Particulate emissions from flares with entrained droplets

by

Mohsen Kazemimanesh

A thesis submitted in partial fulfillment of the requirements for the degree of

Doctor of Philosophy

Department of Mechanical Engineering
University of Alberta

Abstract

In this work, particles emissions from flares with entrained droplets were characterized during the operations of oil/gas wells. It is a likely scenario that droplets of flowback fluids or produced water entrain in the flare gas and burn in an open flame. Major ions found in these fluids are sodium and chloride ions, which can affect the particle emissions from a flare. A benchtop-scale laminar methane diffusion flame with and without NaCl particles, coupled with a high dilution sampling system, was used to study the fundamental interactions between soot and NaCl particles. Soot formation and evolution from inception and surface growth to coagulation and oxidation were observed for soot particles inside the flame. NaCl reduced the coagulation between soot particles in the agglomeration region; however, it also inhibited soot oxidation, leading to higher soot concentration released to ambient air. Freshly nucleated NaCl particles from its vapour phase formed in the post-flame region which were occasionally internally mixed with soot. NaCl also increased light absorption of soot due to its increased concentration; however, this study was inconclusive about whether or not the mass-specific absorption coefficient of soot changed with the addition of NaCl to the flame.

A lab-scale turbulent diffusion flame from a pipe flare with different diameters with various gas compositions representative of flare gases in the upstream oil and gas industry was used with and without entrained droplets of different liquids, including flowback fluids from Cardium and Duvernay formations. Soot particle size and concentration did not depend on flare diameter or exit velocity, but noticeably changed with gas composition and its higher heating value. Data from electron microscopy images and effective density data provided consistent information on soot morphology. Flare soot had an effective density (and hence, a morphology) similar to that of soot from various combustion engines. Moreover, soot morphology was independent of gas

composition, flare diameter, and flare exit velocity over the range tested. Adding water to the flame suppressed soot particle size and concentration. Addition of a tiny amount of inorganic salts to the flame increased particle concentration by orders of magnitude and decreased the particle size significantly, which was due to re-nucleation of salt particles in the post-combustion region. The addition of salts also increased the concentration of soot particles due to inhibition of soot oxidation near the flame front. Adding more salts increased the particle size markedly and the particle concentration slightly. Most of the particles smaller than ~150 nm had an effective density similar to that of salt and most of the particles larger than ~300 nm had a density close to that of soot. This result was also confirmed by electron microscopy images of the particles. These images also showed that most of the particles were either individual salt particles or internally mixed soot and salt particles. The significance of this study lies in its climate implications: increased soot and salt concentrations directly affect global climate by higher absorption and scattering of sunlight, respectively. On the other hand, they indirectly affect the climate by increasing cloud formation as cloud condensation nuclei. These implications may be currently underestimated for particle emissions from flares.

Preface

Some of the research conducted for this thesis was part of a research collaboration, with Dr. Jason Olfert being the lead collaborator at the University of Alberta. The experimental setup for the benchtop laminar flame described in Chapters 2, 3, and 4 was designed by myself. I also ran the experiments and analyzed the data presented in these chapters myself, except Chapter 3 for which Alireza Moallemi helped me in running the experiments and analyzing the data. The experimental setup referred to in Chapter 5 and 6 was designed and operated by Dr. Matthew Johnson's research group at Carleton University. However, the collection of particle size distribution and effective density data and their analysis was my original work, which is presented in Chapters 5 and 6. Details of the role of each collaborator for the experiments in Chapter 5 is outlined below. In Chapter 6, Raman spectroscopy and TEM imaging were done by Alberto Baldelli and Una Trivanovic, respectively, both from the University of British Columbia and part of our research collaboration.

Chapters 2 and 3 of this thesis have been published as

- Kazemimanesh, M., Moallemi, A., Olfert, J.S., and Kostiuk, L.W. (2017). Probe sampling to map and characterize nanoparticles along the axis of a laminar methane jet diffusion flame. *Proceedings of the Combustion Institute*, 36(1):881–888.

- Moallemi, A., Kazemimanesh, M., Kostiuk, L.W., and Olfert, J.S. (2018). The effect of sodium chloride on the nanoparticles observed in a laminar methane diffusion flame. *Combustion and Flame*, 188:273–283.

In the first journal article, I was responsible for the design and conduction of experiments, data collection and analysis as well as writing the manuscript. A. Moallemi assisted with the data

collection. J.S. Olfert and L.W. Kostiuk were the supervisory authors and were involved with concept formation and manuscript editing.

In the second journal article, I was responsible for the design and conduction of experiments, data collection and analysis as well as heavily editing the draft of the manuscript. A. Moallemi assisted with the conduction of experiments, data collection and analysis, and writing the main draft of the manuscript. L.W. Kostiuk and J.S. Olfert were the supervisory authors and were involved with concept formation and manuscript editing.

Chapter 5 of this thesis has been published as

- Kazemimanesh, M., Dastanpour, R., Baldelli, A., Moallemi, A., Thomson, K.A., Jefferson, M.A., Johnson, M.R., Rogak, S.N., and Olfert, J.S. (2019). Size, effective density, morphology, and nano-structure of soot particles generated from buoyant turbulent diffusion flames. *Journal of Aerosol Science*, 132:22–31.

In this journal article, I was responsible for conducting experiments, collecting and analyzing data for particle size distribution and effective density, and writing the manuscript. R. Dastanpour was responsible for collecting and analyzing TEM samples. A. Baldelli was responsible for analyzing Raman spectroscopy and writing the corresponding section in the manuscript, A. Moallemi helped with running the SMPS, M.A. Jefferson operated the flare facility, and K.A. Thomson, M.R. Johnson, S.N. Rogak, and J.S. Olfert were the principle investigators in our research collaboration and were involved with concept formation and manuscript editing.

Acknowledgements

I would like to acknowledge my supervisor, Dr. Jason Olfert, for his support and scientific leadership during the course of this research. He has been a truly supportive supervisor who helped me greatly with his broad knowledge in aerosol science to improve this study. I could not ask for a better supervisor during my years at the University of Alberta.

I also thank my co-supervisor, Dr. Larry Kostiuk, for his great ideas, support, and enthusiasm for this research. I always learned something new from his extensive knowledge in the field of combustion. I also appreciate him for granting his lab space to run part of my experiments.

I would also like to appreciate Dr. Matthew Johnson of Carleton University and his research group to help us run part of my experiments at their Lab-scale Flare Facility. Dr. Steven Rogak is acknowledged for providing a thermophoretic sampler for part of my experiments and for his insightful comments about our work along the course of this research.

Finally, I would like to thank the FlareNet Strategic Network which provided an opportunity for me to attend different conferences and workshops during my PhD studies. The funding agencies which generously supported my research through numerous scholarships, particularly NSERC, are also greatly appreciated.

Table of Contents

List of Tables

List of Figures

Nomenclature

List of Symbols

B_{abs}	Absorption coefficient (m^{-1} or Mm^{-1})
B_{ext}	Extinction coefficient (m^{-1} or Mm^{-1})
B_{scat}	Scattering coefficient (m^{-1} or Mm^{-1})
C_c	Cunningham slip correction factor
d	Particle diameter
d_a	Projected area equivalent diameter (nm)
d_m	Particle mobility diameter (nm)
d_p	Primary particle diameter (nm)
d_{va}	Sauter mean diameter of primary particles (nm)
D_m	Mass-mobility exponent
D_{TEM}	Exponent of power-law fit to TEM data
D_α	Constant exponent
$dN/d\log d_m$	Normalized particle concentration (cm^{-3})
DR	Dilution ratio
e	Electric charge of an electron (1.60×10^{-19} C)
E	Intensity of electric field
I	Intensity of light
k	Constant pre-factor of mass-mobility relationship
k_a	Constant pre-factor

$\bar{K}$	Coagulation coefficient (cm^3/s)
L	Path length of light (m)
m	Particle mass
M	Particle mass concentration (g/m^3 or $\mu g/m^3$)
$m(d_m)$	Mass-mobility relationship function
N	Particle number concentration (cm^{-3})
n	Number of moles (mol)
$n(d_m)$	Mobility diameter distribution of particles
$\dot{n}$	Molar rate (mol/s)
P	Pressure (Pa)
q	Electric charge
R	Ideal gas constant (8.314 J/mol·K)
T	Temperature (K)
V	Volume of fluid
V_T	Terminal velocity of particle in motion
x	Size parameter
X	Mole fraction
Z	Electrical mobility
λ	Wavelength
μ	Dynamic viscosity
Φ	Equivalence ratio

ρ_{eff}	Effective density (kg/m^3)
ρ	Material density (kg/m^3)
σ_g	Geometric standard deviation
ω	Single-scattering albedo

List of Acronyms

AAE	Absorption Ångström Exponent
AER	Alberta Energy Regulator
API	American Petroleum Institute
BC	Black Carbon
CCN	Cloud Condensation Nuclei
CI	Confidence Interval
CMD	Count Median Diameter
CPC	Condensation Particle Counter
CPMA	Centrifugal Particle Mass Analyzer
DMA	Differential Mobility Analyzer
EC	Elemental Carbon
ESP	Electrostatic Precipitator
GDI	Gasoline Direct Injection
GSD	Geometric Standard Deviation

HAB	Height Above Burner
HHV	Higher Heating Value
HPDI	High Pressure Direct Injection
HRTEM	High Resolution Transmission Electron Microscopy
LIF	Laser-Induced Fluorescence
LII	Laser-Induced Incandescence
LOSA	Light Of Sight Attenuation
MAC	Mass-specific Absorption Coefficient
MSC	Mass-specific Scattering Coefficient
OC	Organic Carbon
PAH	Polycyclic Aromatic Hydrocarbon
PASS-3	Three-wavelength Photoacoustic Spectrometer
PAX	Photoacoustic Extinctiometer
PFI	Port Fuel Injection
PM	Particulate Matter
PSD	Particle Size Distribution
RF	Radiative forcing
SLPM	Standard Litre Per Minute
SMPS	Scanning Mobility Particle Sizer
SSA	Single-Scattering Albedo
TEM	Transmission Electron Microscopy

TOA	Thermal-Optical Analysis
TDS	Total Dissolved Solids
TPS	Thermophoretic Sampler
UOG	Upstream Oil and Gas
USGS	United States Geological Survey

CHAPTER 1

Introduction, Problem Statement, and Thesis Objectives

In this chapter an overview of flaring in the oil and gas industry and its implications, hydraulic fracturing and flowback operations, soot and its composition and properties, thesis motivation and problem statement, and finally the objectives of the thesis are presented.

1.1 Flaring

The upstream oil and gas industry (UOG) deals with exploration and extraction of gas and petroleum, while refining and processing of gas and petroleum is done in the downstream oil and gas industry. In both the upstream and downstream oil and gas industries, two practices are used extensively to dispose of unwanted and economically unviable gases: venting and flaring (Johnson *et al.* 2001). In venting the unwanted gases are simply released into the atmosphere, while in flaring, the undesired combustible gases are burned off in an open atmospheric flame (Johnson *et al.* 2001; Tyner and Johnson 2014). Gases are typically flared or vented because their processing is not economic (*e.g.*, when the well is far from a pipeline or when it contains low concentrations of toxic hydrogen sulfide) or due to emergency blow-downs at processing facilities (Johnson *et al.*

2001). The composition of flared or vented gases varies significantly from site to site but, in general, methane is the main component of these gases (Johnson *et al.* 2001; McEwen and Johnson 2012). Flaring is often preferred over venting because the global warming potential of methane over a 100-year time horizon is 28 times higher than carbon dioxide produced from burning methane (Myhre *et al.* 2013). However, flaring has the potential to produce soot and other pollutants which negatively impact the environment and air quality (see Section 1.1.3).

The significance of these negative impacts becomes clearer by considering the sheer volume of flaring. Recent estimates based on satellite data indicate that total flaring volume is 143±13.6 billion m^3 globally each year (Elvidge *et al.* 2015), an amount equivalent to ~3.9% of global natural gas production (British Petroluem 2018). In Canada, the province of Alberta is the most significant source of flaring (McEwen and Johnson 2012), with its total flaring volume peaking at 1,041 million m^3 in 2014 (Alberta Energy Regulator 2018) associated with the rapid development of unconventional oil and gas resources and the added upgrading due to converting oil sands bitumen to fuels. Latest flaring volumes in Alberta were approximately 740 million m^3 in 2017 (Alberta Energy Regulator 2018). In the United States, the annual flaring and venting volume steadily increased from 2000 to a maximum of 8,320 million m^3 in 2014 and with current levels of 6,670 million m^3 in 2017 (U.S. Energy Information Administration 2018). The sharp increase in flaring and venting volume in the U.S. has been associated with the development of unconventional oil and gas resources most notably in Bakken Shale in North Dakota, the Eagle Ford and Haynesville Shales in Texas, and the Marcellus Shale in Pennsylvania, New York, and Ohio (see Figure 1.1). Similarly, the slight decrease in flaring and venting volume since 2014 has been associated with the decrease in production.

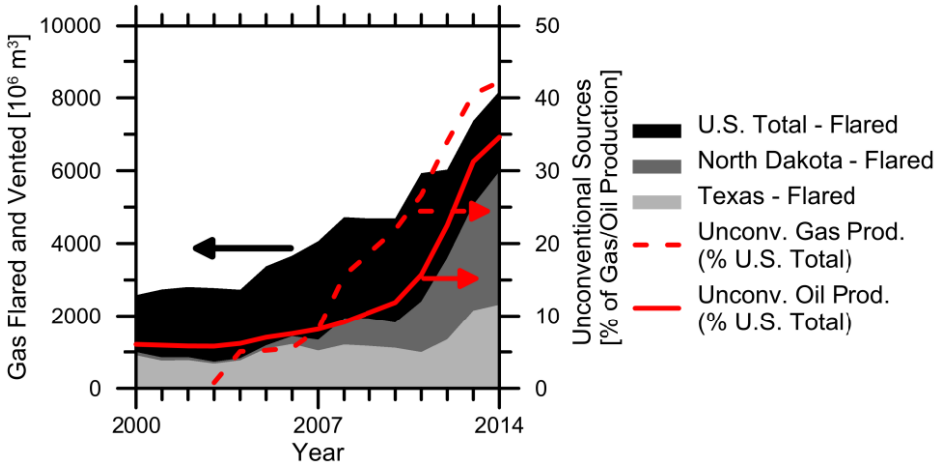

Figure 1.1: Volume of gas flared and vented in the U.S. from 2000 to 2014. Also shown is the percentage of oil and gas production in the U.S. from unconventional sources. Source of the plot: Jefferson (2017).

1.1.1 Flare Categories

Flares are typically categorized into three groups: production flares, process flares, and emergency flares (Johnson *et al.* 2001). Production flares refer to all kinds of flaring which happen during upstream production of oil and gas resources. Production flaring is further divided into two sub-categories: well testing and solution gas flaring. Well testing happens at the initial development of a gas well when the gas may be flared at very high flow rates for a few days, typically without engineered provisions for smoke reduction. By contrast, solution gas flaring is usually established during the initial operation of an oil well. At this time, the solution gases may be flared while assessing their economic suitability as sale-grade natural gas. If the flared gases are not economic to sell, then the solution gas can be flared for the life of the oil well. Typically, solution gas flares have significantly lower flow rates and exit velocities compared to flares associated with well testing. However, due to their abundance and continuous operation, solution gas flares are the primary source of global flaring and venting (Johnson *et al.* 2001; Johnson and Coderre 2012).

Process flaring typically happens at refineries, petrochemical plants, and gas plants for gases that leak past the relief valves. Process flaring is usually continuous and has relatively low flow rate;

however, during blow-down of process units or start-up and shutdown of the plant, significantly higher gas flow rates may be flared (Johnson *et al.* 2001).

Emergency flares typically operate at large refineries or gas plants during emergency situations, such as fire, valve rupture, compressor failure, and over-pressure. In these situations, large volumes of flammable gas need to be disposed of very quickly at very high flow rates and exit velocities approaching sonic velocity (Johnson *et al.* 2001).

1.1.2 Solution Gas Flares

As mentioned in the previous section, the majority of global flaring occurs during upstream production of oil and gas resources and, thus, solution gas flaring is the most significant contributor to global flaring volumes which is discussed in more detail here. Solution gas is the dissolved gas and volatile chemical species in oil and brackish formation liquids, which is released from the liquids when it is brought to the surface and its pressure is reduced from the high pressure of a subsurface geological formation to near atmospheric pressure (Johnson *et al.* 2001; Johnson and Coderre 2012). When the oil is brought to the surface, dissolved solution gas is separated from the oil at a separation facility known as an "oil battery". In an oil battery site, oil is stored temporarily for further processing, while solution gas is flared, vented, or conserved (as fuel source for the battery site or for sale).

Solution gas flare stacks are typically 10 m high pipes with an internal diameter of ~100 mm (Johnson *et al.* 2001). In contrast, commercial flares (such as flares used in refineries and other industries) have a more complex design. Commercial flare stacks typically include a commercial burner tip, pilot, and smoke suppressant. Commercial burner tips are complicated in design and may include integration of a pilot flame, steam or air injection (to supress soot), and protection

from crosswind. The pilot is used to keep the flare lit during start-up, when low heating value gas is flared, or during high crosswinds. Smoke suppression is typically achieved by injecting steam or air into the flame. It should be noted that smaller or remotely-located solution gas flares rarely or never use these options (McEwen 2010), which are the type of flares of interest in this thesis.

1.1.3 Environmental and Health Implications of Flaring

Environmental implications of flaring are typically related to combustion efficiency and emissions. In a typical solution gas flare, the combustion efficiency (or carbon conversion efficiency) is a measure of the ability of the flare in fully converting all carbon in the hydrocarbons into CO_2 (Johnson *et al.* 2001). When there is combustion inefficiency in flaring, unburned hydrocarbons, carbon monoxide, soot, (semi-)volatile organic compounds, etc. are produced. Unburned hydrocarbon in the form of CH_4 has negative impacts on the climate because global warming potentials of methane is 28 times higher than carbon dioxide over 100 years (Myhre *et al.* 2013).

Besides gas-phase emissions from flares, particle emissions such as soot are also a major concern for human health and the environment. From a health perspective, soot particles are identified to have adverse effects on human health and affect human life expectancy significantly (Janssen *et al.* 2011; Grahame *et al.* 2014). The global burden of disease assessment in the period of 1990–2010 for 21 regions of the world attributed an annual ~3.2 million premature mortalities to ambient $PM_{2.5}$ exposure, which makes $PM_{2.5}$ as one of the leading risk factors for premature death (Lim *et al.* 2012). On a local scale, elevated concentrations of pollutant emissions, directly affecting the local air quality, have been reported for ground-level measurements downwind of flaring sites (Sonibare *et al.* 2010; Abdul-Wahab *et al.* 2012; Bunch *et al.* 2014; Paulik *et al.* 2015; Swarthout *et al.* 2015).

From an environmental perspective, current estimates suggest that black carbon (BC, a major component of soot) is the second strongest contributor to global warming with an average radiative forcing of 0.9 W/m^2, next to CO_2 with a radiative forcing of 1.66 W/m^2 (Ramanathan and Carmichael 2008; Bond *et al.* 2013). On a regional level, one study has directly implicated high-latitude flaring as a critical source (~42%) of BC emissions observed in the lower troposphere of the Arctic (latitudes greater than 66° N), which contribute to the Arctic haze phenomenon and deposit on the snow (Stohl *et al.* 2013). Deposition of BC particles on snow and ice significantly reduces the surface albedo[1] of the latter and promotes the melting of snow and ice due to enhanced light absorption by BC particles (Menon *et al.* 2002; Hadley and Kirchstetter 2012). The melting of Arctic snow and ice contribute to a positive feedback loop, where melting of snow and ice reveals the darker surfaces underneath them, resulting in more absorbed sunlight radiation and warmer temperatures, further reducing the amount of snow and ice (Etkin 1990). Consequently, the melting of Arctic snow and ice can lead to the raise in global sea levels. Some studies suggest that due to the relatively short lifespan of soot in the atmosphere (only a few weeks), reduction in soot emissions is the fastest means to decrease the trend of global warming in the short term (Ramanathan and Carmichael 2008).

1.2 Hydraulic fracturing

Induced hydraulic fracturing (in short, hydrofracturing or 'fracking') is a ubiquitous technique used in the UOG industry to increase the extraction rate from unconventional oil and natural gas reservoirs, commonly trapped in low-permeability rock formations such as shale gas and shale oil. Wellbores for hydraulic fracturing can be vertical, angled, or horizontal (*i.e.*, combination of a vertical section and a horizontal section to cover more of the oil or gas reservoir). The depth of the

[1] Albedo is the fraction of the total light intensity received that is reflected (or scattered) from the surface.

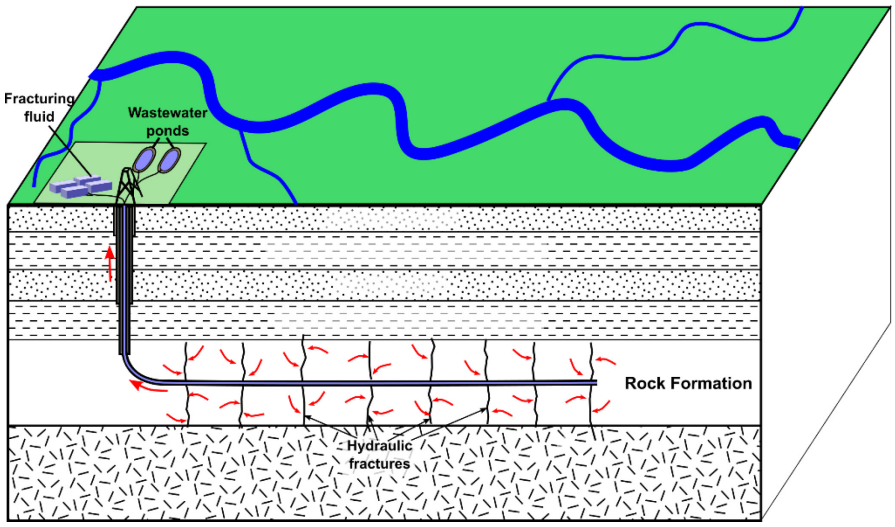

Figure 1.2: Schematic of a typical hydraulic fracturing process for unconventional production of hydrocarbon resources. Image from https://commons.wikimedia.org/wiki/File:HydroFrac2.svg under Creative Commons License.

vertical section can be 0.2–~3 km into the rock formation and the length of the horizontal section can be 0.5–4 km (Tyner and Johnson 2014). Figure 1.2 shows the schematic of a typical hydraulic fracturing process for a horizontal wellbore. During hydraulic fracturing, large volumes of a mixture of water, proppant (usually sand, ceramic pellets, or aluminum oxide), and other chemical additives, collectively known as fracturing fluid, are injected into the wellbore at high pressure (35–70 bar). The upper vertical section of the wellbore is generally lined with casing, which consists of several layers of steel pipe and cement. The horizontal section of the wellbore is lined with perforated casing. The injection of fracturing fluid into the wellbore at high pressure causes small fractures, typically less than 1 mm wide, in the rock formation along the horizontal section of the wellbore and a mixture of oil, gas, and brine trapped in the formation can flow to the wellbore. The newly created fractures can extend several hundred meters to a few kilometers away from the wellbore, thus increasing the extraction of oil and gas from isolated reservoirs significantly. The proppant holds the fractures open in the formation and oil and gas can continue to flow to the wellbore even after hydraulic fracturing is finished. When the pressure of the

fracturing fluid is removed, the internal pressure of the rock formation causes the fracturing fluid now mixed with formation water to return to the surface through the wellbore. This stage of well-completion is called a *flowback operation* and the fluid is known as *flowback fluid*. Flowback fluids returning to the surface are typically high in dissolved solids and salts, primarily due to mixing with formation water. It should be noted that the fluids returned to the surface prior to production are simply known as flowback fluids, while any fluids produced concurrent with the production of oil and gas are known as *produced water* (Barbot *et al.* 2013).

1.2.1 Composition of Fracturing Fluid

Fracturing fluid composition is primarily determined based on water characteristics and geological properties of the target rock formation. The majority of current fracturing fluids are water-based, which mostly include *slick water*, *i.e.*, water mixed with proppant and small quantities of chemical additives (Gandossi 2013; Gallegos and Varela 2015). The composition of fracturing fluid used in the UOG industry varies widely from site to site. In recent years, public and governmental concerns about cross-contamination of underground water resources as a result of hydraulic fracturing has led to regulatory requirements for the UOG industry in Canada and the U.S. to disclose the composition of fracturing fluid and the amount of chemical additives (Frac Focus 2019).

Slick water fracturing fluid is composed of mainly water and proppant (collectively 99% by mass) as well as a small fraction of chemical additives. Analysis of Frac Focus database and some other reports show that slick water contains based on mass ~90% water, ~9% proppant, and ~1% chemical additives (URS Corporation 2011; Frac Focus 2019).

The small quantities of chemical additives used in the fracturing fluid varies significantly for each site and operator; however, typically between 3–12 chemical additives are used (Gomaa *et al.*

Table 1.1: Commonly used additives in water-based fracturing fluids, chemical examples for each additive, and their purpose

Additive	Purpose of usage	Example of chemicals
Acids	Remove mineral build-up in wellbore. Precursor to fracturing fluid injection to create cracks in the rock formation.	Hydrochloric Acid (3–28% concentration by mass)
Biocides	Inhibit bacteria growth when organic fracturing fluids are used.	2,2-Dibromo-3-nitrilopropionamide
Breakers	Break polymer chains for fluid recovery	Peroxydisulfates
Corrosion Inhibitors	Prevent corrosion in wellbore pipe	Glutaraldehyde; Acetone; Isopropanol
Friction Reducers	Reduce wellbore friction	Polyacrylamide
Scale Inhibitor	Remove scale build up in pumps and wellbore pipe	Ethylene glycol
Surfactants	Reduces the surface tension of fracturing fluid	Ethanol; Isopropyl alcohol

2011; URS Corporation 2011). Table 1.1 lists the most commonly used groups of additives in the fracturing fluids with example chemicals and the purpose of each additive. The Frac Focus database and other reports (URS Corporation 2011) reveal that numerous chemicals are used in fracturing fluids other than the examples listed in Table 1.1; however, reviewing the list of these chemicals is beyond the scope of the current study. Although chemical additives are a small fraction of the fracturing fluid, the sheer volume of fracturing fluids used per operation (9,000–80,000 m^3) and the abundance of fracturing operations make the amount of chemicals used in hydraulic fracturing operations significant.

1.3 Flowback Fluid

The fracturing fluids injected into the wellbore mix with oil, solution gas, and water in the rock formation when it is brought back to the surface. Therefore, flowback fluids are ultimately the fluids of interest because these are the fluids that should be treated, reused, or disposed of (Vengosh *et al.* 2014). Thus, we discuss the composition of flowback fluids in more detail. Recent studies have shown that the composition of flowback fluids are different than that of fracturing fluids

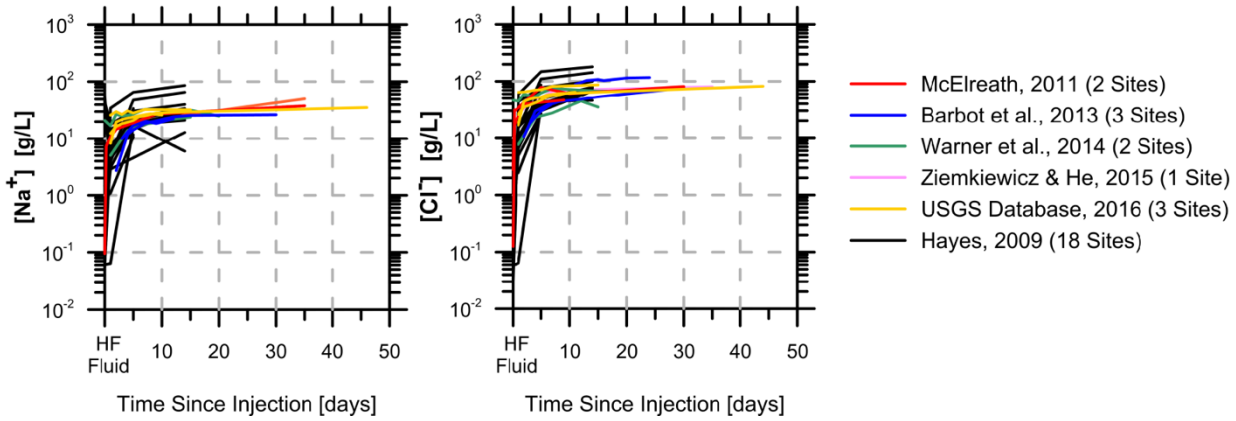

Figure 1.3: Temporal concentration of sodium and chloride ions in flowback fluid over a span of up to two month. Plots are from Jefferson (2017).

(Hayes and Severin 2012; Ziemkiewicz and He 2015). Moreover, the composition of flowback fluids evolves with time as the flowback operation progresses over days to months. Figure 1.3 shows the temporal change in the concentration of sodium cation (Na^+) and chloride (Cl^-), as two major ions in the flowback fluids, with respect to days after hydraulic fracturing operation, based on chemical composition data reported for different sites (Mcelreath 2011; Hayes and Severin 2012; Barbot *et al.* 2013; Warner *et al.* 2014; Ziemkiewicz and He 2015). It is clear that the concentration of Na^+ and Cl^- increases sharply by several orders of magnitude over the first few days subsequent to fracturing operation until it reaches an equilibrium concentration. The same temporal trend is also seen for the concentration of total dissolved solids (TDS) in flowback fluids. The flowback fluids are similar in composition to fracturing fluids shortly after the beginning of flowback operation, while the composition of the former converges to that of produced water after many days subsequent to the start of flowback operation. The transition in the composition of flowback fluids from fracturing fluids to produced water is presumably due to mixing with the rock formation water.

Chemical composition of flowback fluids has been studied for some formations such as Marcellus shale (Gregory *et al.* 2011; Horner *et al.* 2011; Chapman *et al.* 2012; Hayes and Severin 2012;

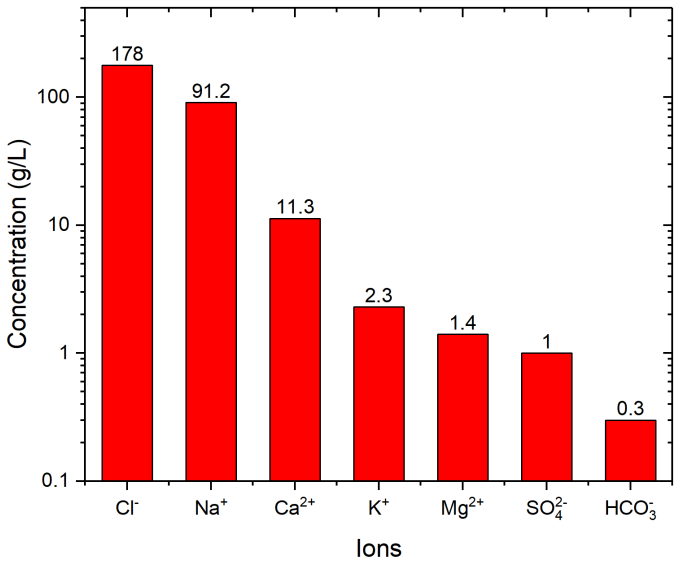

Figure 1.4: Concentration of major cations and anions found in produced water in descending order based on the analysis of Moallemi (2017). Sodium and chloride are the two major ions, which are order(s) of magnitude higher in concentration than the other ions.

Barbot *et al.* 2013; Haluszczak *et al.* 2013; Ziemkiewicz and He 2015), Barnett shale (Horner *et al.* 2011), Woodford formation (Acharya *et al.* 2011), and Horn River shale (Paktinat *et al.* 2011). Moreover, the United States Geological Survey (USGS) maintains an extensive database about the chemical composition of flowback fluids and produced water sampled from different regions of the United States (Blondes *et al.* 2018). It is a plausible assumption that the equilibrium concentration of salts in flowback fluids after few weeks approaches that of produced water (*i.e.*, the fluid brought to surface during production). Previous studies have analyzed the USGS database and have determined the median concentration of different cations and anions found in flowback fluids (Moallemi 2017), which is shown in Figure 1.4. It is clear from this chart that sodium and chloride are the major ions in flowback fluids and other ions are order(s) of magnitude lower in concentration compared to these two ions. Other studies have also reported that sodium and chloride ions are the predominant ions found in flowback fluids (Mcelreath 2011; Barbot *et al.* 2013; Miller *et al.* 2013). It also seems that the naturally-occurring concentrations of sodium and

chloride from formation water rapidly (*i.e.*, within days) are larger than the concentrations of chemicals used in the fracturing fluids.

1.4 Soot and its Structure and Composition

As mentioned in Section 1.1.3, soot is considered as an important risk for human health and is the second strongest contributor to climate forcing, after carbon dioxide. In this section, we discuss the formation of soot and some of its properties relevant to this thesis, such as morphology, nano-structure, composition, optical properties, and mixing state.

Under ideal conditions, *i.e.* stoichiometric condition, the combustion of hydrocarbons leads to the production of carbon dioxide and water. However, in practical combustion devices, such as gas turbines or internal combustion engines, conditions can deviate locally from stoichiometric (ideal) conditions due to the presence of insufficient oxygen, which causes the combustion to be incomplete and produce carbon monoxide, soot, unburned hydrocarbons, *etc*. in addition to carbon dioxide and water. The formation and evolution of soot is a complex chemical and physical process, which takes place in different stages. Over the past decades, numerous studies have used different types of flames and fuels to understand the chemical and physical processes related to how soot is formed and its evolution in the flames (Haynes and Wagner 1981; Frenklach and Wang 1991, 1994; Kennedy 1997; Appel *et al.* 2000; Frenklach 2002).

Figure 1.5 shows a schematic representation of soot formation and evolution in a flame. Starting from the burner outlet and moving up, the fuel undergoes decomposition to form small radicals such as OH, O, H, CH, and CH_2. These small radicals lead the reaction to form larger hydrocarbon radicals. Acetylene is one such intermediate species, which is believed to play a significant role in the formation of the first aromatic ring (Frenklach 2002; Wang 2011). As the reaction between

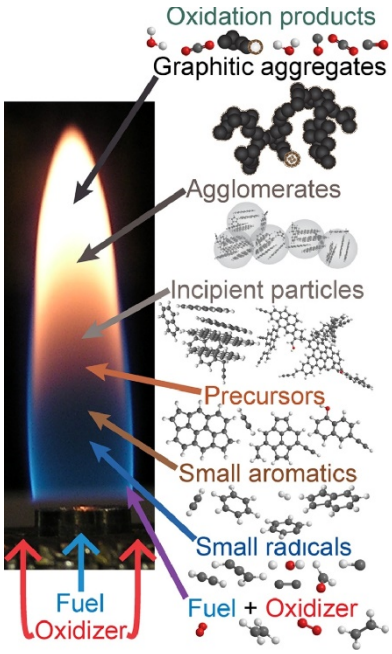

Figure 1.5: Schematic representation of soot formation and evolution in a flame. Image re-used from Michelsen (2017) with permission.

aromatics and acetylene continues, new aromatic rings are added to the initial aromatic molecule, which forms larger polycyclic aromatic hydrocarbons (PAH). The PAH species are believed to be the precursor of soot formation (Richter and Howard 2000; Frenklach 2002; McEnally *et al.* 2006; Wang 2011). These PAH precursors react, combine, and grow to form *incipient soot particles*. Incipient soot particles have carbon to hydrogen ratios (C/H) in the range of 1.4–2.5 (D'Alessio *et al.* 1992; Ciajolo *et al.* 1998; Russo *et al.* 2015). Transmission electron microscopy and atomic force microscopy confirm that incipient soot particles have spherical structures (Michelsen 2017). These incipient particles grow further by surface growth to become *primary particles* with diameters in the range of 10–50 nm, which have a graphitic layer structure (Dobbins and Megaridis 1987; Puri *et al.* 1993; Wang 2011; Vander Wal *et al.* 2014). Moving up in the flame, the primary particles coagulate with each other due to Brownian motion and form soot aggregates (sometimes used interchangeably with soot agglomerates). The soot aggregates have strong bonds between their primary particles so that they cannot be readily taken apart (Pratsinis 1998; Eggersdorfer and

Pratsinis 2014). Finally, if the soot aggregates undergo substantial oxidation, their primary particle size decreases and the aggregate structure may collapse. Otherwise, the soot aggregate can escape the flame and be released to the ambient air.

Figure 1.6 shows an image of a freshly released soot aggregate from a combustion source taken by transmission electron microscopy (TEM). The image shows that soot aggregates are typically smaller than 1 µm, have branched or fractal-like structures (Sorensen 2011), and consist of many nearly spherical primary particles coagulated and aggregated with each other. The image also highlights two of the soot primary particles. In Figure 1.6, d_p is the diameter of the primary particles and the projected area equivalent diameter, d_a, is the diameter of a spherical particle which has the same projected area as the soot aggregate (shown as larger dashed circles in the image). Projected area equivalent diameter is one way to describe the size of a fractal-like soot aggregate.

Another way to describe the size of a soot aggregate is by its mobility equivalent diameter. The electrical mobility, Z, of a spherical particle is defined as the velocity of the particle with a charge $q = ne$ in an electric field with strength of unity (Hinds 1999, p. 322). In this definition, n is the

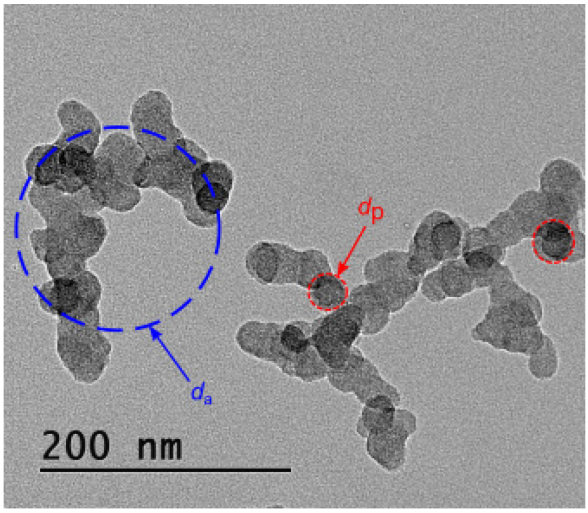

Figure 1.6: Image of fresh soot aggregates from a combustion source using transmission electron microscopy.

number of primary charges and e is the electric charge of an electron. It follows from this definition that

$$Z = \frac{V_T}{E} = \frac{neC_c}{3\pi\mu d} \tag{1.1}$$

where V_T is the terminal velocity of the particle in motion in the electric field, E is the intensity of the electric field, C_c is the Cunningham slip correction factor (significant for particles smaller than 1 μm), d is the particle diameter, and μ is the viscosity of the air (Hinds 1999). Now the mobility equivalent diameter, hereinafter called mobility diameter, of a soot aggregate is defined as the diameter of a spherical particle which has the same electrical mobility as the soot aggregate. The aerosol research community use instruments, such as differential mobility analyzer (DMA), to classify aerosol particles (such as soot aggregates) by their mobility diameter. This is achieved by the balance between electrical forces on a charged particle in an electric field and the drag force experienced by the particle in motion in that field.

As mentioned earlier, the ratio of carbon to hydrogen of a soot primary particle is typically large, suggesting that it is mostly constituted from carbon, which is referred to as elemental carbon (EC). On the other hand, soot can also contain hydrogen, oxygen, and other small ($C < 10$) or large ($C > 24$) PAH molecules, which are often referred to as organic carbon (OC) (Russo *et al.* 2017). One commonly used method to determine the EC and OC content of soot particles is thermal-optical analysis (TOA). In this method, the soot sample is collected on quartz fiber filters and the speciation of organic and elemental carbon is accomplished through the change in temperature under controlled atmosphere in a sample oven. A small punch of the filter is put in the sample oven with a helium (He) atmosphere, where the sample is heated in four increasing temperature steps up to 820 °C to remove all organic carbon on the filter. During this stage, some organic compounds

(as much as 30%) may convert by pyrolysis to elemental carbon. This conversion is continuously monitored by measuring the transmission of a laser through the filter. As the organic compounds are vaporized, they are immediately oxidized to CO_2 in an oxidizer oven which follows the sample oven. The flow of helium, containing the CO_2, then goes to a methanator oven where the CO_2 is reduced to methane and its quantity is measured (Birch and Cary 1996). After the sample oven is cooled to 525 °C, the helium atmosphere is switched to a 2% O_2 in He mixture in the sample oven. Then the sample oven temperature is stepped up to 850 °C. During this phase, both the original elemental carbon and that was produced by the pyrolysis of organics during the first phase are oxidized to carbon dioxide. The carbon dioxide, as in the first stage, is converted to methane and its quantity is measured. The point at which the transmittance of the laser starts to increase (due to removal of elemental carbon from the filter), is known as the *split point* and the amount of carbon before and after this point is considered as organic and elemental carbon, respectively (Birch and Cary 1996).

Another method that is used to characterize carbonaceous materials, such as soot particles, is Raman spectroscopy (Dennison *et al.* 1996; Lyon *et al.* 1998; Escribano *et al.* 2001; Ferrari and Robertson 2001; Dresselhaus *et al.* 2010). In Raman spectroscopy, a laser beam excites the sample by inducing oscillating electric dipole moments. Some of the excited molecules end up in a vibrational state different from the original state, thereby scattering the laser light inelastically, *i.e.*, at frequencies different from the excitation frequency (Saffaripour *et al.* 2017). The shift in the frequency of the scattered light relative to the excitation frequency, referred to as the Raman shift, results from the difference between the original and final energy states of the bonds. The Raman shift corresponds to a very specific bond within the sample. For example, a Raman shift frequency of 1584 cm^{-1} represents highly-uniform carbon atoms in planar graphitic sheets. Soot has a

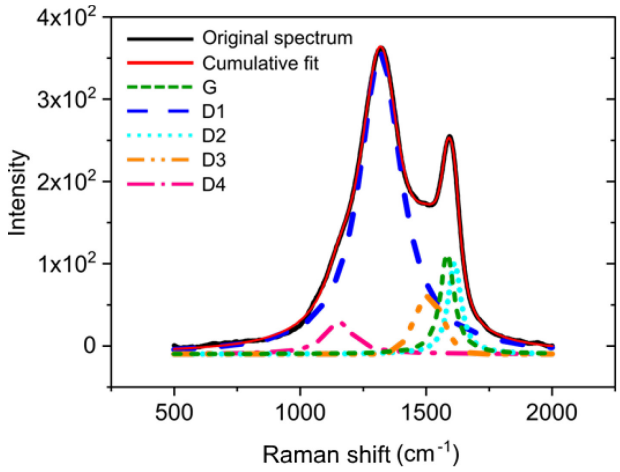

Figure 1.7: Typical Raman spectrum of soot showing two broad and strongly-overlapping peaks. The measured Raman spectrum is best fit by five different bands (one G band and four D bands).

complex multi-component structure, composed of an amorphous structure in its inner core surrounded by a crystalline graphitic shell on its outer surface (Vander Wal *et al.* 2007; Raj *et al.* 2010; Wang 2011). Figure 1.7 shows a typical Raman spectrum of soot which is composed of two broad and overlapping bands. The rightmost band, centered at ~1591 cm^{-1}, is due to crystalline graphitic structure and is known as the graphite band (G band) and the leftmost band, centered at ~1344 cm^{-1}, is due to defects in the graphitic structure and is known as the defect band (D band). Raman spectra of carbonaceous material are best represented with a fit of five different bands (Cuesta *et al.* 1994; Sadezky *et al.* 2005), including one G band and four D bands due to different types of defects in the graphitic structure. These four defect bands and their fitting method will be discussed in more details in Chapter 5. The ratio of the intensities of D and G bands can represent the relative defects in the graphite crystals.

When fresh soot aggregates are released from the combustion source into the atmosphere, it is extremely hydrophobic. During their lifetime in the atmosphere, which is from a few days to about two weeks (Cape *et al.* 2012), soot particles undergo an aging process and due to the oxidation by atmospheric OH, O_3, SO_2, and NO_x, polar surface groups form on the soot that can cause the soot

to become hydrophilic (Zuberi *et al.* 2005). Sulfates and other organic materials can then condense on these hydrophilic soot particles as a coating. In this case, it is often said that the soot particle is internally mixed with organic materials. If the organic material exist as individual aerosol particles separate from soot aggregates, then this mixing state is referred to as externally mixed soot and organic material. Figure 1.8 shows soot and organic material that are either internally or externally mixed. The coating on soot particles can change the absorption and scattering of light by these particles or it can affect the morphology of the fractal-like soot aggregates and cause them to restructure to a more compact shape (Xue *et al.* 2009; Ghazi and Olfert 2013). The coating of soot particles in the atmosphere can have complex effects on the optical properties of soot, such as light absorption and scattering. On the one hand, the coating can act as a magnifier (the so-called *lensing effect*) and enhance the absorption of light by soot particle. On the other hand, the coating can decrease the projected area of soot aggregate due to restructuring and, thus, decreasing its absorption of light. Therefore, the net effect of aging process of soot in the atmosphere is complex and uncertain.

As mentioned earlier, the optical properties of soot can change due to coating. An aerosol particle can redirect an incident light beam in many directions, which is known as scattering of light from that particle. The particle can also absorb some of the energy from incident light depending on its

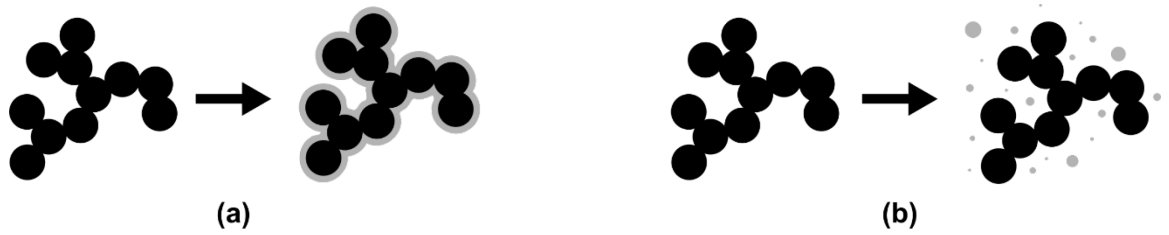

Figure 1.8: Schematic representation of two mixing states: (a) soot aggregate internally mixed with organic material as coating, and (b) soot aggregate externally mixed with organic material. The organic material is shown in grey.

material properties, i.e. refractive index, and turn that into thermal energy. Thus, the extinction in light intensity due to a particle is the sum of light scattering and absorption by that particle. The extinction coefficient, B_{ext}, can be determined based on Beer-Lambert law as follows:

$$B_{ext} = -\frac{1}{L}\ln\frac{I}{I_0} \tag{1.2}$$

where L is the path length of the light through the aerosol particles, I_0 is the intensity of incident light, and I is the light intensity measured after extinction by aerosol particles. It simply follows that $B_{ext} = B_{scat} + B_{abs}$, where B_{scat} and B_{abs} are the scattering and absorption coefficients, respectively. Since absorption and scattering coefficients depend on the concentration of aerosol particles, it is common to normalize them by the aerosol mass concentration and use mass-specific absorption coefficient (MAC; also known as mass absorption cross-section) or mass-specific scattering coefficient (MSC; also known as mass scattering cross-section). MAC and MSC are defined as follows

$$MAC = \frac{B_{abs}}{M} \tag{1.3}$$

$$MSC = \frac{B_{scat}}{M} \tag{1.4}$$

where M is the mass of aerosol particles per unit volume of air, *i.e.* the mass concentration of particles. If absorption and scattering coefficients have a unit of m^{-1} and mass concentration is expressed in g/m^3, then MAC and MSC would have a unit of m^2/g. Another important optical property of aerosol particles is the single-scattering albedo (SSA or ω), which is a measure of the fraction of extinction due to scattering and is defined as

$$SSA = \frac{B_{scat}}{B_{ext}} = \frac{B_{scat}}{B_{scat} + B_{abs}} \tag{1.5}$$

and is a unitless parameter. The single-scattering albedo is an important parameter in evaluating the net climate (radiative) forcing of aerosol particles.

1.5 Thesis Motivation and Problem Statement

After the hydraulic fracturing operation is finished in a wellbore, the flowback fluid along with oil and solution gas is brought to the surface. At the separation facility at an oil battery site, the flowback fluids and solution gas are separated from the oil. The separated oil is typically sent to a pipeline, while the economically nonviable solution gas is directed to the flare stack to combust in an atmospheric flame. A knock-out drum, which is a horizontal drum with interior baffle plates, is typically used to remove flowback liquids from the solution gas.

Due to inefficiencies in the knock-out drums used for separation at oil battery sites, the separation process can create scenarios where droplets of flowback fluids can entrain in the solution gas flow directed to the flare stack for flaring. The occurrence of such scenarios in knock-out drums have been previously reported for the separation of liquid hydrocarbons and solution gas at oil battery sites (Strosher 2000). In addition to inefficiencies in knock-out drums, entrainment of flowback fluid droplets in solution gas flow is possible due to the design criteria used for these drums. American Petroleum Institute (API) Standard 521 requires that droplets with diameter larger than 300 μm must be removed from the gas flow (American Petroleum Institute 2014), which is also the recommended design criteria in Alberta Energy Regulator (AER) Directive 60 and Saskatchewan ECON S-20 guideline. Thus, it is possible that liquid droplets smaller than 300 μm can be carried over and entrain in the solution gas flow and ultimately burn in the open flame. Evidence for the carry over of flowback fluid droplets into a flare has been recently reported for flares in Bakken region in North Dakota (Milani *et al.* 2019). In this study, emission spectroscopy

was used to detect carried-over sodium to the flare based on its emission signatures (at wavelengths of 588.99 nm and 589.59 nm).

The carried-over droplets of flowback fluids to the flare and their combustion in the flame, raise questions and concerns about their effect on the formation and emission of pollutants, including soot. In such scenarios, there is a potential for combustion emissions distinct from the combustion of gaseous hydrocarbons without liquid droplets in the flare stream. Gas-phase and particulate emissions from flares have been investigated in several recent studies for laboratory flares or real flares in the field (Johnson *et al.* 2011, 2013; McEwen and Johnson 2012; Corbin and Johnson 2014; Schwarz *et al.* 2015; Weyant *et al.* 2016; Conrad and Johnson 2017; Gvakharia *et al.* 2017). However, to the author's knowledge, there are no published studies specifically considering the effects of entrained aerosols from simulated or real flowback fluids in gas flow on physical properties and mixing state of the particle emissions from flares. The possibility of aerosolized flowback fluids, high in dissolved sodium chloride, which is a result of poor design regulations or inefficient separation, provides the justification and motivation for this work to study the particle emission properties in such scenarios.

1.6 Thesis Objectives

The main objective of this thesis is to investigate the potential effects of entrained aerosols of simulated and real flowback fluids on the microphysical and morphological properties and the mixing state of particle emissions from laboratory-scale flares and to understand the underlying interactions that lead to these particle emissions. Because sodium cations and chloride anions are the major ions with an order of magnitude higher concentration than other ions in flowback fluids (Section 1.3), sodium chloride was chosen as one of the additives to the flare, although surrogate and real flowback fluids were also tested. Besides measuring and characterizing the final state of

the particle emissions due to flowback liquid entrainment, which was conducted on a laboratory-scale large turbulent diffusion flame under controlled conditions, it is also necessary to understand how this final state was arrived at.

Combustion scientists often use well-defined bench-top laminar flames to study and understand the mechanisms of soot formation and evolution. One such bench-top flame is the laminar diffusion flame called the Santoro burner (Santoro *et al.* 1983), which has been used extensively in previous experimental and modelling studies on soot formation and soot emission properties (Smyth *et al.* 1985; Dobbins and Megaridis 1987; Santoro *et al.* 1987; Samson *et al.* 1987; Puri *et al.* 1993, 1994; Quay *et al.* 1994; Shaddix and Smyth 1996; Smooke *et al.* 2005; Schulz *et al.* 2006; McEnally *et al.* 2006; Bueno *et al.* 2011; Dworkin *et al.* 2011; Slavinskaya *et al.* 2012; Radney *et al.* 2014; Michelsen *et al.* 2015). One advantage of using laminar flames, which makes them ideal for studying soot formation and evolution processes as opposed to complex practical combustors, which often include turbulent flames, is that the laminar flame is highly reproducible without instantaneous changes encountered in turbulent flames. Thus, we used this bench-top laminar diffusion flame (*i.e.*, Santoro burner), with methane as the fuel of choice, to study the evolution of particles when NaCl was introduced into the flame. Using a diffusion flame is relevant to the flame type encountered in flares, which are non-premixed flames. We also used methane in the bench-top flame because it is the major component of flare gas. A stepwise tracking of the evolution of particle properties from inside the flame to post-flame region was conducted on the bench-top flame to understand the underlying physical interactions that lead to the final state of particle emissions. This understanding can be very useful in interpreting and explaining the measurement results from the large turbulent diffusion flame.

It should be noted that without detailed information on the potential amounts or compositions of entrained aerosols in a flare stream during flowback operations, the goal of this work is to understand the potential effects of the former on particle emissions and their underlying mechanisms and the results should be interpreted within in the experimental range covered in this work.

Accordingly, the following are the sub-objectives of this study:

- To design and validate a high dilution sampling system to extract soot nanoparticles from a high-temperature reacting flow
- To study the stepwise evolution of size and morphology of particles from closed-tip and open-tip methane diffusion flames with and without entrained sodium chloride, which leads to an understanding of the interactions involved up to the final state of the particles
- To study the effect of flare size, exit velocity, and gas composition on the size distribution, effective density, morphology, and nano-structure of particle emissions from lab-scale flares
- To investigate the effect of entrained flowback liquid droplets on the size distribution, effective density, morphology, and mixing state of particle emissions from lab-scale flares

CHAPTER 2

High-dilution sampling system and experimental setup[2]

2.1 Introduction

In this chapter, we describe the bench-top scale burner (*i.e.* Santoro burner) that was used to produce a laminar diffusion flame. The main objective of using a small-scale flame was to understand the main steps in soot formation and how NaCl can affect that. In addition to Santoro burner, we also introduce the high dilution sampling system which was used to extract samples from high temperature reacting flows. Moreover, we describe the instruments used to characterize nanoparticles. Finally, the high dilution sampling system is characterized and validated for soot particles sampled from inside the laminar diffusion flame.

[2] This chapter is based on the following published journal articles:
- Kazemimanesh, M., Moallemi, A., Olfert, J.S., and Kostiuk, L.W. (2017). Probe sampling to map and characterize nanoparticles along the axis of a laminar methane jet diffusion flame. *Proc. Combust. Inst.*, 36(1):881–888.
- Moallemi, A., Kazemimanesh, M., Kostiuk, L.W., and Olfert, J.S. (2018). The effect of sodium chloride on the nanoparticles observed in a laminar methane diffusion flame. *Combust. Flame*, 188:273–283.

Intrusive techniques have been extensively used to investigate soot formation in combustion processes. One such technique is probe sampling, which has been employed for soot measurements from flames during the last few decades. This method offers the advantage of extracting samples directly from a known location in the flame and then using standard aerosol instruments to perform the measurement; however, concerns exist whether the measured sample is representative of that in the flow at the sample location due to the presence of the probe in the flow and flame (such as stagnation effects) and remains representative during the handling of the sample in tubing prior to measurement. For example, Burtscher *et al*. (1993) and Hepp and Siegmann (1998) investigated soot formation and its evolution in diffusion flames. They used a quartz micro probe that consisted of a tiny capillary for extracting soot particles and diluting them with an inert carrier gas. A differential mobility analyzer and an aerosol electrometer were used to obtain particle size distributions at different heights above the burner. On the other hand, Kasper *et al*. (1997) employed a stainless steel tube with a tiny pinhole as the sampling probe and measured particle size distributions from a diffusion flame doped with metallic additives. By using this probe, the particles extracted from the flame were rapidly diluted and cooled as a flow of nitrogen passed through the tube. The diffusion flames in Hepp and Siegmann (1998) and Kasper *et al*. (1997) used methane diluted with argon as the fuel. Higgins *et al*. (2002) used a similar sampling probe as Kasper *et al*. (1997) to investigate the oxidation rate of soot particles generated from an ethylene diffusion flame over a range of temperatures.

Probe sampling was also used extensively to investigate soot formation in premixed flames (Maricq *et al.* 2003; Zhao *et al.* 2003, 2005; Maricq and Xu 2004; Abid *et al.* 2008; De Filippo *et al.* 2009; Sgro *et al.* 2009; Camacho *et al.* 2015). In some of these studies, sampled soot particles were diluted in multiple stages to reach a high overall dilution and then directed to particle

measuring instruments (Maricq *et al.* 2003; Maricq and Xu 2004; Maricq 2011, 2012). Multi-stage dilution systems have the advantage of decreasing particle concentrations to within the measuring range of particle measurement instruments; however, such systems lack very high immediate dilution of the sample, which could result in changing the particle size distribution due to coagulation between particles if particle concentrations are very high, *e.g.* in a reacting flow. Zhao *et al*. (2003) pioneered an improved version of the probe sampling technique used by Kasper *et al*. (1997) and used it extensively to extract soot samples from ethylene premixed flat flames. Other studies have used a similar probe sampling method with multi-stage dilution for the study of nanoparticles in liquid fuel diffusion flames (Maricq 2011, 2012).

The use of probe sampling for investigation and characterization of soot nanoparticle evolution in a gaseous diffusion flame has not been tested. Therefore, the main objective of this chapter is to improve and characterize the probe-sampling technique for the investigation of the evolution of soot nanoparticles along the centerline of a methane laminar diffusion flame with high spatial resolution. Besides providing new data and insights on soot particle formation and evolution through a laminar methane diffusion flame, this work explores a large dynamic range of dilution ratio immediately after extraction to quantify what is required to maintain the integrity of the sample for measurement.

2.2 Experimental Setup

Figure 2.1 shows the schematic of the experimental setup. The experimental setup consisted of a co-flow diffusion flame burner, sampling and dilution system, particle measurement suite, thermophoretic sampler, temperature measurement system, and sodium chloride generation system. In the following sections, each component is explained.

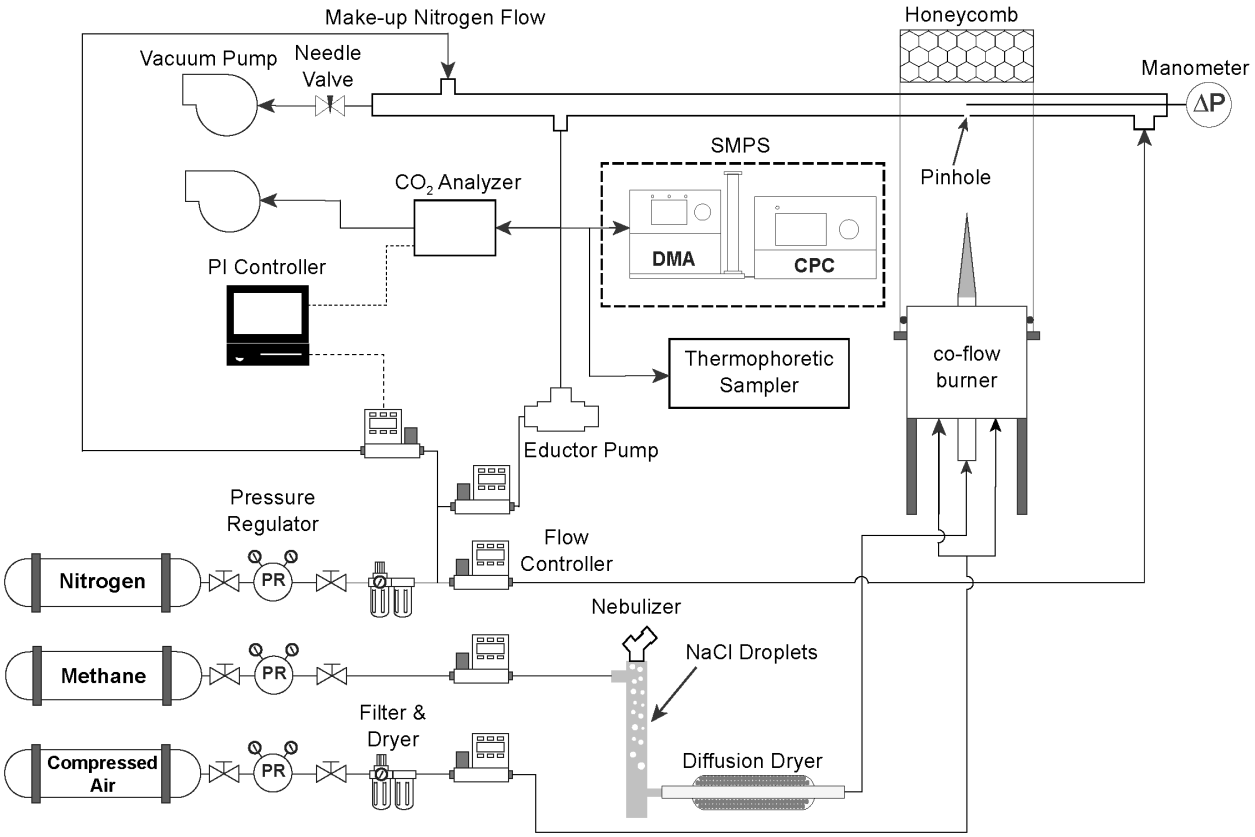

Figure 2.1: Schematic of the experimental setup showing the co-flow diffusion flame burner, the sodium chloride generation and injection system, the high-dilution sampling system, the aerosol measurement suite, and the thermophoretic TEM sampler.

2.2.1 Co-flow Burner

The co-flow burner used for the experiments was a well-studied co-annular burner described by Santoro *et al*. (1983). The burner consisted of two concentric tubes with internal diameters of 11.1 and 101.6 mm for fuel and co-flow air, respectively, which produced a stable laminar diffusion flame at atmospheric pressure. The inner tube and the outer tube were made of brass and aluminium, respectively. The fuel flowed through the inner tube and the co-flow air flowed through the co-annular section of the burner. The co-flow air at high flow rates also worked as a sheath to prevent the diffusion flame from flickering. To have a uniform flow of air, the co-annular section of the burner was fitted from bottom to top with a perforated distribution plate, a brass

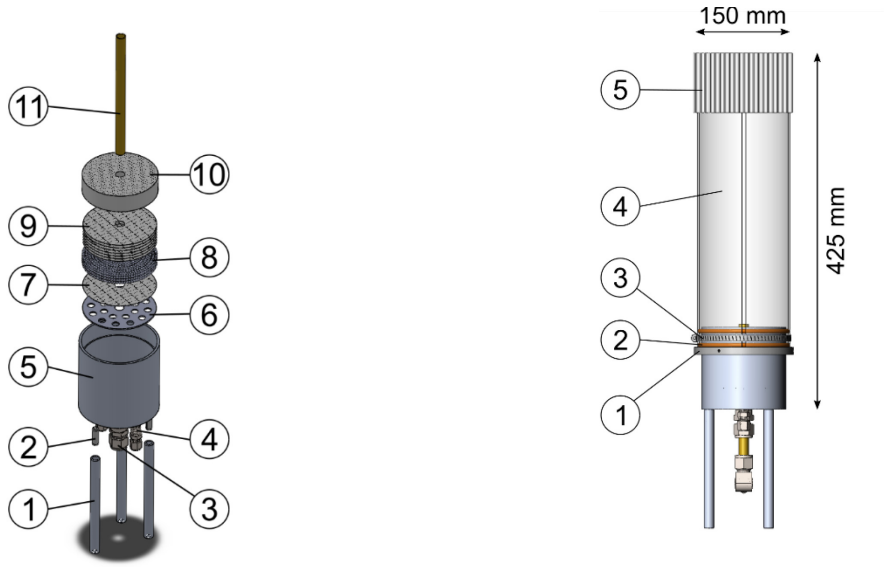

(a) (b)

Figure 2.2: (a) Exploded view of the Santoro burner showing 1: support legs, 2: spring pins, 3: fuel inlet fitting, 4: two air inlet fittings, 5: burner body, 6: air distribution plate, 7: brass mesh screen, 8: glass beads, 9: seven layers of brass mesh screens, 10: ceramic honey comb, and 11: fuel tube. (b) Side view of the burner assembly showing 1: holder ring, 2: O-rings, 3: worm-drive clamp, 4: quartz shield, and 5: ceramic honeycomb.

mesh screen (standard mesh size of 60×60 with openings of 250 μm), a 50-mm filling of glass beads (diameter of 3 mm), seven layers of brass mesh screen (a mix of standard mesh sizes of 40×40 and 60×60 with openings of 380 and 250 μm, respectively), and a 25-mm thick ceramic honeycomb with 1.5 mm cell size. Figure 2.2(a) shows an exploded view of the co-flow burner with its different components.

Methane was used as the fuel due to its lower sooting tendency compared to heavier hydrocarbons such as ethylene and because methane is commonly the main component of gas flares in upstream oil and gas industries. Methane and air flow rates in the burner were maintained at 0.35 and 70.0 SLPM (standard liters per minute at 25°C and 1 atm), respectively, by using two mass flow controllers (Cole-Parmer, Model 32907-71, and Omega, Model FMA-774A, respectively). All mass flow controllers in this setup worked based on the principle of laminar flow element (LFE). The volumetric flow rate of a gas in a laminar flow element (LFE) follows the Poiseuille equation

Figure 2.3: Image of the methane laminar diffusion flame.

and is linearly proportional to pressure drop. A differential pressure sensor is used to measure the pressure drop along a fixed distance of the LFE. This pressure drop, along with the viscosity of the gas, is used to accurately determine the volumetric flow rate. Separate absolute temperature and pressure sensors are incorporated and correct the volumetric flow rate to standard temperature and pressure defined earlier. The mass flow controllers were individually calibrated with a bubble flow meter (Sensidyne, Model Gilibrator-2). The mass flow controllers generally had an accuracy of less than 1% of reading and they were controlled by LabVIEW program via serial (RS-232) communication. These flow rates resulted in a stable diffusion flame with a visible height of 60 mm (Figure 2.3). The temperature of the edge of fuel tube was at ~450 K measured by a bare-wire thermocouple (Type K, Omega).

To avoid the entrainment of ambient air and to minimize the effect of room air currents, a quartz shield with diameter of 115 mm was mounted around the burner (Santoro *et al.* 1983) and a ceramic honeycomb placed atop of the shield to improve the stability of the flame, as mentioned in earlier studies (Saffaripour *et al.* 2011). Figure 2.2(b) shows the burner assembly with the quartz shield and the ceramic honeycomb. The shield consisted of two pieces of half-cylinder quartz glass with

a radius of 57.5 mm and a height of 300 mm, which were mounted on a holder ring fixed to the burner body by set screws. The two longitudinal narrow slots between the half-cylinders of the shield allowed vertical translation of the sampling probe in and out of the flame. Two O-rings were placed between the shield and the burner body and the shield was fixed to the burner by a worm-drive clamp. The burner assembly was mounted on two motor-driven translation (Velmex Inc., Model XN10-060-E01-21) stages with an accuracy of 0.03 mm for horizontal movement along the *x* and *y* axes.

2.2.2 Diluted Sampling System

To maintain the integrity of the extracted samples from high temperature reacting flows with very high particle concentrations, it is required to quench and dilute the sample immediately after extraction to prevent chemical reactions and particle-particle coagulation, respectively. The sampling probe consisted of a horizontal stainless steel tube (3.175 mm OD with wall thickness of 125 μm) with a downward-facing pinhole, with a diameter of 0.2 mm, positioned on the centerline of the flame. The sampling system was mounted on a separate motor-driven translational stage (Velmex Inc. Model XN10-0120-E01-21) with an accuracy of 0.03 mm for movement along the *z*-axis. The flame length was measured by using the sampling probe mounted on the vertical translation stage relative to the fuel tube exit plane. The pinhole was centered along the centerline of the burner before each test using the three translation stages by using a device that fits into the throat of fuel tube and has a centrally located needle on which to align the sample port. Dry, particle-free nitrogen was directed through one side of the probe and samples were extracted through the pinhole.

Using pinhole diameters smaller than 0.2 mm resulted in complete clogging of the pinhole by soot particles in a time less than the duration of a measurement with the particle measurement suite. At

heights above the burner (HAB) below 39 mm and above 55 mm, the concentration of the particles was low enough to make measurements possible with a 0.2 mm pinhole. On the other hand, for other HABs a probe with a 0.3 mm pinhole was used for sampling. It should be noted that due to gradual clogging, the pinhole was cleaned by a fine wire after each measurement.

The flow rate of the diluent nitrogen that flows through the sampling probe was set at 19.3 SLPM using a mass flow controller (Omega, Model FMA-5540), which was calibrated with a bubble flow meter (Sensidyne, Model Gilibrator-2). As illustrated in Figure 1, to establish a negative pressure throughout the sampling system, the downstream of the sampling probe was attached to a vacuum pump (GAST, Model DAA-P501) and the flow rate drawn into the vacuum pump was adjusted by a needle valve to ~23 SLPM by using the above-mentioned bubble flow meter. Make-up nitrogen flow was added to the main sampling line prior to the vacuum pump connection to control the extraction flow rate through the pinhole. The make-up nitrogen flow was controlled by a mass flow controller (Omega, Model FMA-2608A), which was calibrated with a bubble flow meter (Sensidyne, Model Gilibrator-2). Using an eductor pump (AIR-VAC, Model AVR093H), a fraction of the sample was drawn from the main sampling line through a branch placed between the pinhole and the make-up nitrogen. The portion of the sample that was drawn from the sampling line was subsequently directed to a low-range non-dispersive infrared CO_2 analyzer (Li-Cor 840), the particle measurement suite, and a thermophoretic sampler to collect particles on TEM grids. The CO_2 analyzer was calibrated for low CO_2 concentrations by using a calibration gas (Praxair) consisting of 48 ppm of CO_2 and a balance of nitrogen. The eductor pump was essentially a Venturi tube in which a flow of nitrogen at 10 SLPM set by a mass flow controller (Omega, Model FMA-775-V) passed through its inlet and generated the required negative pressure to extract the sample from the main sampling line.

To maintain a constant dilution ratio at a desired level (as defined in section 2.2.4), the concentration of CO_2 in the extracted sample was acquired and monitored by the CO_2 analyzer and, by using a PI controller tuned by the Ziegler-Nichols method (Ziegler and Nichols 1942), the make-up flow rate was manipulated such that the concentration of CO_2 remained at the desired constant level. A key feature of the sample probe was a 0.8 mm OD stainless steel tube inside the sampling probe, inserted from the upstream side, to measure the gauge pressure at the pinhole using a digital manometer (Dwyer, Model 475-1-FM). Previous studies (Zhao *et al.* 2003) measured upstream and downstream pressures in the sampling probe and used calibration of pressure drop as a function of distance to find the pressure at the pinhole location; however, the current method gave a direct reading of ΔP across the pinhole. By measuring the gauge pressure in the vicinity of the pinhole it could be verified whether sample was extracted through the pinhole or not and also maintain the sample extraction flow in the similar range under diluted and undiluted conditions (see Sections 2.2.3 and 2.2.4).

2.2.3 Undiluted Sampling System

To evaluate the amount of dilution during sampling, the ratio of the mole faction of a gas species of choice (CO_2 in this study) in both undiluted and diluted conditions was measured. Therefore, a sampling system was required to extract samples without diluting them. Figure 2.4 shows the sampling system for the undiluted condition.

Some modifications were applied to the diluted sampling system to change it into the sampling system for the undiluted condition. Instead of using the diaphragm pump for extracting the sample through the probe, the downstream sampling line was connected to the throat of an aluminum Venturi tube with inlet and throat diameters of 10 mm and 5 mm, respectively. The other end of the sampling line was capped. The Venturi tube acted as a pump when nitrogen flow passed

through it. The pressure drops at the throat of the Venturi tube drew an undiluted sample from the flame through the pinhole of the probe. Venturi tube was preferred to the diaphragm pump because of having a better control over the very low levels of suction in the probe (typically 250–500 Pa).

The sampled flow through the pinhole was passed through a high efficiency particulate air (HEPA) filter to remove the particulates, a tube filled with silica gel to remove water vapour content of the sample, and a wide-range non-dispersive infrared CO_2 analyzer (Gas Sensing Solutions, Model COZIR-20%) to measure CO_2 mole fraction. The wide-range CO_2 analyzer was zeroed with a pure nitrogen bottle and calibrated with a calibration gas bottle with 11.95% CO_2 (Praxair). The water content of the sampled gas in the undiluted sample was removed prior to the measurement of CO_2 mole fraction to avoid condensation of water vapour and undesired interference between absorption spectrum of H_2O and CO_2 in the CO_2 analyzer. The mole faction of CO_2 was measured at a ΔP across the pinhole similar to the diluted sampling condition (typically 250–500 Pa). At these low pressure differences, the mole fraction of CO_2 at a given height inside the flame was independent of the pressure difference and it was considered to be the representative mole fraction of CO_2 at that height. If the pressure difference is too small, the flow rate of the extracted sample decreases and it takes a longer sampling time for the instrument to reach to the steady-state mole fraction of CO_2, which could be interrupted by the clogging of the pinhole. If the pressure

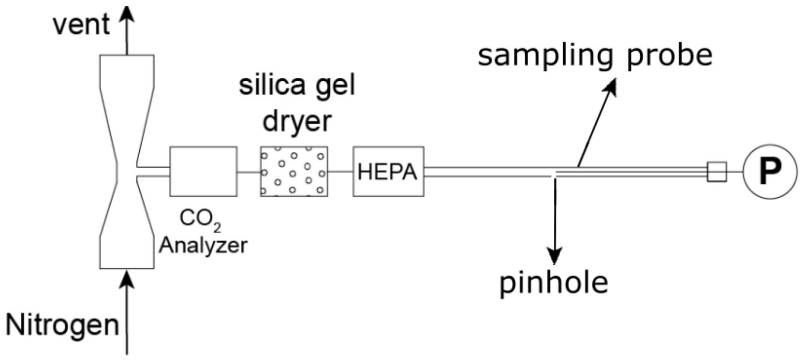

Figure 2.4: Schematic of the undiluted sampling system.

difference is too large, the extracted sample is not representative of the flow composition at the pinhole location. Thus, the pressure measured at the pinhole location was in a similar range during diluted and undiluted sampling.

2.2.4 Dilution ratio measurement

The mole fraction of CO_2 in the sample measured under diluted and undiluted conditions (as explained in Sections 2.2.2 and 2.2.3) can be used to estimate the dilution ratio of the sampling system. When sampling particles at very high concentrations from reacting flows, a dilution ratio on the order of thousands of times is required to prevent particle-particle coagulation and lower the particle concentration to within the measurement range of the particle measurement suite. To create that high of a dilution, the CO_2 mole fraction in the sample under diluted condition should be typically in the range of 5–80 ppm, which corresponds to a ΔP across the pinhole in the range of 250–500 Pa for a specific height above burner (HAB; height above the fuel tube exit plane). To measure the CO_2 mole fraction in the undiluted case for that specific HAB, the ΔP across the pinhole was maintained in the same range as the diluted case by controlling the inlet flow to the Venturi tube. By assuming that the pressure and temperature at the pinhole location were similar in both diluted and undiluted conditions for a specific HAB, it could be inferred that the composition of the extracted gas in the diluted and undiluted cases was similar. Therefore, the dilution ratio (DR) is defined as

$$DR = \frac{X_{\mathrm{CO_2,\ undiluted}}}{X_{\mathrm{CO_2,\ diluted}}} \tag{2.1}$$

where $X_{\mathrm{CO_2,\ undiluted}}$ and $X_{\mathrm{CO_2,\ diluted}}$ are the mole fraction of CO_2 in the undiluted and diluted samples at the same pressure and temperature, respectively. As mentioned in Section 2.2.3, the water content of the sample was removed in the undiluted sampling condition. Therefore, the CO_2

mole fraction measured by the CO_2 analyzer under the undiluted condition needed to be corrected for the removal of H_2O. The mole fraction of undiluted CO_2 can be written as

$$X_{\mathrm{CO_2,\ undiluted}} = \frac{n_{\mathrm{CO_2}}}{n_{\mathrm{CO_2}} + n_{\mathrm{H_2O}} + n_{\mathrm{other}}} \tag{2.2}$$

where $n_{\mathrm{CO_2}}$, $n_{\mathrm{H_2O}}$, and n_{other} are the number of moles of CO_2, H_2O, and other species (including N_2), respectively. However, the CO_2 analyzer under the undiluted condition measures the mole fraction of CO_2 with no water content, *i.e.*

$$X_{\mathrm{CO_2,\ undiluted,\ dry}} = \frac{n_{\mathrm{CO_2}}}{n_{\mathrm{CO_2}} + n_{\mathrm{other}}}. \tag{2.3}$$

Mitchell (1975) measured the mole fraction of different species for a burner geometry and flow conditions quite similar to our study. Mitchell's results showed that the mole fraction of CO_2 was approximately half the mole fraction of H_2O at different heights. Therefore, it was assumed that in this study, $n_{\mathrm{H_2O}} \approx 2n_{\mathrm{CO_2}}$. By replacing this assumption into Eq. (2.2), we obtain

$$X_{\mathrm{CO_2,\ undiluted}} \approx \frac{n_{\mathrm{CO_2}}}{n_{\mathrm{CO_2}} + n_{\mathrm{other}} + 2n_{\mathrm{CO_2}}} \approx \frac{X_{\mathrm{CO_2,\ undiluted,\ dry}}}{1 + 2X_{\mathrm{CO_2,\ undiluted,\ dry}}}. \tag{2.4}$$

When measuring the size distribution of particles, the mole fraction of CO_2 in the diluted sample was in the range of 5–10 ppm for most heights above the burner (corresponding to ΔP across the pinhole in the range of 250–300 Pa) to achieve dilution ratios of ~6,000 to ~13,000. At HABs where the concentration of particles were relatively lower (*i.e.*, near the closed tip of the flame where oxidation takes place), a lower dilution ratio was required and the CO_2 mole fraction in the diluted sample was in the range of 20–80 ppm, which corresponds to a ΔP up to ~500 Pa. This low of pressure difference drove a tiny flow rate through the pinhole, which caused minimal perturbation to the flame. An immediate dilution on the order of thousands of times with nitrogen

at ~300 K also ensured quenching of chemical reactions inside the probe. As mentioned in the introduction, some studies (Maricq *et al.* 2003; Maricq and Xu 2004; Maricq 2012) have achieved high overall dilution ratios by combining several low-dilution stages, which could possibly lead to coagulation of particles and change their size distribution.

Sample flow velocity, residence time, and the extent of coagulation of particles were estimated as outlined in Appendix A. Considering a typical dilution ratio of 10,000, the sample flow rate and flow velocity through the pinhole were ~0.13–0.16 cm^3/s and ~4–5 m/s, respectively, resulting in a residence time of ~30–50 μs across the pinhole. The residence time for particles in the sampling probe from the pinhole to the extraction branch for the particle measurement suite was ~2.1 ms. The maximum concentration of particles in the sampling probe after being diluted in the pinhole was ~3×10^7 cm^{-3}. The maximum coagulation coefficient was equal to ~19.6×10^{-10} cm^3/s (Hinds 1999, pp. 269–271), and the percentage of particles undergoing coagulation in the probe was always below 0.01%. The residence time from the extraction branch in the sampling probe to the particle measurement suite was ~0.78 s ensuring that coagulation of particles was always less than ~4.4% during transport to the particle measurement suite.

2.2.5 Particle measurement suite

To measure the size distribution of particles, a scanning mobility particle sizer (SMPS; TSI Inc., Model 3080) was used which consisted of a differential mobility analyzer (DMA; TSI Inc., Model 3085) and a condensation particle counter (CPC; TSI Inc., Model 3776).

Briefly, the aerosol particles pass through a bipolar charger (or neutralizer) where they undergo frequent collisions with bipolar ions due to the random motion of ions. The particles quickly reach a state of charge equilibrium, in which the particles carry a known bipolar charge distribution. This

process is known as *bipolar charging* or *neutralization*. In the equilibrium charge state the percentages of particles carrying no charge, single charge, or multiple charges of both positive and negative polarities are known. These aerosol particles are then directed to the DMA. The DMA consists of two concentric metal cylinders. The *polydisperse aerosol* and sheath air, both laminar flows, are introduced at the top of the DMA and flow down the annular space between the cylinders without mixing. The inner cylinder is maintained at a controlled negative voltage, while the outer cylinder is grounded. This creates an electric field between the two cylinders, which causes the positively charged particles to be attracted through the sheath air to the collector rod. Particles are precipitated along the length of the collector rod, with their exact location depending on the particle electrical mobility (see Section 1.4), the collector rod voltage, the flow rate of sheath air, and the DMA geometry. *Monodisperse particles*, with a narrow range of electrical mobility, exit through a small slit located at the bottom of the collector rod.

Monodisperse particles are then directed to the CPC, which counts the number of particles. The particles entering the CPC pass through a capillary tube with a nominal flow rate of 0.050 L/min. Particles exiting the capillary tube are exposed to clean sheath air saturated with butanol vapour. A wick soaked in butanol produces butanol vapour in a heated saturator (at 39 °C). The particles and saturated butanol vapour are directed to a condenser at 10 °C, where butanol vapour becomes supersaturated and condenses onto the aerosol particles to form larger droplets. The droplets pass from the condenser through a nozzle into the optical detector, where their number is counted based on light scattering signal from the droplets. By continuously classifying the particles of a certain mobility diameter and counting their number over a wide range of particle sizes, the particle size distribution can be obtained.

The aerosol and sheath air flow rates were set at 1.5 L/min and 15 L/min, respectively, for a full-width half-maximum resolution of one tenth the mobility set point and provided a particle sizing range of 2–60 nm. The scanning time for the SMPS was 40 seconds after ~10 min warm-up time for flame stabilization and the size distributions were corrected for diffusion losses in the sampling line and inside the SMPS. The particle diffusion losses in the SMPS were corrected using the algorithm used by Aerosol Instrument Manager software (AIM; TSI Inc., Version 9.0.0.0). The flow in the sampling probe was turbulent (with a Reynolds number of 8,930) while the flow in the transport tubing connecting the probe to the SMPS was laminar (with a Reynold number of 390). The particle diffusion losses in the sampling probe and the transport tubing up to the input of the SMPS were corrected using the correlations in Kulkarni *et al*. (2011, pp. 90–91) for each section based on the flow regime in that section.

2.2.6 Thermophoretic TEM Sampler

The morphology of sampled nanoparticles was studied using transmission electron microscopy (TEM). To do this, particles were collected on TEM grids using a custom-built thermophoretic TEM sampler from the University of British Columbia which was similar in principle and design to the sampler described in Rogak *et al*. (1993). In this sampler, the main mechanism of particle deposition was thermophoresis (*i.e.*, thermal force), which acts upon the particles in a temperature gradient and causes them to deposit on a colder surface. The thermophoretic sampler consisted of a preheating capillary tube which heated the particle-laden flow to 300 °C, a nozzle to direct the hot particle-laden flow over the TEM grid, and a colder surface at room temperature to hold the TEM grid directly under the nozzle. Thermophoretic deposition was the preferred method because it is not as size dependent as electrostatic, diffusional, or inertial deposition processes. The TEM grids used for collecting samples were ultra-thin carbon film (<3 nm thickness) supported by a

lacy carbon film on a 400 mesh copper grid (Ted Pella Inc., Product No. 01824). The thermophoretic sampler drew a portion of the diluted sample prior to being directed to the SMPS. The morphology of soot particles was investigated by analyzing TEM grids with a transmission electron microscope (JEOL Ltd., Model JEM 2100) operating at an accelerating voltage of 200 kV. Images were taken at high resolution using a Gatan CCD camera with a magnification of up to 1,000,000×.

2.2.7 Temperature measurement system

The temperature at different radial and axial positions of the reacting flow was measured with a bare wire type R thermocouple (Pt/13%Rh-Pt, Omega). The wire diameter was 75 µm and the junction size was approximately 190 µm (same order of magnitude as the pinhole size for sampling). The thermocouple was mounted on a holder similar to the one described in several previous studies (Cundy *et al.* 1986; McEnally *et al.* 1997), which is shown in Figure 2.5. The thermocouple mount comprised of two ceramic tubes with an outer diameter of 1.6 mm and lengths of 100 mm and 110 mm, which acted as a support for the thermocouple wire. The ceramic tubes

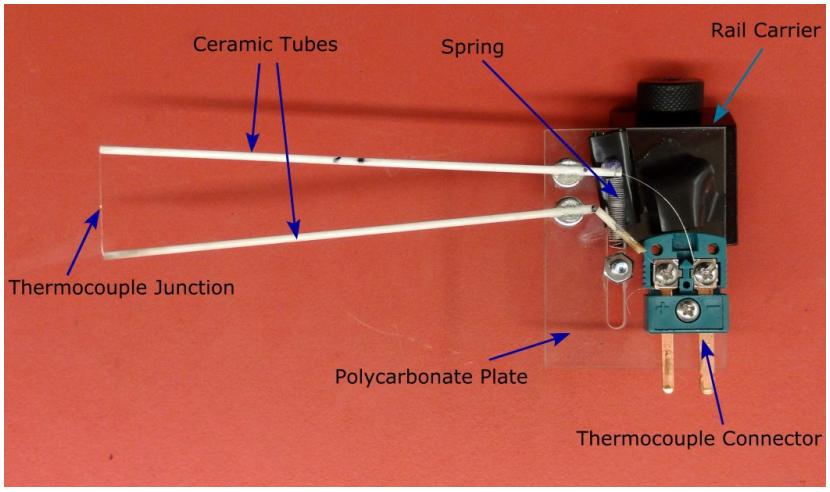

Figure 2.5: The thermocouple holder used for flame temperature measurement consisted of a bare-wire thermocouple, two ceramic tubes, and a soft spring. All parts were mounted on a polycarbonate plate attached to a rail carrier.

were attached to the head of two screws as mentioned in McEnally *et al.* (1997). One of the screws was tightened to a polycarbonate plate attached to a rail carrier (Thorlabs, Model RC1), while the other screw was allowed to pivot. A portion of the thermocouple wire between the ceramic tubes was exposed, while the two ends of the thermocouple wire were attached to a thermocouple connector on the polycarbonate plate. The thermocouple junction was adjusted at the middle of the exposed portion of the thermocouple wire. A spring was connected to the pivoting ceramic tube to keep the exposed portion of the thermocouple stretched and to prevent it from sagging due to thermal expansion under high flame temperatures.

Figure 2.6 shows the schematic of the temperature measurement system. The thermocouple mount was placed on an optical rail (Thorlabs, Model RLA0600) that made it possible to swiftly insert the thermocouple in the flame manually. This method of temperature measurement is known as rapid thermocouple insertion (McEnally *et al.* 1997). One end of the optical rail was attached to the motor-driven translational stage that was used for the vertical movement of the sampling and dilution system, which allowed the thermocouple to measure the flame temperature at different

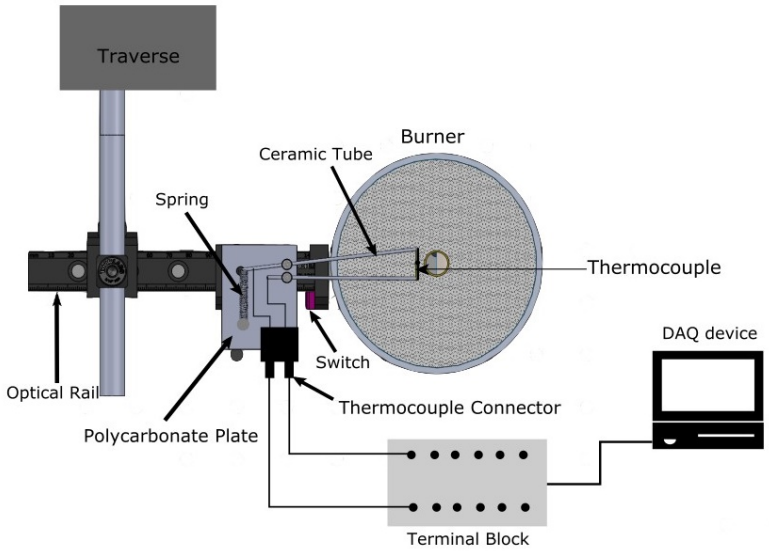

Figure 2.6: Schematic of the temperature measurement system, showing the thermocouple mount, optical rail, terminal block, and DAQ device.

axial positions. The location of the thermocouple junction was adjusted at the desired radial and axial position in the flow before each measurement. On the other end of the optical rail, a stopper with a switch was placed. Once the rail carrier reached the stopper, the switch was activated and the data acquisition system started collecting temperature data by using a LabVIEW program. The thermocouple connector was connected to a terminal block (National Instruments, Model SCB-68) and a data acquisition (DAQ) device (National Instruments, Model PCIe-6323). The terminal block had a thermistor which determined the cold junction compensation for the measured temperatures by the thermocouple and was initially calibrated with an ice bath. The temperature was logged at a sampling rate of 100 Hz. The temperature was measured at least four times at each location and was averaged to represent the temperature of the flow at that location. The measured temperature by the thermocouple was corrected for radiation losses based on the procedure explained by Shaddix (1999), which is explained in details in Appendix B.

2.2.8 Sodium Chloride Generation System

One of the objectives of this study, as it will be discussed in Chapter 3, was to understand the effect of sodium chloride on microphysical properties of soot particles from a flame. To introduce sodium chloride (NaCl) particles into the fuel flow prior to combustion, droplets of sodium chloride solution were first produced by atomizing an aqueous solution of NaCl (25% on mass basis) into the methane flow using a nebulizer (Aerogen Solo). The atomized droplets of NaCl solution were then passed through a diffusion dryer (TSI Inc., Model 3062) to remove its water content and form crystalline sodium chloride particles. By adding a relay to the nebulizer controller, the rate of NaCl droplets generation could be manipulated through variation of the duty cycle of the controller (Park *et al.* 2015). Figure 2.7 shows that the NaCl particles changed the colour of the flame and created a halo region around the flame with an intense yellowish-orange colour, which was determined

Figure 2.7: Image of the laminar diffusion flame with added sodium chloride particles

visually. To measure the mass concentration of NaCl particles injected into the flame, firstly, the size distribution of NaCl particles was measured with an SMPS directly attached to the fuel tube. Secondly, a centrifugal particle mass analyzer (CPMA, Cambustion Ltd; Olfert and Collings (2005)) was employed to derive the mass-mobility relationship of the generated NaCl particles. By combining the size distribution of NaCl particles at the fuel tube exit plane and their mass-mobility relationship, the mass distribution of the NaCl particles was obtained and, subsequently, the mass concentration of the NaCl particles at the fuel tube outlet prior to combustion was calculated to be ~45 ng/cm^3. The procedure of deriving the mass-mobility relationship of NaCl particles is explained in Appendix C.

2.3 Results and discussion

2.3.1 Effect of dilution on particle size distribution

A wide range of dilution ratios were used at each height above burner to investigate its effect on the measured particle size distribution (PSD). Particle losses or particle-particle coagulation can

change the particle size distribution. For low dilution ratios, where coagulation is significant, it is expected to measure larger particles with reduced number concentration. Once a critical dilution ratio is reached or the particle number concentration is sufficiently low, the effect of coagulation is negligible and the measured particle size and concentration becomes independent from the dilution ratio. Zhao *et al*. (2003) and Camacho *et al*. (2015) refined this probe sampling technique to achieve this criterion for premixed flames and we followed the same path to obtain the critical dilution ratio for the current diffusion flame. Figure 2.8 shows the variation in the dilution-corrected particle size distributions for HAB=38 mm when the dilution ratio was changed by more than an order of magnitude from ~800 to ~13,300. The total number concentration of particles was obtained from $N = DR \cdot N_{SMPS}$, where N_{SMPS} is the particle number concentration measured by SMPS. With low dilution ratio, the PSD was unimodal and no particles smaller than 3 nm were detected. As the dilution ratio was increased, the PSD started to become bimodal with a very large number of nanoparticles smaller than 2 nm (only a small fraction of the tail of the first mode in the range of 2–3 nm could be detected by the DMA). Note that the lower detection limit of the DMA

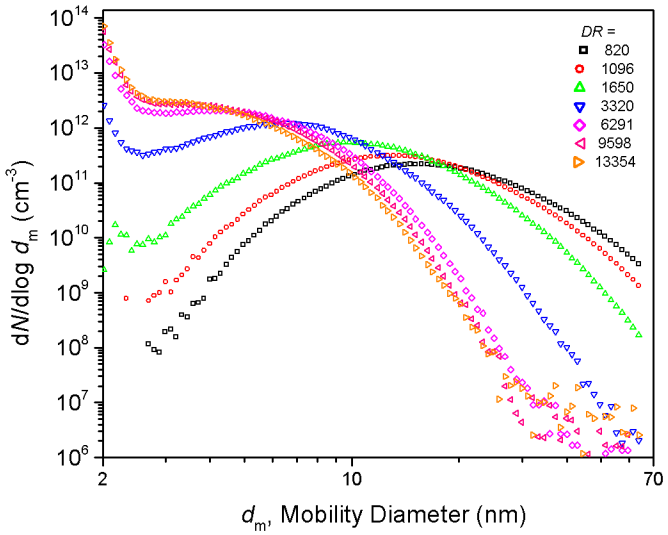

Figure 2.8: Variations of particle size distribution as a function of dilution ratio for HAB=38 mm.

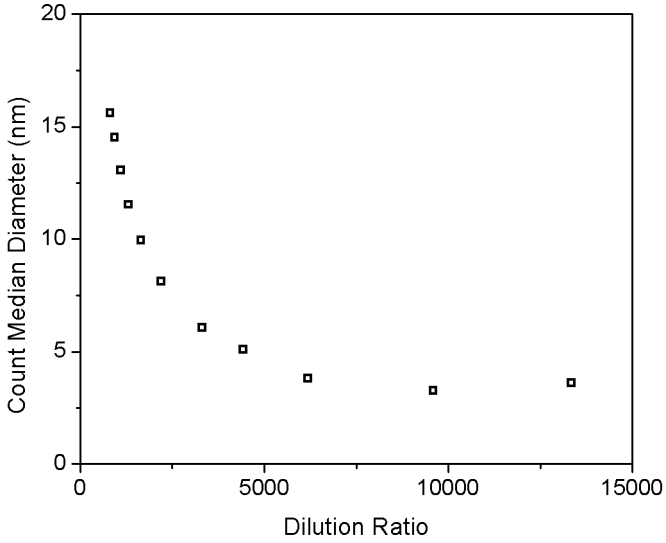

Figure 2.9: Particle size distributions for HAB=30–60 mm in the methane diffusion flame.

was 2 nm. Figure 2.8 shows that at dilution ratios greater than ~6,300 the PSDs become approximately independent of dilution ratio and converge to one dilution-independent PSD.

Figure 2.9 shows the change in the particle median diameter of the second (larger) mode of the size distributions of Figure 2.8 with variation in dilution ratio. This median diameter was calculated based on a bimodal lognormal fit of the measured PSD. Once the dilution ratio reached the critical value of ~6,300 for this specific HAB, the particle median diameter remained approximately constant. This is consistent with the findings of Zhao *et al*. (2003) and Camacho *et al*. (2015) for premixed flames. In the subsequent sections, only data obtained beyond the critical dilution ratio are presented, although not all HABs had the same critical dilution ratio.

2.3.2 Effect of pinhole clogging on particle size distribution

One of the practical drawbacks of sampling particles with a probe, was the clogging of the pinhole over time. Deposition and accumulation of soot particles on the wall of the pinhole as well as on the outer surface of the sampling tube in the vicinity of the pinhole caused gradual clogging of the pinhole reducing its effective diameter. Clogging typically continued until the pinhole was

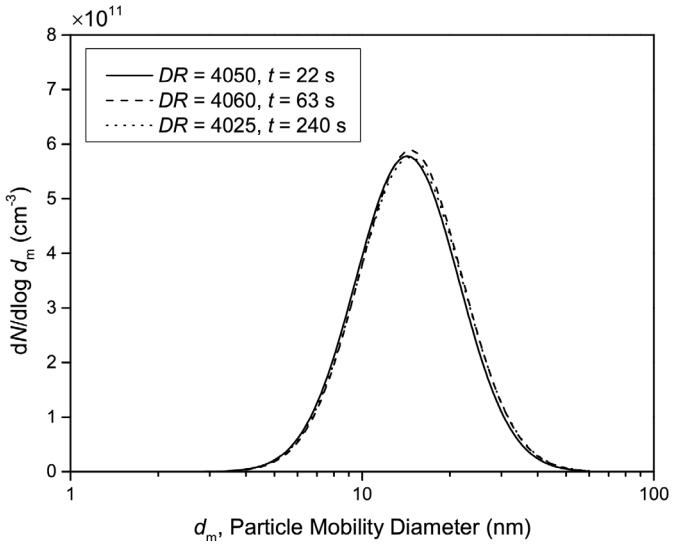

Figure 2.10: Effect of pinhole clogging on particle size distribution for HAB=41 mm. In the legend, *t* is the time after the clean pinhole was positioned in the flame and the SMPS scan started.

completely blocked and no CO_2 was measured by the analyzer. During clogging of the pinhole, online CO_2 measurements showed that CO_2 mole fraction decreased with time, an indication that sample flow rate through the pinhole was reduced. Moreover, online ΔP measurements revealed that, during clogging, slightly higher vacuum was measured inside the sampling probe due to the partial blockage of the pinhole. The PI controller described earlier in Section 2.2.2 changed the make-up nitrogen flow rate to keep the CO_2 mole fraction in the diluted sample at the desired constant level (for example, 10 ppm). It should be noted that when the pinhole was about to be completely clogged, the PI controller could not keep up with the reduction in CO_2 mole fraction and this led to a rapid complete blockage of the pinhole.

Due to this drawback, it was necessary to investigate the effect of pinhole gradual clogging on the measured particle size distribution. Figure 2.10 shows the effect of clogging on the measured PSD for HAB = 41 mm. We noted earlier that the dilution ratio affected the PSD considerably. To isolate the effect of dilution ratio, particle size distribution was measured at a specific constant CO_2 mole fraction (*i.e.*, dilution ratio) while the pinhole was lightly, moderately, or heavily

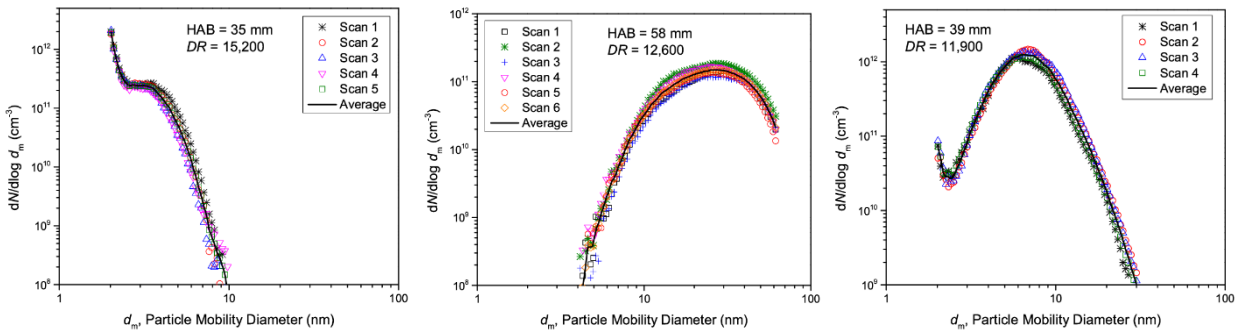

(a) (b) (c)

Figure 2.11: Particle size distribution at representative HAB = 35, 58, and 39 mm for *DR* = 15200, 12600, and 11900, respectively. Marker points show different SMPS measurements and solid lines represent the average particle size distribution.

clogged. The required time for complete blockage of the pinhole in this set of tests was ~300 s. The amount of clogging is indicated by the time after the clean pinhole was positioned in the flame and the SMPS scan started. It is clear from Figure 2.10 that the amount of clogging did not have a considerable effect on the particle size distribution. This fact provided ample time for the PI controller to reach the desired set point for the CO_2 mole fraction (~30–60 s) and measuring PSD as long as the pinhole was not completely clogged. Figure 2.10 also confirms that once a certain dilution ratio was maintained in the diluted sampling system, highly reproducible particle size distributions could be obtained regardless of time or degree of pinhole clogging (also see Figure 2.11).

2.3.3 Validation of particle size distributions in the flame

Particle size distributions for different heights above the burner along the centerline of the flame were obtained. The purpose of this part of the study was to create a detailed map of nanoparticles across the laminar diffusion flame and investigate particle evolution along the centerline of the flame.

Figures 2.12 – 2.14 show the particle size distribution for HAB from 30 mm to 62 mm. For the sake of clarity, the particle size distributions are broken into three plots to better represent the trends in particle evolution. Below HAB=30 mm, the SMPS could not detect any particles. At the onset of particle nucleation at the height of 30 mm (Figure 2.12), a small fraction of the tail of the PSD could be detected which mostly consisted of nanoparticles smaller than 2 nm (below the lower detection limit of the DMA). At 35 mm, the PSD became bimodal, with a larger diameter mode. Like before, only a fraction of the tail of the first mode could be detected which consisted of particles smaller than 3 nm; however, the number of particles in this mode was much more than that of the second mode. At higher heights above burner until 38 mm, the second mode increased in both particle mobility diameter and number concentration as the first mode gradually disappears. By fitting the bimodal PSDs with two lognormal distributions, the median diameter of the second mode is estimated to change from ~3 nm to ~6 nm when the HAB was changed from 35 mm to 38 mm. The PSDs show particle nucleation at lower heights and the coagulation of these nucleated nanoparticles at higher heights to form larger particles with reduced number concentration.

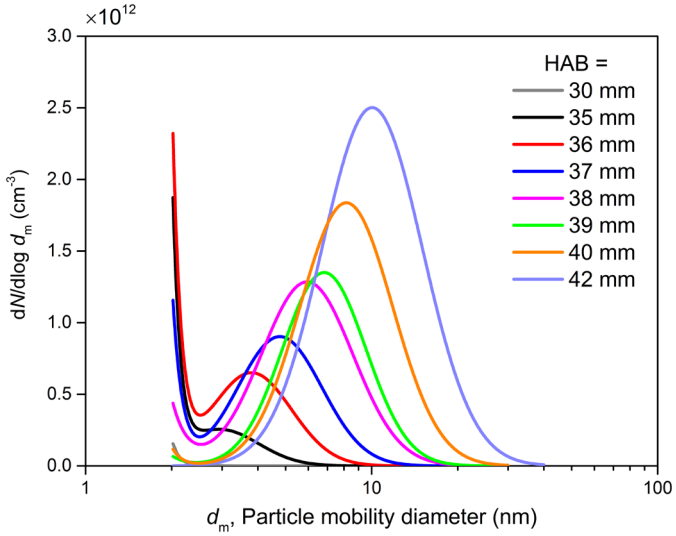

Figure 2.12: Particle size distributions for HAB=30–42 mm.

At heights of 39 to 42 mm (Figure 2.12), the PSD was mostly unimodal with both its median diameter and number concentration growing as HAB increased. The particle median diameter grew to ~10 nm for the height of 42 mm. Closer investigation of these PSDs revealed that they included the tail of the small first mode, which decreased with height above the burner. It should be noted that the geometric standard deviation, σ_g, of the PSD from the heights of 39 to 42 mm varies from 1.44 to 1.50, which is larger than $\sigma_g = 1.44$ for a self-preserving distribution in the free-molecular regime (Lai *et al.* 1972). Zhao *et al*. (2003) have mentioned that this is indicative of particle growth not only by coagulation, but also by surface growth due to surface reactions with existing polycyclic aromatic hydrocarbons (PAH) (Frenklach and Wang 1991).

Several studies (Zhao *et al.* 2003, 2005; Abid *et al.* 2008) on premixed ethylene flames reported the same bimodality of the PSD in these flames; however, they found that the first mode of the PSD was persistent throughout the flame and did not gradually disappear. They argued that for lightly sooting premixed flat flames, particle nucleation was an ongoing process throughout the flame height and the rate of continuous nanoparticle nucleation at different heights was in balance with their rate of consumption for coagulation into larger particles. However, for the diffusion flame in the current study, gradual diminishing of particle nucleation could be seen in the region of particle surface growth and it seemingly did not continue throughout the flame height. This result is consistent with the findings of Zhao *et al*. (2007) for a rich ($\Phi = 2.5$) premixed ethylene flame, where particle nucleation seems to stop at a certain HAB.

From the height of 42 mm to 43 mm, the particle median diameter continued to grow from 10 nm to 11.3 nm while their number concentration decreased (see Figure 2.13). At HAB=44 to 48 mm, the unimodal PSD became bimodal again. We call the left-most mode as Mode I and the right-most mode as Mode II. With increasing height in this region of the flame, the median particle size

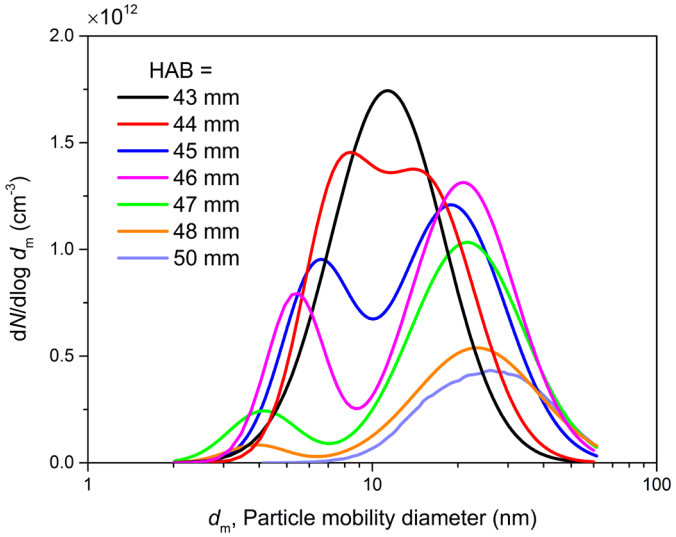

Figure 2.13: Particle size distribution for HAB=43–50 mm.

in Mode II grew larger in diameter from 15 nm to 23.3 nm, while they became smaller in diameter in Mode I, and both Modes I and II decreased in number concentration. At the height of 50 mm, Mode I vanished and only Mode II survived. This is an interesting evolution for the particles, which to our knowledge, has not been reported before for diffusion flames but has been observed in premixed flames in the literature. For example, Maricq *et al*. (2003) reported bimodality of the PSD at mid-range heights in rich ($\Phi = 2.06$) premixed ethylene flame in a McKenna burner. Also, Maricq (2006) showed that such bimodality was present in the PSD of premixed flames of other fuels such as ethane, acetylene, and benzene/acetylene, with the trough of two modes typically occurring at ~10 nm or smaller diameters. Presumably, the particles in Mode I and Mode II continue to coagulate and form larger particles in Mode II in smaller numbers.

At the heights of 50 mm to 55 mm (Figure 2.14), the PSD was unimodal and the median particles continued to grow to ~30 nm and their number concentration decreased due to coagulation. From the height of 57 mm to the closed tip of the flame at HAB=61 mm (Figure 2.14), the median particle diameter sharply decreased from ~30 nm to ~9 nm while its number concentration dropped

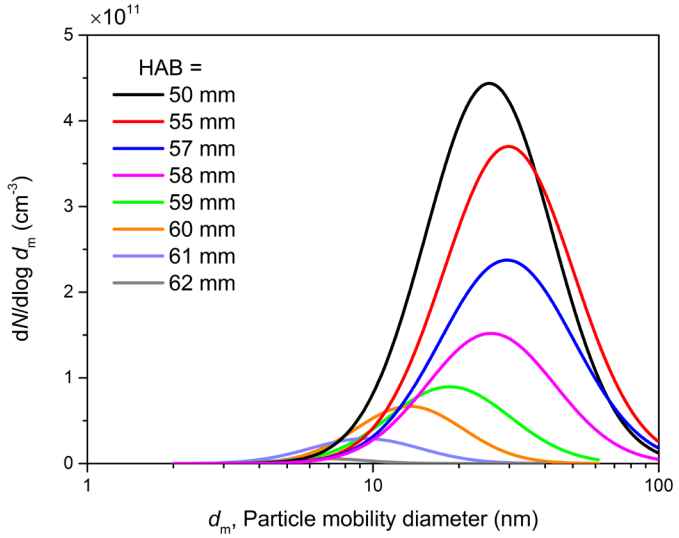

Figure 2.14: Particle size distribution for HAB=50–62 mm.

significantly, due to particle oxidation. At HAB=62 mm, just outside the tip of the flame, the particles continued to shrink in size and their number concentration was greatly reduced.

Hepp and Siegmann (1998) reported the general trend of particle evolution from nucleation (inception) and surface growth to coagulation and oxidation in a lightly sooting methane/argon diffusion flame; however, they did not observe the bimodal distribution during particle nucleation as well as at mid-range heights. This could be possibly due to the low dilution ratio of 400:1 used in their study; when we lowered the dilution ratio in our setup at these heights, the bimodality of PSD disappeared and a unimodal distribution was observed.

2.4 Conclusions

Nanoparticles generated by combustion of methane in a laminar jet diffusion flame were characterized systematically by direct sampling through the pinhole of a probe and sizing them with a DMA. Particular attention was paid to verify the validity of probe-sampling technique in measuring nanoparticles from highly reacting flows. A method for the measurement of dilution ratio was introduced by measuring CO_2 mole fraction continuously during the tests for diluted and

undiluted samples, which could substitute other methods of determining dilution ratio based on computation or offline measurement of CO_2 concentration. Analytical and experimental results showed that particle-particle coagulation, which is a challenge for particle size distribution measurement, was negligible in this study. The effect of dilution ratio on the shape of the particle size distributions was characterized, confirming that particle size distributions became independent from the dilution ratio when using very high and immediate dilution. Moreover, it was shown that the degree of clogging of the pinhole had no considerable effect on the measured particle size distribution.

Size distributions of particles larger than 2 nm were obtained for various heights above burner, covering early nucleation and surface growth to coagulation and oxidation regions. It was found that the PSD in the nucleation region was bimodal and gradually turned into a unimodal PSD due to particle growth. At the height of 44 mm above the burner, the PSD started to become bimodal again with the second mode growing in diameter and the first mode gradually decreasing in size until it vanished. It is speculated that particles in the first mode were consumed for coagulation with particles in the second mode to form particles with a median diameter of up to 30 nm. At the height of 57 mm, particles started to oxidize gradually until the tip of the flame where they reached a median diameter of 9 nm and in very low concentrations.

CHAPTER 3

The Effect of Sodium Chloride on the Nanoparticles Observed in a Laminar Methane Diffusion Flame[3]

3.1 Introduction

In this chapter, we use the bench-top burner and the high dilution sampling system introduced in Chapter 2 to study the effect of sodium chloride on soot formation and evolution in a close-tip laminar methane diffusion flame. We used methane as the fuel because it comprises a major fraction of the gas flares. Sodium chloride was also chosen because both sodium and chloride ions are the most abundant ions found in flowback fluids. The experiments in this chapter shed light on how sodium chloride affects the fundamental interactions between soot particles during their inception, coagulation, and agglomeration, which is useful in explaining the microphysical properties of particle emissions from lab-scale large turbulent diffusion flames (Chapter 6).

[3] This chapter is based on the following published journal articles:
- Moallemi, A., Kazemimanesh, M., Kostiuk, L.W., and Olfert, J.S. (2018). The effect of sodium chloride on the nanoparticles observed in a laminar methane diffusion flame. *Combust. Flame*, 188:273–283.

Soot formation and evolution have been extensively investigated in different experimental and theoretical studies. One less-investigated area of research is regarding the effect of additives on the process of soot formation. Alkaline and alkaline earth metals are two categories of additives that affect soot formation and evolution and have been investigated for more than three decades (Haynes *et al.* 1979; Bonczyk 1983, 1988; Mitchell and Miller 1989; Tappe *et al.* 1993; di Stasio *et al.* 2011). Haynes *et al*. (1979) measured the volume fraction and number density of the soot particles in a premixed ethylene flame while adding alkaline salts to the flame by employing laser light extinction and scattering methods. They found that the addition of alkaline salts, such as sodium and potassium chlorides, lead to a significant increase in the number concentration of soot particles. They argued that the increase in the number concentration of soot particles is due to charge interactions between soot particles and alkaline ions inside the flame. Bonczyk (1983) investigated the effect of alkali chlorides on soot formation in a propane diffusion flame by measuring the size and number concentration with Mie scattered laser radiation. Results obtained by Bonczyk (1983) shows that these additives caused an increase in the number concentration and a decrease in the size of soot particles. Mitchell and Miller (1989) found that the addition of alkaline salts to a diffusion ethylene flame resulted in the neutralization of predominantly positive soot particles. Most of the techniques used in these investigations were laser and optically based methods.

Extractive sampling is a conventional method which has been employed in studies related to soot formation and emission from combustion sources (Burtscher *et al.* 1993; Hepp and Siegmann 1998; Maricq *et al.* 2003; Zhao *et al.* 2003; Abid *et al.* 2008; Maricq 2011; Camacho *et al.* 2015). In this method, a probe is being used to extract a sample and send it to particle measurement instruments. Numerous studies used extractive sampling techniques in conjunction with a scanning

mobility particle sizer (SMPS) to measure the size distribution of particles at different stages of soot formations. Hepp and Siegmann (1998) developed a probe sampling technique to extract and dilute the samples from a diffusion flame and investigated the changes in particle size distribution extracted from different heights above the burner (HAB). The extractive technique used by Hepp and Siegmann was refined by Zhao *et al*. (2003). Their sampling system has the advantage of providing a larger dynamic range of dilution for the extracted samples. Sampling systems similar to the one developed by Zhao *et al*. have been extensively used in numerous studies (Zhao *et al.* 2007; Abid *et al.* 2008; Camacho *et al.* 2013, 2015) to study soot particle evolution in flames.

To the best of our knowledge, there has been little research on the effects of addition of sodium chloride particles on soot formation and evolution in a diffusion flame using scanning mobility particle sizer (SMPS). In this study, probe sampling in conjunction with SMPS and transmission electron microscopy (TEM) was employed to provide a better understanding of the observed nanoparticles (soot and non-soot particles) along the centerline of a laminar methane diffusion flame, when sodium chloride is entrained in the fuel flow. Compared to the other techniques used in previous studies, the use of SMPS and TEM make it possible to measure the particle size distribution and probe particles as small as 2 nm from within the flame. Additionally, such phenomena as coagulation between particles and changes in particle structure can be tracked using the SMPS and TEM results.

3.2 Results and Discussions

3.2.1 Temperature measurements

3.2.1.1 Temperature Profiles of the Methane-only and Methane-NaCl Flames

The process of soot nanoparticle formation is significantly affected by temperature. An understanding of nanoparticle formation in a laminar diffusion flame cannot be achieved unless

the temperature of the reacting flow is determined. The temperature profiles from the flame centreline to a radial position of 8 mm (with 1 mm increments) for selected heights above burner from 1 mm to 60 mm (with 5 mm increments) were measured for the cases of the methane diffusion flame and the methane diffusion flame doped with NaCl particles (hereinafter, as methane-only flame and methane-NaCl flame). The temperature profile at different HABs along the centerline of the flame is shown in Figure 3.1. Temperature at each location was measured at least four times and the average of the measured temperatures is illustrated in Figure 3.1. All temperatures were corrected for radiation losses and the maximum uncertainty of the measured temperatures was ±40 K based on the propagation of precision and bias uncertainties. Based on these results, the spatial temperature fields are quite similar for both methane-only and methane-NaCl flames, with the minimum and maximum difference being 13 K and 40 K, respectively.

Figure 3.2 is a contour plot of measured flame temperatures for the methane-NaCl flame and it is based on the temperatures acquired at various radial positions (1 mm apart) at different HABs (5 mm apart). The temperature between the measured points was estimated by interpolation. The black and red lines in the contour plot demonstrate the locus of bulk sodium chloride melting and

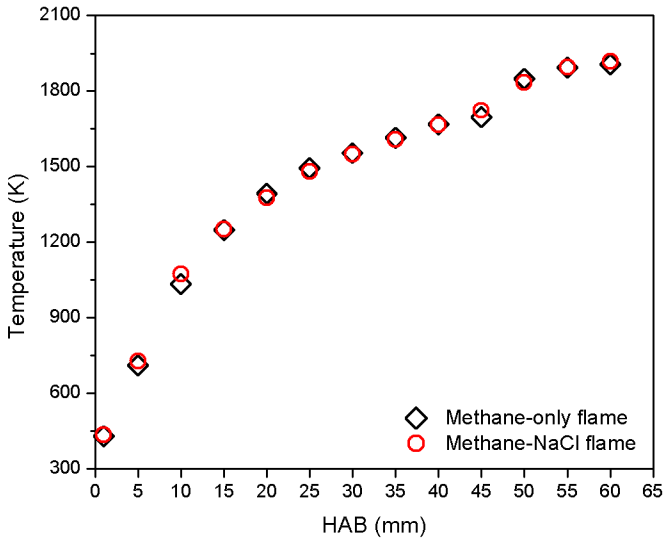

Figure 3.1: Axial temperature profile of flame methane-only and methane-NaCl flames. The visible flame height was 60 mm.

boiling points at 101 kPa, respectively (see Section 3.2.3 for the effect of particle size on its melting and boiling point). The dashed line is an approximate locus of the visible flame surface.

A point worth making about the observed steady-state scalar field of temperature is that there are a wide range of gradients in both the radial and axial direction which superimpose the transport of sensible energy by conduction on top of the convection in the flow. Similar gradients will exist in other scalar fields, such as the particle number concentration that will be measured in a following section. Therefore, the measured local magnitude of any quantity (such as the particle size distribution) is a balance between the convective and diffusive transport in both the axial and radial directions, as well as the local source/sink processes.

3.2.1.2 Effect of Sampling Probe on Flame Temperature

The insertion of the sampling probe into the flame disturbs the temperature profile and will reduce the temperature near the vicinity of the sampling probe; therefore, it is necessary to investigate the effect of the probe on the flame temperature as it could potentially affect the formation and

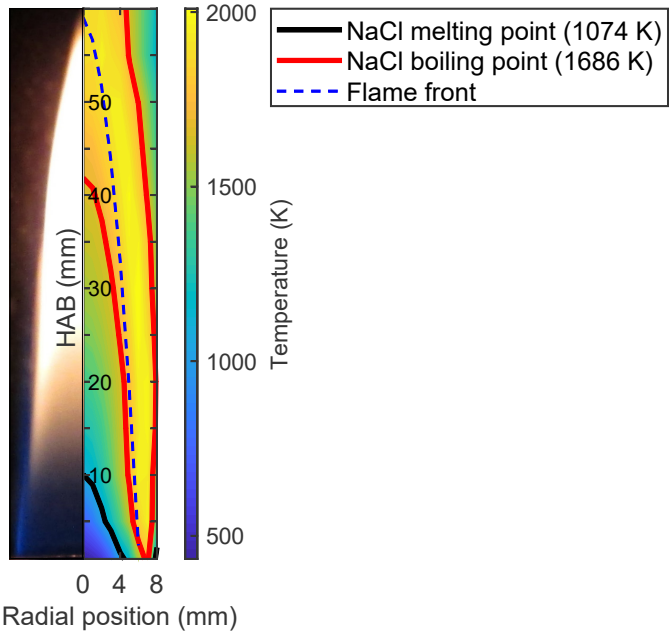

Figure 3.2: Picture of flame and contour of flame temperature (K) in methane-NaCl flame.

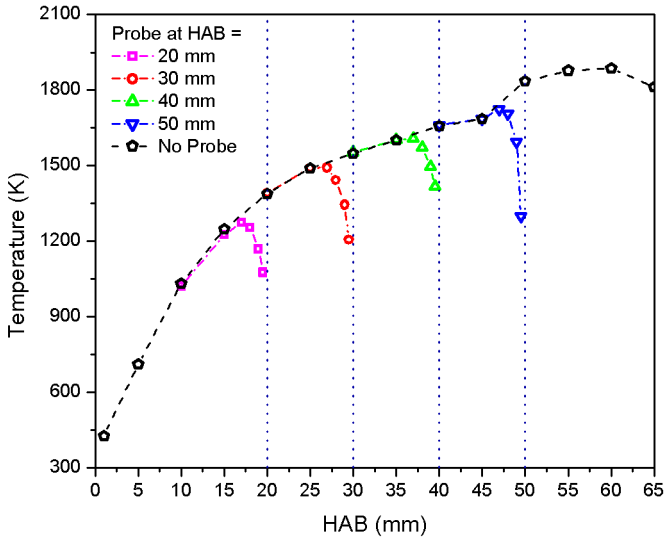

Figure 3.3: Temperature measured along the centreline of the methane-only flame with and without the probe. The vertical lines show HABs where the probe was inserted.

evolution of nanoparticles. This investigation was done by placing the sampling probe at several HABs and measuring the temperature along the centerline of the flame from 0.5 mm to 10 mm upstream of the location of the probe. Figure 3.3 demonstrates the temperature profiles along the centreline of the flame for the case of probe inserted at different HABs as well as the temperature of the undisturbed flame. The vertical lines are the HABs where the probe was inserted while the temperatures for locations upstream of these HABs were measured.

The results show that the insertion of the probe reduced the temperature of points that are located approximately 3 mm upstream of the probe. Such temperature drop was significant and as high as ~600 K in the vicinity of the sampling probe. The observed temperature trend is similar to the results obtained by Zhao *et al*. (2003), which reported a decrease in local flame temperature in a region 3 mm upstream of the probe. They argued that the local temperature drop is an intrinsic disadvantage of probe sampling which results in a decrease in the rate of chemical reactions. Abid *et al*. (2008) used probe sampling with an SMPS and thermocouple densitometery (which does not disturb the flame significantly) and found that soot volume fractions were similar if the HAB of

the SMPS results were shifted 3.5 mm downward; presumably because the probe slows reactions near the probe.

3.2.2 Nanoparticles in the Methane Diffusion Flame

Size distributions of particles along the centreline of the methane-only flame were measured at different HABs to provide an understanding of the evolution of nanoparticles in the flame when no NaCl particle was added to the fuel flow prior to combustion. The observed spatial rate of

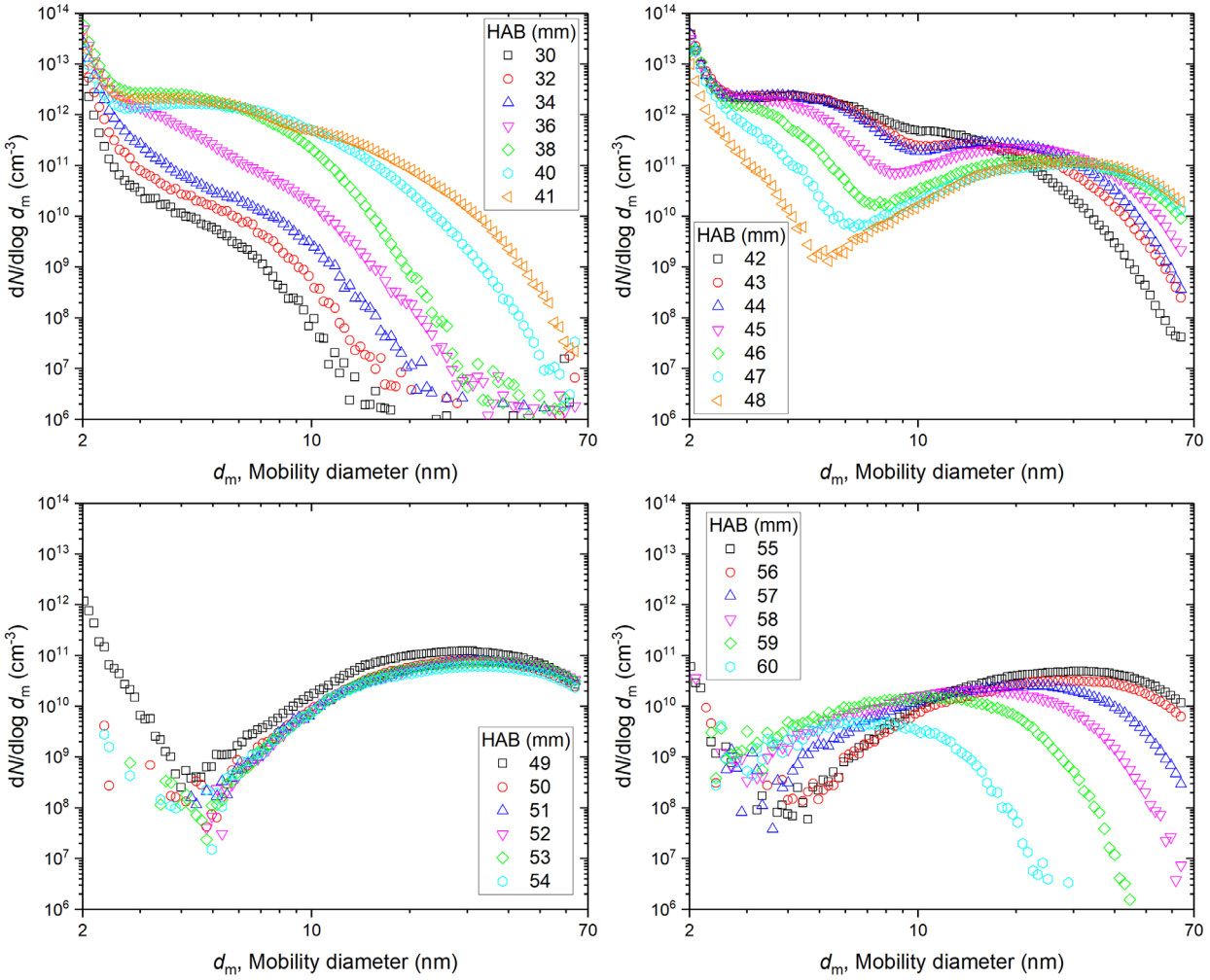

Figure 3.4: Particle size distributions for HAB=30–60 mm in the methane diffusion flame. The top left panel covers the soot inception and surface growth region of the flame (HAB = 30–41 mm), the top right panel covers the coagulation region of the flame (HAB = 42–48 mm), the bottom left panel covers the agglomeration region (HAB = 49–54 mm), and the bottom right panel covers the oxidation region (HAB = 55–60 mm).

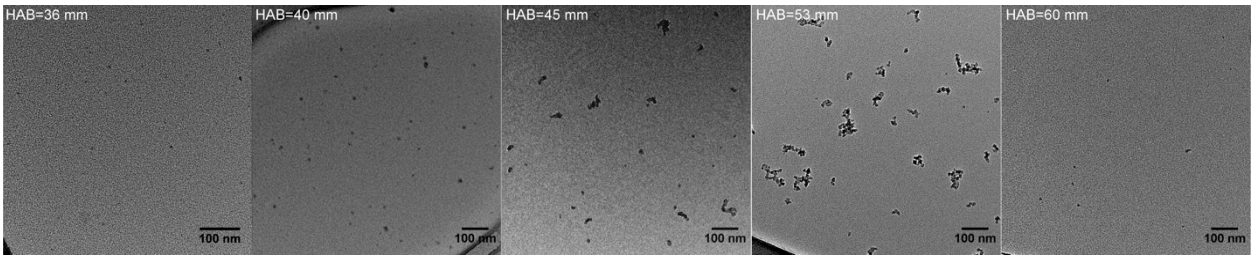

Figure 3.5: TEM images of particles sampled at different representative HABs in the case of methane-only flame.

change of particle size distribution significant, and four ranges of HABs were chosen to display the results in Figure 3.4. Additionally, a representative TEM image of the sampled nanoparticles from each of these HAB ranges is shown in Figure 3.5, except for the lowest HAB range where two images were needed to characterize the changes observed.

The SMPS started to detect particles at HAB=30 mm. The size distribution at HAB=30 mm seems to consist of two different portions: a mode which seems to have a median size smaller than 2 nm which could be associated with the insipient soot particles that were either formed locally or transported to this location by diffusion, and an emerging trough for particles sizes between 3 to 10 nm. As HAB increased, particles with mobility diameters greater than 3 nm grew in size and concentration, which led to the formation of a distinguishable mode for particles larger than 3 nm at HAB=38 mm. Herein, the smaller mode will be called the inception mode and the larger mode will be called Mode I. The formation of Mode I could be due to surface growth of incipient soot particles. The TEM image of sampled particles at HAB=36 mm (Figure 3.5) suggests that the particles (the small dark circular shapes in the figure) are individual non-aggregate soot particles. Figure 3.6 shows high resolution TEM (HRTEM) images of particles at HAB=40 and 41 mm. The HRTEM images show that the soot particles at these HABs have single or multiple core-shell structure. The core-shell structure of soot particles has also been reported in other studies (Chen and Dobbins 2000; An *et al.* 2016; Botero *et al.* 2016).

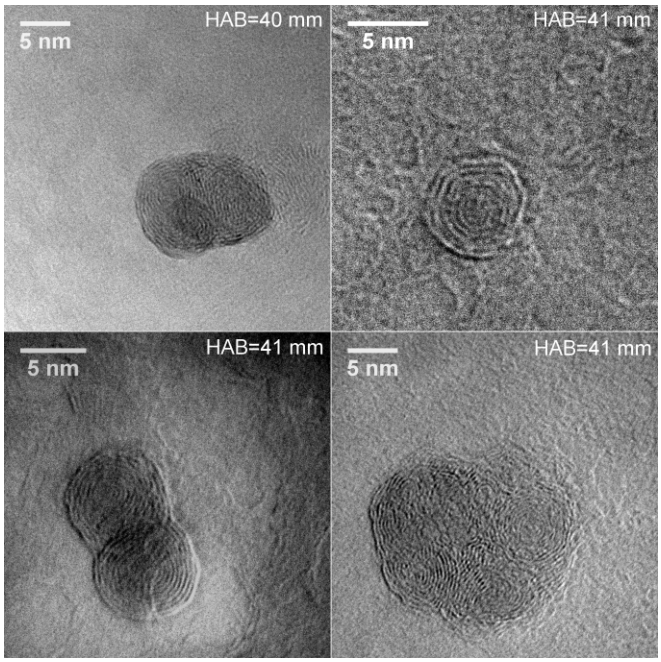

Figure 3.6: HRTEM image of particles at HAB=40 and 41 mm from the methane flame.

At HAB=42 mm, particles with mobility diameter greater than 10 nm begin to form another mode with a size of ~ 30 nm. Hereafter this mode is referred to as Mode II. In the height range of 44 to 48 mm, the median particle size in Mode II became larger while the particles in Mode I became smaller in diameter, and both Modes I and II decreased in number concentration. As also suggested in Chapter 2, this indicates that the particles in Mode II underwent coagulation. Moreover, presumably a higher rate of coagulation between incipient soot particles and particles associated with Mode II resulted in size growth of Mode II particles. On the other hand, particles in Mode I which could be generated by the coagulation between incipient particles, starts to reduce in number and vanishes, as most of the incipient particles coagulate with larger particles from Mode II at higher HABs.

This trend continued until HAB=48 mm, where Mode I vanished and only the larger particles in mode II survived on the centerline. It should be noted that the number concentration of the particles in the inception mode remained more or less unchanged up to HAB=48 mm; however, at HAB=49

mm, their number concentration dropped by an order of magnitude and, at higher HABs, their number concentration was further reduced by another two to three orders of magnitude over a relatively short distance. The TEM image of particles at HAB=45 mm (Figure 3.5) demonstrates that at this height the soot population is a blend of large aggregates and individual primary soot particles which is an indication that particles in this region of the flame experience coagulation and growth in size.

At the heights of 50 mm to 52 mm, the size distributions were approximately unimodal and the median diameter of particles continued to grow to ~33 nm while particle number concentration decreased, likely due to coagulation. The TEM image of particles at HAB=53 mm (Figure 8) shows that the majority of particles have aggregate-like structure which is an indication that the dominant process that particles experience in this HAB is coagulation.

Particle size distribution results show that from HAB = 54 mm to the tip of the flame (~60 mm), the median particle diameter sharply decreased from ~32 nm to ~7 nm while its number concentration dropped significantly by an order of magnitude, presumably due to particle oxidation. The TEM image of the particles (Figure 3.5) also shows a considerable change in the structure of particles from an aggregate-like structure at HAB=53 mm to mostly small, individual particles at HAB=60 mm.

3.2.3 Nanoparticles in the Methane-NaCl Diffusion Flame

The sodium chloride particle size distribution at the fuel tube outlet was measured by connecting the fuel tube directly to the SMPS with a conductive tube (*i.e.*, there was no flame and no dilution; for safety reasons the carrier gas flow was nitrogen and not methane) which is demonstrated in Figure 3.7 for which HAB = 0 mm represents the NaCl at the burner inlet measured without the

flame. The structure of the injected NaCl particles into the flame is shown in Figure 3.10. The median size of the NaCl particles was ~130 nm and the TEM image (HAB = 1 mm) shows that the NaCl particles injected into the fuel flow had a cubic structure.

Similar to the methane-only flame, particle size distributions at different heights above the burner were measured in the methane-NaCl flame. The size distributions for HAB=8 to 26 mm are shown in Figure 3.7 (Note the approximate four orders of magnitude difference between the number concentration of injected NaCl particles and the particles observed at HAB=8 to 26 mm). Adding NaCl to the fuel results in the emergence of considerable number of particles above HAB=8 mm. Recall that there were no particles detected in methane-only flame below HAB=30 mm. For these particles, the size distributions appear to be unimodal with a positive skew. By increasing HAB, the size and number concentration of these particles reached a maximum at HAB=18 mm and decreased at higher HABs subsequently.

Figure 3.8 is an HRTEM image of a particle located at HAB=14 mm. The HRTEM image shows that these particles have cubic structures which are normally associated with NaCl particles (Wang

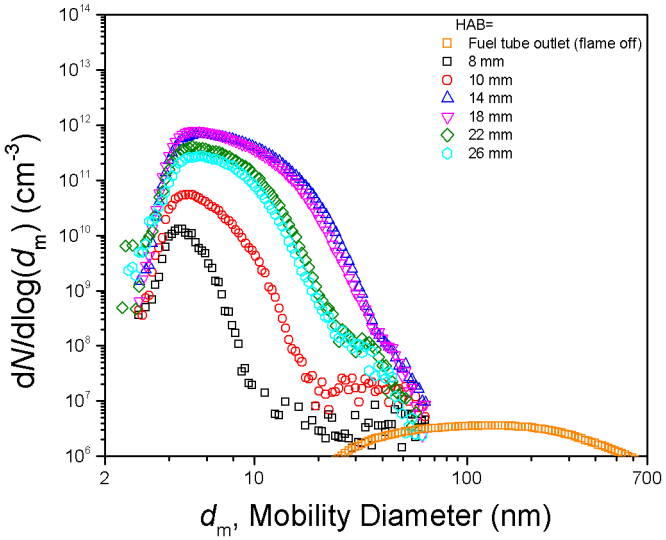

Figure 3.7: Particle size distributions at the burner tube outlet (HAB=0 mm) when the flame is off and along the centerline of the flame for HAB=8–26 mm in the case of methane-NaCl flame.

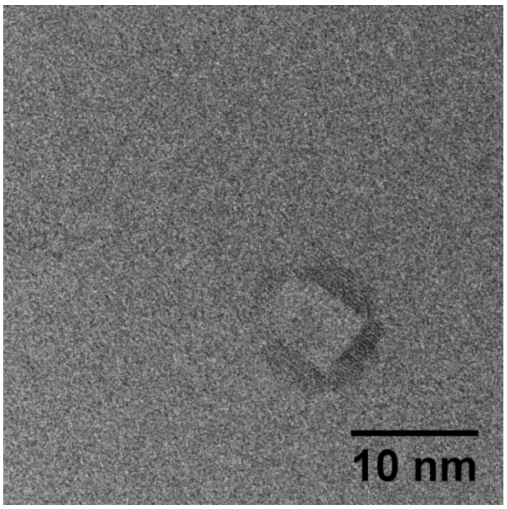

Figure 3.8: Cubic structure of a particle sampled at HAB=14 mm from methane-NaCl flame.

et al. 2010). Compared to the NaCl particles that were injected into the flame, NaCl particles observed from HABs above 8 mm were considerably smaller in size (median diameters of ~4–8 nm compared to ~130 nm) and larger in number concentration (approximately 600 to 77,000 times more). Therefore, these NaCl particles are believed to have been formed by nucleation of condensed NaCl vapour. The contour of temperature shown in Figure 3.2 indicates that the temperature of the flame at HABs below ~40 mm is less than the boiling point of bulk NaCl (*i.e.*, 1686 K); therefore, it is probable that evaporated NaCl condenses at HABs below 26 mm. The NaCl vapour that presumably condensed to form the nucleated NaCl particles may have diffused from the flame front where the temperature is above the boiling point of NaCl (see Figure 3.2). For nanoparticles smaller than a critical size, the surface-to-volume ratio is much larger than the bulk material and the melting point of nanoparticles decreases as their size becomes smaller (Wronski 1967; Zhang *et al.* 2000; Sun and Simon 2007). Therefore, it is expected that NaCl nanoparticles below a critical size have a melting point lower than that of bulk NaCl, which is known as melting point depression. This can be seen by comparing the melting point of bulk NaCl in Figure 3.2 (which occurs at HAB=10 mm) and the particle size distributions in Figure 3.7. The gas temperature along the centerline of the flame and below HAB=10 mm is less than the melting

point of bulk NaCl (*i.e.*, 1074 K); however, nucleated NaCl nanoparticles were first measured at HAB=8 mm, which could be an indication that the actual melting of NaCl nanoparticles occurs at that height with a lower temperature.

Figure 3.9 shows the size distributions from the methane-NaCl flame at HAB=30 to 60 mm. Figure 3.10 shows TEM images of particles at different representative HABs in the methane-NaCl flame. The inception mode in size distributions appears at HAB=30 mm similar to the size distributions of the methane-only flame. At HAB=30 to 34 mm, another mode was detected in the size

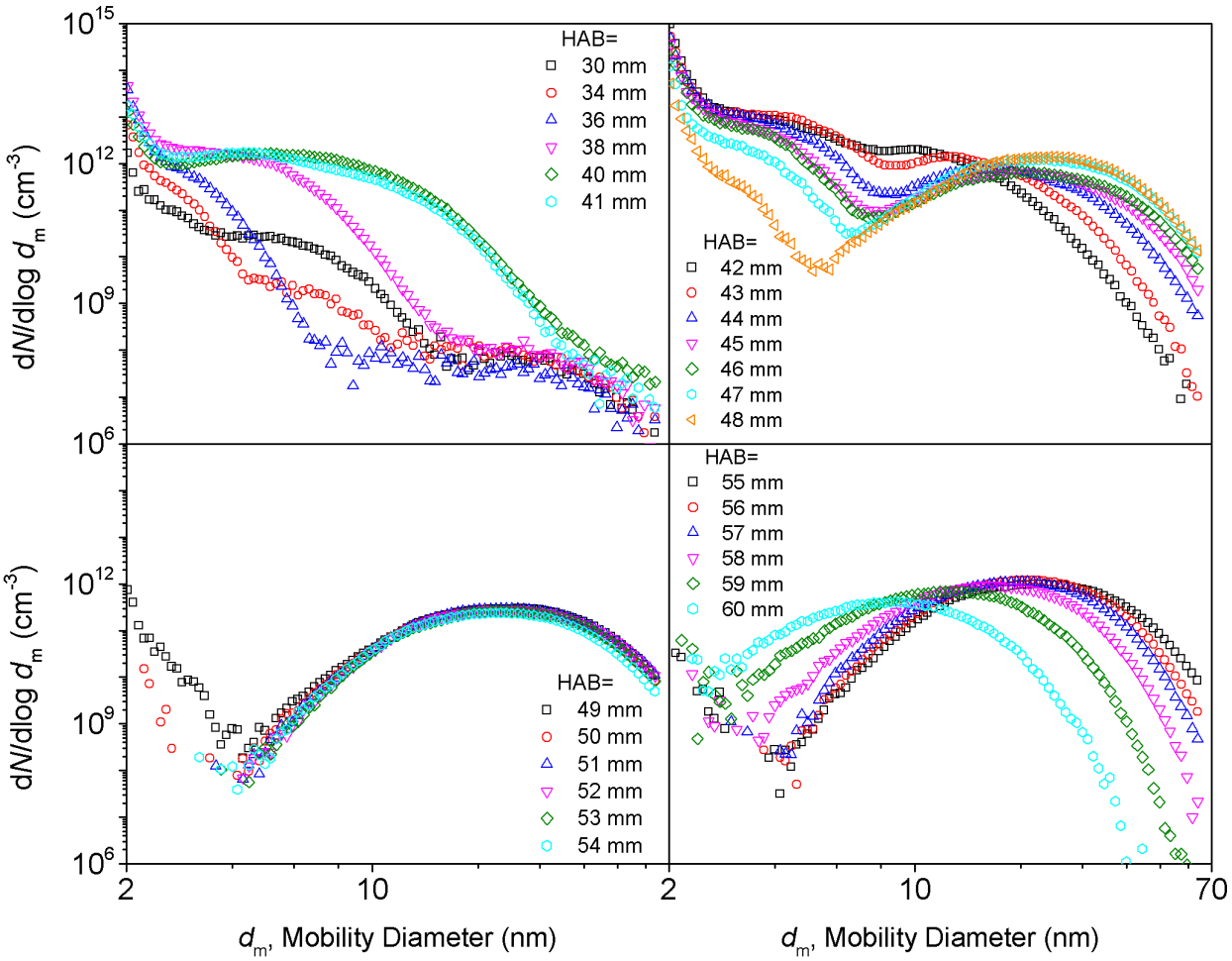

Figure 3.9: Particle size distributions for HAB=30–60 mm in the methane-NaCl flame. The top left panel covers the soot inception and surface growth region of the flame (HAB = 30–41 mm), the top right panel covers the coagulation region (HAB = 42–48 mm), the bottom left panel covers the agglomeration region (HAB = 49–54 mm), and the bottom right panel covers the oxidation region (HAB = 55–60 mm).

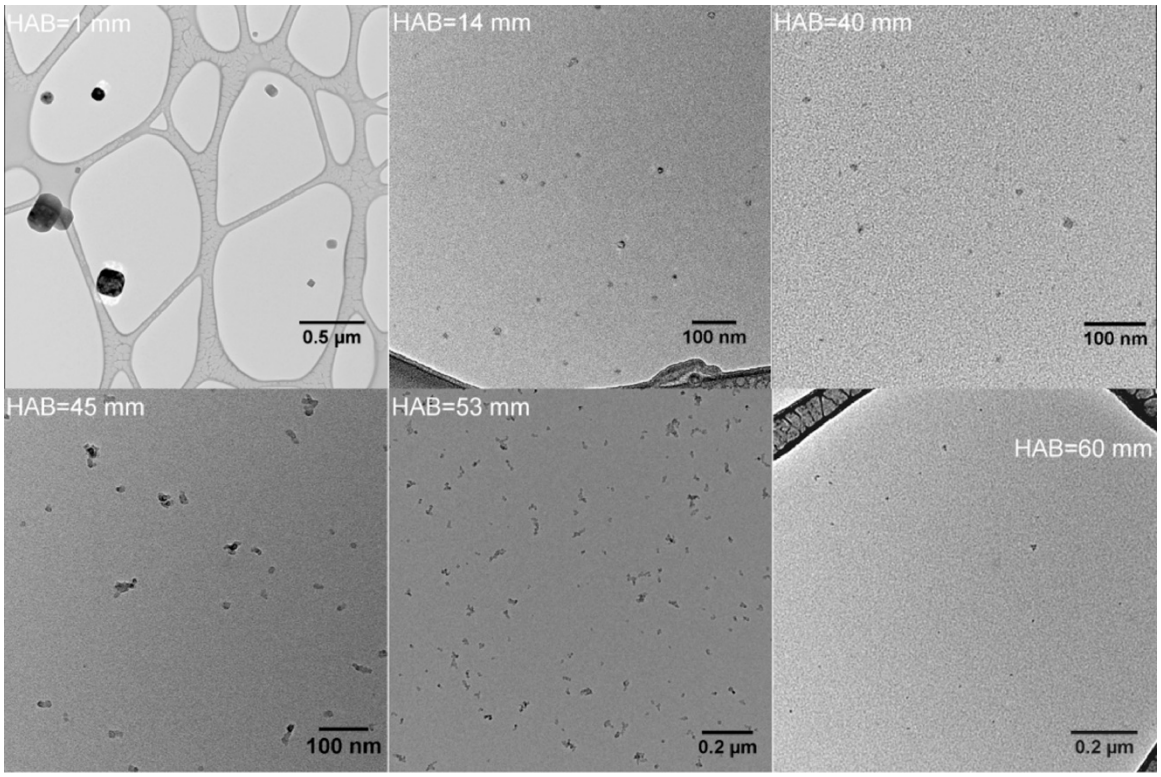

Figure 3.10: TEM images of particles sampled at different representative HABs in the methane-NaCl flame.

distributions with mobility diameters greater than 5 nm which could be attributed to the remnants of NaCl particles that were formed at lower heights. As the HAB increased, this mode in the size distributions decreased in number concentration and was not observed above HAB=36 mm. Boiling point depression is an important consideration for nanoparticles smaller than a critical size. Boiling point of nanoparticles decreases as their size becomes smaller (Nanda 2005), similar to their melting point. It is expected that the majority of small-sized nanoparticles nucleated at HAB=8 to 26 mm would evaporate prior to reaching the boiling point of bulk NaCl at HAB~42 mm (see Figure 3.2). This can be seen in the particle size distributions of the methane-NaCl flame (Figure 3.9) for HABs between 36 and 42 mm, where the gas temperature is less than the boiling point of bulk NaCl. As mentioned earlier, the remnants of NaCl nanoparticles were not seen in the

particle size distributions for HAB=36 mm and above, which could be an indication that NaCl nanoparticles evaporated above this height due to their reduced boiling point.

The size distributions from HAB=38 to 60 mm (Figure 3.9) are qualitatively similar to the size distributions for the methane-only flame, with Mode I appearing at HAB=38 mm and Mode II emerging at HAB=42 mm. For HAB=47 to 55 mm, size distributions were mostly dominated by coagulation from Mode II. For HAB=56 to 60 mm oxidation took place and a reduction in both the number concentration and the size of particles was observed. Although the emergence and disappearance of the three modes of the size distributions are generally similar between methane-only and methane-NaCl flames, the median diameters and number concentrations of nanoparticles are different.

As mentioned earlier, at HAB=46 mm the soot particles are expected to experience three simultaneous processes in soot formation and evolution, namely inception, surface growth, and coagulation. For heights between 46 to 53 mm, coagulation was the dominant process of soot evolution which means that the particles grew in size while their number concentration decreased. It appears that the rate at which the particles grew in size with increasing the HAB was quite different for the two flame cases. Figure 3.11 illustrate the changes in median diameter and total number concentration of particles (of the measured range) for both flame cases. In the methane-NaCl flame, the median diameter of the particles from HAB=47 to 53 mm were approximately constant with a size of ~23 nm. In the methane-only flame, the median diameter of the particles increased until it reached a maximum of ~35 nm at HAB=52 mm. These results show that there is a noticeable difference between the median diameter of the particles in the coagulation dominant region of each flame case; however, in the oxidation region (HABs above 53 mm) the particle median diameter in each flame case started to converge at heights near the tip of the flame. The

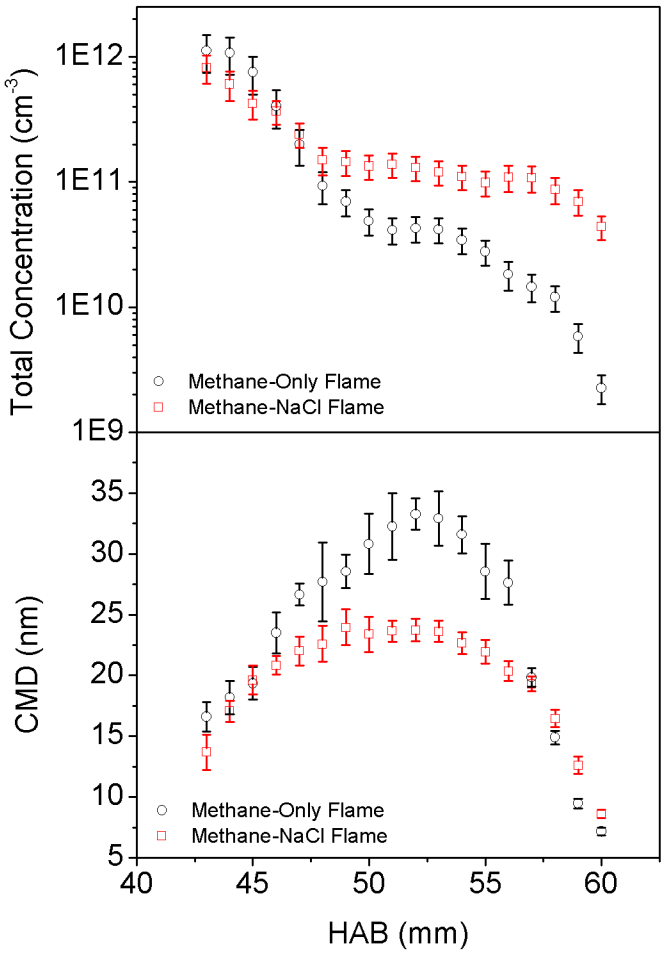

Figure 3.11: Variation of count median diameter (CMD) and total concentration of nanoparticles as a function of HAB, from 43 to 60 mm, for methane-only and methane-NaCl flames. The error bars represent the precision uncertainty based on at least five repeat measurements.

total number concentration of particles in both flame cases was quite similar for HABs below 46 mm; however, it started to diverge at HAB=47 mm with higher concentration of particles in the methane-NaCl flame. At HAB=60 mm, the concentration of particles was an order of magnitude higher in the methane-NaCl flame compared to the methane-only flame. Thus, the addition of NaCl particles to the flame leads to smaller particles with greater number concentration in regions of the flame where coagulation is dominant.

It was argued by Howard and Kausch (1980) that due to the low ionization potential of alkali metals, these metals could ionize readily in flames and affect the formation of soot particles in

both molecular and particulate scales. Based on this ionic mechanism of alkali metals, there are two hypotheses in the literature regarding the potential effect of alkali metals on soot formation.

The first hypothesis suggested by Bulewicz *et al*. (Bulewicz *et al.* 1975) states that alkali metals have the ability to affect the nucleation of soot particles by electrically neutralizing soot precursors and reduce soot formation. This hypothesis says that although the overall ion concentration (from metal and hydrocarbon) increases in a seeded flame, the actual concentration of natural flame ions decreases (Bulewicz *et al.* 1975; Howard and Kausch 1980). Bulewicz *et al*. (1975) investigated the effect of alkali metals on a propane/oxygen diffusion flame and found that the addition of some alkali metals such as potassium or cesium could increase the suppression of soot particles, leading to a smaller number of particles. In a more recent study, Simonsson *et al*. (2017) observed that the addition of potassium to a premixed flame reduced the size of primary soot particles and decreased the soot volume fraction due to low ionization potential of potassium.

The second hypothesis, proposed by Haynes *et al*. (1979), states that the ionic interaction between alkali metals and soot particles occurs after the inception (nucleation) of soot particles only. Calculations of Haynes *et al*. (1979) for various premixed flame conditions showed that the increase in the electrostatic repulsion forces between soot particles results in an order-of-magnitude reduction in the coagulation constant which leads to an increase in the number of soot particles and a decrease in the agglomerate size. In our study, we did not notice any significant difference between concentrations of the incipient soot particles (in the inception region) under the two flame conditions which could confirm that the addition of NaCl has a post-inception effect on soot particles, which is in agreement with the second hypothesis.

Based on the second hypothesis, alkali metals could reduce the coagulation rate between soot particles by altering the charge of soot particles. Some studies (Howard *et al.* 1973; Wersborg *et al.* 1975; Mitchell and Miller 1989) suggested that a majority of soot particles have positive charges, presumably due to thermionic emission. Mitchell and Miller (1989) reported that the addition of alkali metals reduces the number concentration of soot particles that are positively charged and suggested that alkali metals have the ability to neutralize charges of soot particles through the following reaction:

$$M + \text{soot}^{+} \rightleftarrows M^{+} + \text{soot} \tag{3.1}$$

Neutral soot particles have a lower tendency to coagulate compared to populations that include both charged and neutral soot particles (Glarborg 2007). Howard *et al*. (Howard *et al.* 1973) investigated the coagulation of soot particles in a flat premixed acetylene flame by accounting for both van der Waals and electrostatic forces and found that the coagulation rate constant between charged and uncharged particles could increase up to 2 to 3 times due to the aforementioned forces.

The results of the current study confirmed that the addition of NaCl particles to the methane diffusion flame reduced the agglomeration of soot particles, as the median size of the particles in regions of the flame where aggregation took place was smaller compared to the baseline methane flame while the number concentration of particles was higher in the former case, which is in agreement with the second hypothesis outlined above. Therefore, the reduction of particle coagulation could be attributed to the effect of alkali metal (in this case, sodium from NaCl) on soot particles.

3.3 Conclusions

In this study, the effects of the addition of NaCl particles to the flow on the observed nanoparticles along the centerline of a laminar diffusion flame was investigated. The spatial temperature field of the baseline methane flame and the methane flame doped with NaCl particles were obtained using rapid insertion of thermocouple, which showed that the NaCl particles added to the flame did not have a significant effect on the flame temperature. Additionally, it was found that the sampling probe affected the temperature in the flow approximately 3 mm upstream of the probe, which would have slowed any reactions in that region. Thus, the results showed in this chapter represent the processes happening in an unperturbed flame at a height which is 3 mm below the location of the sampling probe. A dilution system with a dynamic range of dilution ratio diluted the extracted sample from the flame immediately on the order of thousands of times to keep the integrity of the sampled particles before size distribution measurements.

Particle size distributions for the baseline case of methane flame showed different stages of nanoparticle evolution, from inception (with median size of ~3 nm) and surface growth (with a median size of ~10 nm) to coagulation (with a median size of ~33 nm) and oxidation (with a median size of ~7 nm). Transmission electron microscopy images showed that primary soot particles had core-shell structures. These images also showed that at higher HABs nanoparticles coagulated and formed soot aggregates; however, at HABs closer to the tip of the flame, these aggregates underwent significant change in their structure due to oxidation. Particle size distributions for the case of methane flame doped with NaCl particles showed that considerable concentrations of nanoparticles emerged at lower HABs where soot inception is typically not expected in a methane flame. Results showed that nanoparticles with a median size of 4 nm nucleated at the height of 8 mm and grew to their maximum concentration and median size of 8 nm at HAB=18 mm. The TEM images showed that the structure of these nanoparticles was not

similar to soot particles; rather they resembled typical NaCl particle structure. These nanoparticles became smaller in size and concentration up to the heights where soot nanoparticles started to incept. For higher HABs the particle size distribution followed a similar trend as the baseline case of methane flame, except for regions of the flame where coagulation is the dominant process. In this region, the addition of NaCl reduced the mobility diameter of aggregate soot particles but at the same time increased their number concentration. These results indicate that the addition of NaCl to the flame reduced the coagulation between soot primary particles due to the effects of sodium (as an alkali metal) in the NaCl. The existence of sodium in the flame presumably neutralizes charged soot particles, which subsequently reduces the coagulation between soot particles.

CHAPTER 4

Effect of sodium chloride on the evolution of size, mixing state, and light absorption of soot particles from a sooting laminar diffusion flame[4]

4.1 Introduction

In Chapter 3, we looked at the evolution of the size and morphology of the nanoparticles inside a closed-tip (non-smoking) laminar diffusion flame of methane when NaCl particles were added to the fuel. However, as the flame tip was closed, the majority of soot particles oxidized at the flame tip and were not released to the post-flame region. In this chapter, the objective is to continue our work in the Chapter 3 and to study the effect of NaCl on the evolution of size and mixing state of soot particles from an open-tip (smoking) laminar diffusion flame. The release of soot particles to the post-flame region provides an opportunity for re-condensed NaCl particles at lower

[4] This chapter is based on the following conference paper:
- Kazemimanesh, M., Kuang, C., Kostiuk, L.W., and Olfert, J.S. (2019). Effect of sodium chloride on the evolution of size and mixing state of soot particles from a sooting laminar diffusion flame. *In Proceedings of the Combustion Institute Canadian Section*, May 13–16, Kelowna, BC, Canada.

temperatures to mix with soot particles. The results of this study provide an understanding about the final state of particle emissions, how that state was arrived at, and the light absorption properties of the particle emissions. These results can be useful in understanding the interaction that lead to the microphysical and optical properties of particle emissions in practical scenarios such as from gas flares subsequent to flowback operations in the upstream oil and gas industry.

4.2 Experimental Setup

The experimental setup used for the experiments in this chapter, including the sampling and dilution system, the NaCl particle generation system, and the particle measurement suite, was essentially identical to the one described in details in Chapter 2. Here, we only discuss the minor modifications and additional measurement systems of the experimental setup.

4.2.1 Co-flow Burner

Santoro *et al*. (1983) used ethylene as the fuel to produce a sooting flame due to the higher sooting propensity of ethylene. However, we desired to use methane as the fuel because it is commonly a major component of flared gases. It was not possible to produce a laminar sooting flame with methane by simply changing the flow rates of fuel and air, as did Santoro *et al*. (1983) with ethylene. Thus, a minor modification, inspired by the works of Ishizuka and Sakai (1988) and Ishizuka (1982), was made to the co-flow burner to produce an open-tip sooting diffusion flame with methane. A 51 mm long quartz tube with internal and external diameters of 30 and 33 mm, respectively, was placed concentrically around the fuel tube to produce a sooting laminar diffusion flame with a visible height of ~100 mm. The fuel tube protruded 4 mm above the ceramic honeycomb of the burner and the outlet of the small quartz tube was 47 mm above the fuel tube; thus, the lowest height above the burner (HAB) that could be sampled with the sampling probe was 47 mm. The fuel and the overall co-flow air flow rates were 0.261 and 27.5 SLPM (standard

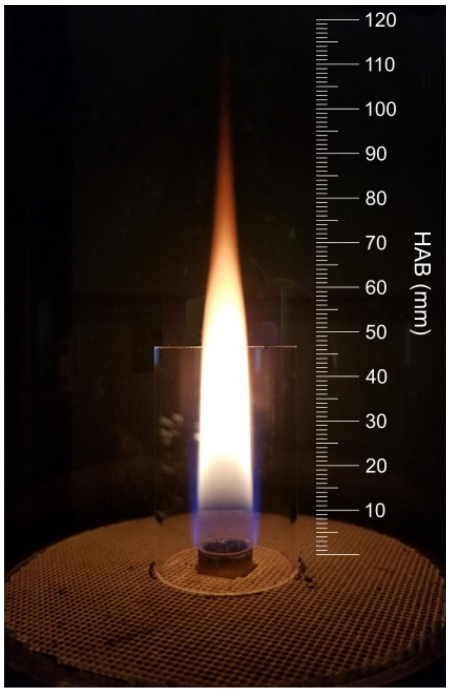

Figure 4.1: Image of the open-tip sooting laminar diffusion flame. The quartz tube around the fuel tube had a diameter of 30 mm.

liters per minute at 1 atm and 25 °C), respectively. Part of the co-flow air enclosed by the small quartz tube was used for combustion and the remainder diluted the exhaust products. Figure 4.1 shows the image of the sooting open-tip laminar diffusion flame used. One objective of the experiments in this chapter is to investigate whether soot and NaCl particles are externally mixed, *i.e.* exist as individual particles separate from each other, or internally mixed, *i.e.* NaCl particles are part of or attached to soot aggregates (see Section 1.4 for background on these two mixing states). To study the evolution of mixing state of soot and NaCl particles in the post-flame region, the large quartz shield (discussed in Section 2.2.1) had to be extended to 600 mm in length in order to provide sufficient time and reduction in temperature for the particle emissions to reach their final mixing state.

4.2.2 Absorption and Scattering Coefficient Measurements

To measure the absorption and scattering coefficients of the particle emissions, a photoacoustic extinctiometer (PAX; Droplet Measurement Technology Inc.) was used. The measurement cell of the PAX consisted of a reciprocal nephelometer, which measured the scattering coefficient, and a photoacoustic cell, which measured the absorption coefficient. The PAX used a modulated diode laser to simultaneously measure light scattering and absorption of the particle emissions. The laser had a standard infrared wavelength of 870 nm, which is highly specific to black carbon (BC) particles, since there is relatively little absorption from gases and non-BC aerosol particles at this wavelength. The absorption measurement used *in-situ* photoacoustic spectroscopy (Petzold and Niessner 1996; Arnott *et al.* 1999). A laser beam directed through the aerosol stream was modulated at the resonant frequency of the acoustic chamber (nominal frequency of 1,500 Hz). Absorbing BC particles heat up and quickly transfer heat to the surrounding air when thermally relaxed. The periodic heating and thermal relaxation of the absorbing particles produced acoustic (pressure) waves with a frequency that matched the frequency of the modulated laser. The amplitude of these acoustic waves was amplified in a resonator with a quality factor of ~26 and subsequently detected with a sensitive microphone mounted on the acoustic chamber.

The PAX used a wide-angle integrating reciprocal nephelometer to measure the scattering coefficient. The scattering measurement responds to all particle types (BC and non-BC) regardless of chemical composition, mixing state, or morphology. The nephelometer consisted of a tube aligned concentric with the previously mentioned laser beam and the aerosol sample was passed through this tube via two ports on each end of the tube. The inner surface of the tube was coated with black paint and two identical baffles with small apertures were mounted on both sides of the tube to minimize the reflection of scattered light by the inner wall of the tube. A photomultiplier

tube (PMT) was mounted on the tube, perpendicular to the direction of the laser beam, which could detect the scattered light (Abu-Rahmah *et al.* 2006).

As the absorption coefficient, B_{abs}, was high in these measurements, a more accurate method was used as follows instead of photoacoustic spectroscopy. The extinction coefficient, B_{ext}, was directly measured by PAX with a photodiode detector based on Beer-Lambert law of light intensity attenuation:

$$B_{ext} = -\frac{1}{L}\ln\frac{I}{I_0} \tag{4.1}$$

where L was the path length of the laser beam through the cavity (0.354 m), I was the light intensity during measurement detected by the photodiode, and I_0 was the average light intensity before and after the measurement (with particle-free air sample). The scattering coefficient, B_{scat}, of the sample was measured using the nephelometer integrated into the PAX. Thus, the absorption coefficient was obtained as the difference between extinction and scattering coefficients, *i.e.*, $B_{abs} = B_{ext} - B_{scat}$. It should be noted that the same procedure is used to calibrate the absorption coefficient measured by the photoacoustic technique and, thus, the outlined method was more accurate if the absorption of the sample is very high (as was the case in these experiments). The scattering was calibrated using strongly scattering particles (such as ammonium sulfate) by comparing the scattering coefficient measured by the nephelometer with the extinction coefficient calculated from laser intensity attenuation based on Beer-Lambert law for many data points in the calibration range (up to 20,000 Mm^{-1}). Because the absorption of ammonium sulfate particles was negligible, the extinction by these particles was almost due to their scattering. The sample was drawn into the PAX at a flow rate of 1 L/min using its built-in vacuum pump. Typical sampling time was 120 s after the absorption and scattering coefficients were steady.

4.2.3 Elemental Carbon Mass Concentration Measurement

As mentioned in Section 1.4, light absorption depends on aerosol concentration and, thus, it is common to normalize that by the particle mass concentration. This normalized absorption coefficient is known as mass-specific absorption coefficient (MAC; or mass absorption cross-section). Therefore, to calculate the MAC of the particle emissions sampled in Section 4.2.2, the mass concentration of the elemental carbon (EC) in the particle emissions must be measured. Soot particles are generally composed of elemental carbon, organic carbon (OC), hydrogen, and oxygen, with elemental carbon being the main light absorbing component and often linked to black carbon. The mass concentration of EC was measured by collecting soot particles on 47 mm pre-fired quartz fiber filters (Pall Inc., Model Tissuquartz 2500 QAO-UP) in parallel to absorption and scattering measurements. The filters were pre-fired in a muffle furnace at 750 °C for 4 hours to assure that all carbon was removed. The filters were held in a dual-stage filter holder (URG Corp., Model 2000-30FXT) and the soot sample was drawn through the 6.3-mm sampling tube used in Section 4.2.2 and the filter holder at 5 L/min using a flow controller (Alicat Scientific, Model MCR-50SLPM-D) connected to the lab vacuum line. Total sample volume was calculated by acquiring the flow rate data from the flow controller over the sample collection time (typically, 3–5 min). The samples were analyzed by thermal-optical analysis (TOA) following the NIOSH 5040 protocol using a Sunset Lab EC–OC analyzer (Birch and Cary 1996).

4.3 Results and Discussion

4.3.1 Nanoparticles Observed in the Methane-only Flame

Figure 4.2 shows the particle size distribution for the case of the methane-only flame spanning a range of heights above the burner (HAB) from 47 to 437 mm. As mentioned in Section 4.2.1, the lowest HAB that could be probed was 47 mm due to the small quartz tube. The measured particle

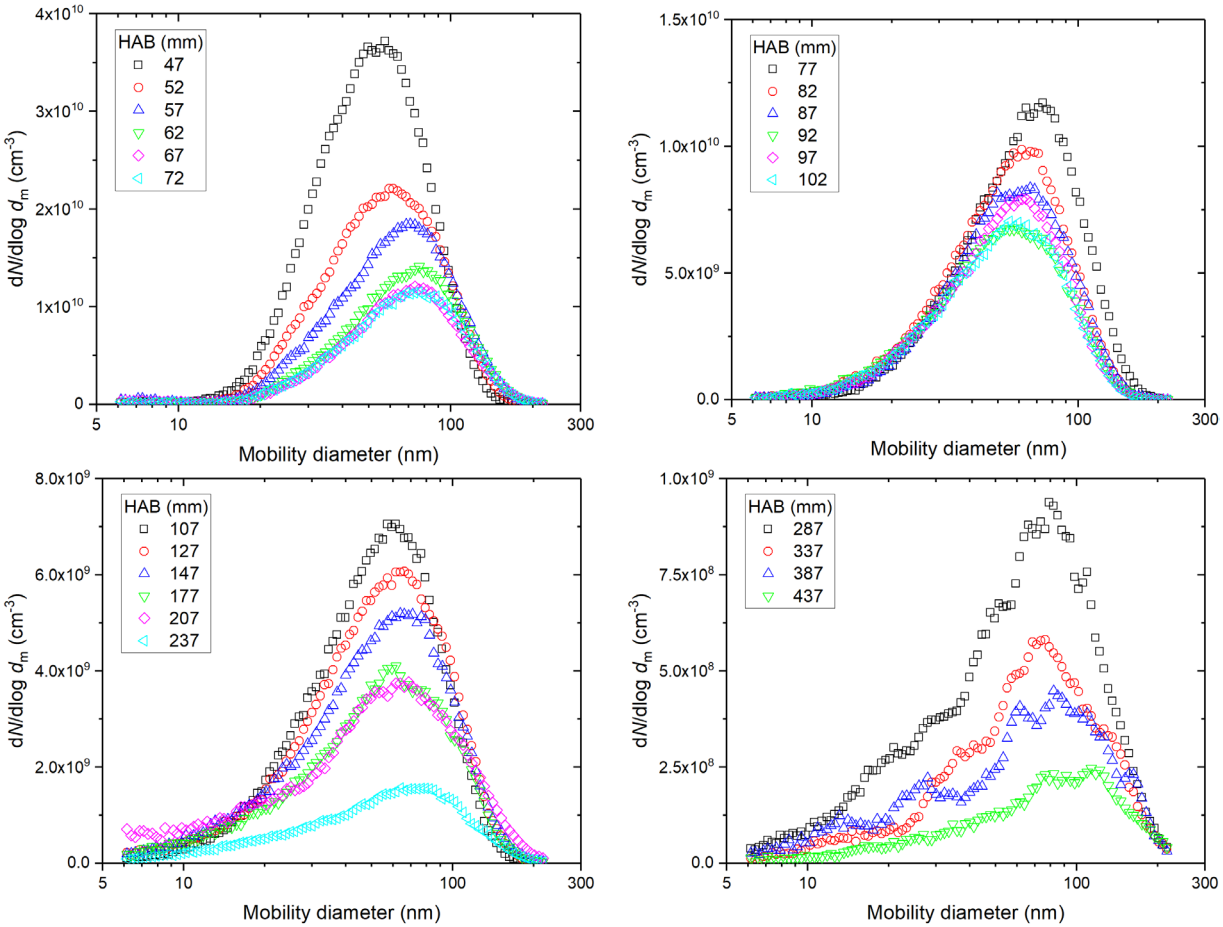

Figure 4.2: Particle size distributions for the case of methane-only sooting flame spanning HAB range of 47 to 437 mm.

size distributions generally had a negative skew and the mode diameter of the size distribution is reported instead of its median diameter. Moreover, since the size distributions were measured partially at some HABs, the total particle concentration is reported based on the integral of lognormal fits to the measured data. Figure 4.3 shows the total particle concentration and the particle mode diameter as a function of HAB. The particle mode diameter increased from 56 nm to 77 nm as the HAB increased in the range of 47–72 mm (Figure 4.2, top left panel), while the total concentration of particles decreased continuously in the same height range. This was due to the coagulation and agglomeration of soot particles inside the diffusion flame, consistent with our previous findings in Chapter 3. As the HAB increased from 72 to 102 mm, the particle mode

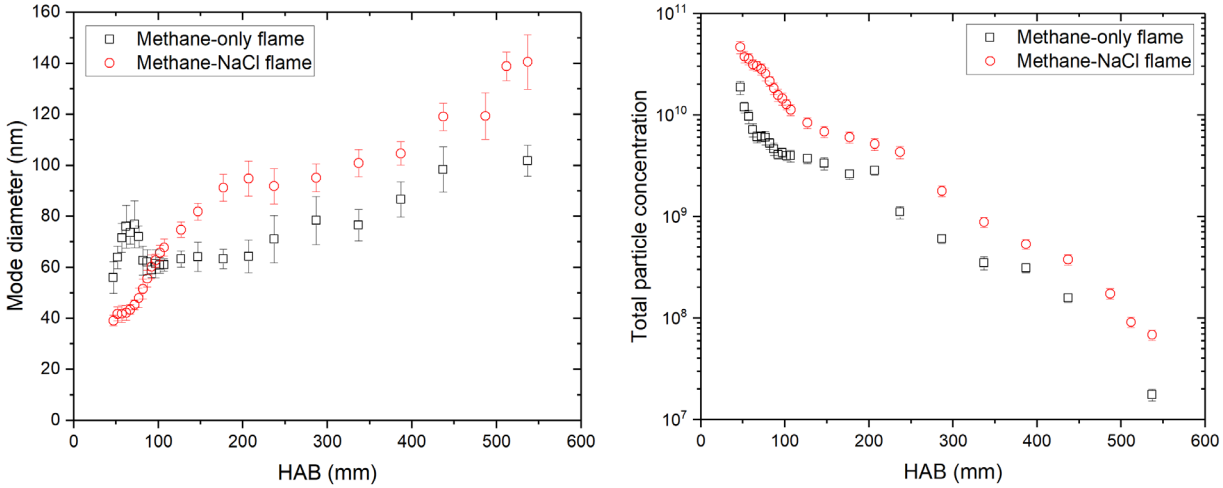

Figure 4.3: Mode diameter and total concentration of soot as a function of HAB for sooting methane-only and methane-NaCl flames. When multiple modes are seen in the size distribution of particles from the methane-NaCl flame (*i.e.*, at HAB=287 mm and higher), only the mode diameter and concentration of soot particles are reported in this figure.

diameter decreased from 77 nm to ~60 nm, while the total particle concentration decreased gradually (Figure 4.2, top right panel). Presumably, the reduction in particle size was due to partial oxidation of soot particles near the open tip of the flame and the reduction in particle concentration was a result of ongoing coagulation. This is also consistent with the change in particle size and concentration observed in the oxidation region near the closed tip of the diffusion flame in Chapter 3.

The particle mode diameter remained relatively constant at ~63 nm as the HAB increased in the range of 102–207 mm, while particle concentration decreased continuously (Figure 4.2, bottom left panel). This was a region just above the open tip of the flame and the soot particles were likely mixing gradually with part of the co-flow air not consumed for combustion and, thus, their concentration decreased slowly. In the height range of 207–437 mm, the particle mode diameter increased from 64 nm to ~100 nm as the HAB increased, while the particle concentration decreased (Figure 4.2, bottom right panel). Particle coagulation was the main process in this post-flame region, causing the particles to grow larger in size and their concentration to decrease. The

reduction in particle concentration was also partly due to mixing with more co-flow air. Although the particle size distributions in this panel are scattered due to low concentrations measurement by the SMPS.

4.3.2 Nanoparticles Observed in the Methane-NaCl Flame

Figure 4.4 shows the particle size distribution for the case of the methane-NaCl flame for HAB range of 47–537 mm. As the HAB increased from 47 to 72 mm, the particle mode diameter increased from 39 nm to 45 nm, while particle concentration decreased gradually (Figure 4.4, top left panel). Similar to the closed-tip methane-NaCl flame in Chapter 3, this HAB range was the agglomeration region inside the flame and the particles underwent coagulation in this region.

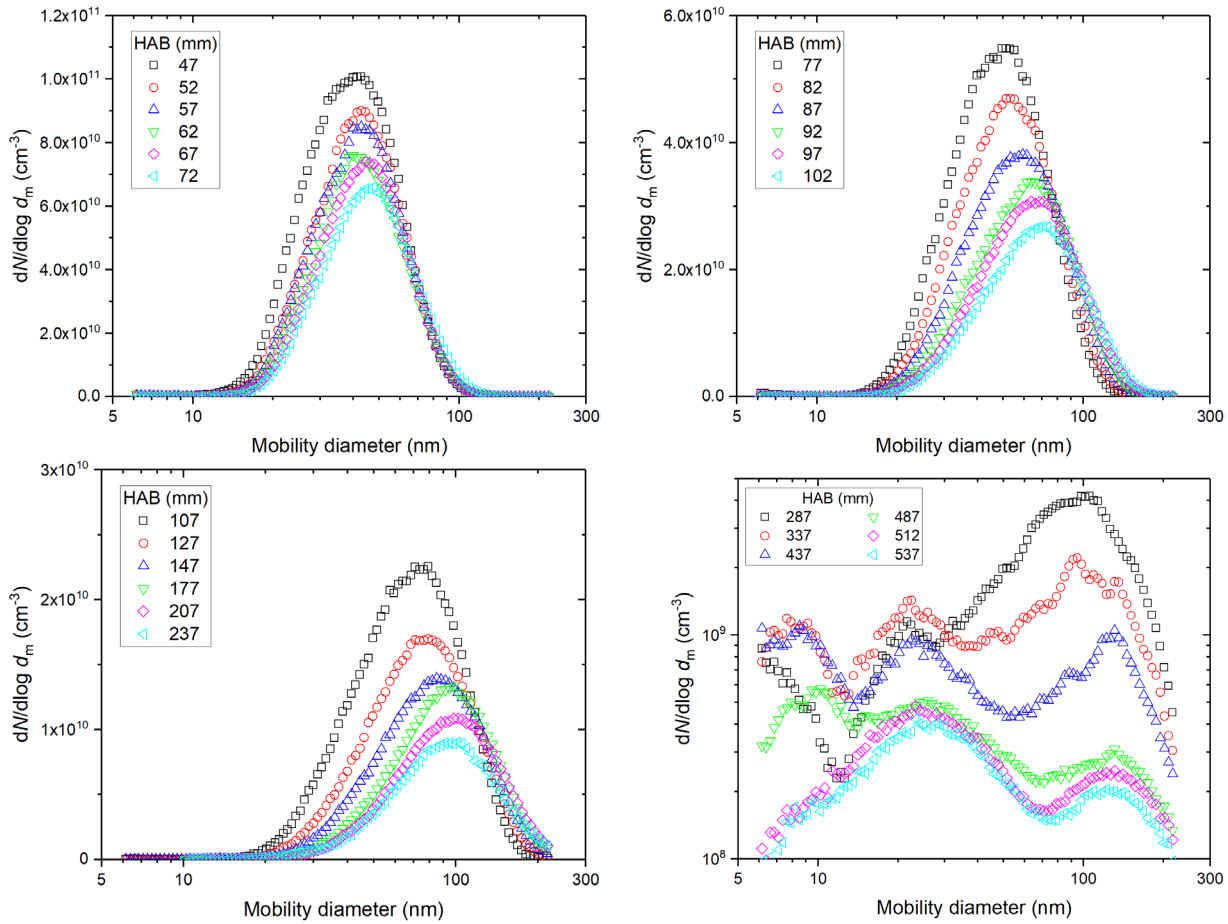

Figure 4.4: Particle size distributions for the case of methane-NaCl sooting flame spanning HAB range of 47 to 537 mm.

However, particle mode diameter was smaller in this region compared to the case of methane-only flame, *i.e.*, a change from 39 nm to 45 nm in the methane-NaCl flame compared to a change from 56 nm to 77 nm in the methane-only flame (see Figure 4.3). Also, the particle concentration was higher by several factors for the methane-NaCl flame compared to the methane-only flame and in the same HAB range of 47–72 mm. The reacting flow temperature in this region of the flame is higher than the boiling point of the introduced NaCl particles and, thus, the NaCl exists in vapour phase. The smaller soot particle size and its higher concentration in the methane-NaCl flame shows that the existence of NaCl vapour in the coagulation region of the flame reduced the rate of coagulation between soot particles. This result is consistent with the same observation in the closed-tip methane-NaCl flame (Chapter 3, Section 3.2.3), where the coagulation rate between soot particles was reduced in the presence of NaCl vapour.

In agreement with these results, several other studies with in-flame measurements have reported that the addition of alkali metals (such as Na, K, Cs) to a diffusion flame decreases soot particle size (Bonczyk 1983, 1988; Tappe *et al.* 1993), while in one flame a significant increase in soot particle concentration was observed (Bonczyk 1983) and in the other flames the soot particle concentration slightly increased with a decrease in the soot volume fraction (Bonczyk 1988; Tappe *et al.* 1993). A decrease in soot particle size and an increase in soot particle concentration inside the flame have been also reported for various premixed flames when alkali metals were added to the flame (Haynes *et al.* 1979; Hayhurst and Jones 1989; Wieschnowsky *et al.* 1989; Bonczyk 1991). Similar to the discussion in Section 3.2.3, some studies (Feugier 1978; Haynes *et al.* 1979; *e.g.*, Wieschnowsky *et al.* 1989) suggest that the observations here can be due to enhanced charging of incipient soot particles, which causes the charged soot particles to resist further collisional growth and coagulation. However, a more plausible explanation is the reduction in the

number of positively-charged soot particles due to exchange of electron with alkali metal atoms and turning soot particles electrically neutral (Mitchell and Miller 1989). Howard *et al*. (Howard *et al.* 1973) have shown that by considering the effect of electrostatic and van der Waals forces, the coagulation rate between a neutral and a charged particle is theoretically 2–3 times (and experimentally 10 times) higher than that between two neutral particles and the coagulation rate between two similarly charged particles is much smaller than the other two cases. Thus, a population of neutral soot particles has less tendency to coagulate with each other compared to a population of neutral and charged soot particles. It should be noted that the concentration of NaCl molecules was on the order of ~5×10^{14} molecule/cm^3 (based on the NaCl mass concentration of ~45 ng/cm^3), which was much higher than the concentration of incipient soot particles in the flame and, therefore, it was assumed that all charged soot particles became neutral very rapidly via charge exchange.

In the HAB range of 72–102 mm, which is near the open tip region of the flame, one would expect oxidation of soot particles to happen and the particle size to decrease similar to the methane-only flame. However, on the contrary, the particle mode diameter grew from 45 nm to 66 nm (Figure 4.4, top right panel) and, at the same time, the concentration decreased gradually. This observation was presumably due to the inhibition of soot oxidation in the presence of NaCl. While the oxidation of soot was inhibited, the soot particles continued to coagulate in this HAB range, which further explains the growth in soot particle size and the decrease in particle concentration.

Previous studies have pointed out that the oxidation of soot in atmospheric fuel-rich and fuel-lean flames is predominantly linked to surface attack by hydroxyl radicals (·OH) and to a lesser degree to O_2, among the possible oxidant species such as H_2O, CO_2, NO, O_2, O, and OH (Fenimore and Jones 1967; Neoh *et al.* 1981; Bradley *et al.* 1985; Garo *et al.* 1990; Roth *et al.* 1991; Puri *et al.*

1994). Also, the inhibition of OH radicals in the flames by the addition of alkali metals has been reported before. For example, kinetics of flame inhibition by potassium (Jensen *et al.* 1979) and sodium (Jensen and Jones 1982) have been studied using a two-reaction mechanism to explain the accelerated removal of OH radicals. Also, Slack *et al*. (1989) have reported that by the addition of potassium (and similarly sodium) to a methane premixed flame, the number concentration of OH radicals at all HABs inside the flame decayed In addition to the proposed mechanisms outlined above, direct evidence of the inhibition of hydroxyl radicals has been also reported by laser-induced fluorescence (LIF) measurements when alkaline-earth metals (such as barium and calcium) were added to a sooting ethylene diffusion flame (Bonczyk 1988). In summary, the addition of sodium to the flame causes a decay in the concentration of OH radicals, which in turn leads to less soot oxidation by these radicals in the oxidation region of the flame. Between the two competitive processes of oxidation and an ongoing coagulation in this region, the coagulation is dominant and causes the soot particles to grow larger in size and in lower concentrations. It should be noted that some previous studies have mentioned that by addition of alkali metals to the flame, the soot particles become smaller due to less coagulation and, thus, these smaller soot particles are oxidized more easily (*e.g.*, Mitchell and Miller 1989). This statement is not necessarily always true because in open-tip sooting flames, such as the one studied here, the alkali metals can have an inhibitive effect on the oxidative attacks of OH radicals and let the soot particles survive to the post-flame regions. Therefore, the alkali metals can serve different roles based on the ongoing processes in the flame (*i.e.*, reduction of coagulation and inhibition of oxidation).

In the HAB range of 107 mm to 237 mm, the particle coagulation continued due to sufficient time and mixing with co-flow air (Figure 4.4, bottom left panel). The soot particles grew in diameter from 68 nm to 92 nm, while their concentration decreased gradually. Particles in this HAB range

were generally larger in diameter than their counterparts in the methane-only flame (Figure 4.3) due to the continued coagulation of soot particles in the methane-NaCl flame without the size-shrinking effect of oxidation seen in the methane-only flame. Moreover, the particle concentration in the methane-NaCl flame was a factor of ~3 more than that of the methane-only flame, which was due to inhibited oxidation of soot in lower HABs in the methane-NaCl flame. This is an interesting observation because this height range (107–237 mm) was in the post-flame region and the soot was both larger in size and higher in concentration in the case of the methane-NaCl flame, which means that the mass concentration of soot in this case was higher compared to the methane-only flame. To illustrate this, if we assume that the mass-mobility exponent of soot particles was ~2.5 (Olfert and Rogak 2019) and the soot particles were 64 nm and 92 nm at the HAB=237 mm in methane-only and methane-NaCl flames, respectively, and by considering a three-fold increase in soot concentration in the methane-NaCl flame, we can calculate the mass concentration ratio as $3\times(92\text{ nm}/64\text{ nm})^{2.5} = 7.4$, which means the mass concentration of soot increased by a factor of ~7 when NaCl was added to the flame.

This result is consistent with the findings of Jefferson (2017), where an increase of several times in soot mass concentration, measured by laser-induced incandescence (LII), was reported for a large turbulent diffusion flame of mostly methane and other C2–C4 alkanes when atomized droplets of NaCl solution were introduced into the flame. This result is also partly consistent with other studies (Cotton *et al.* 1971; Bulewicz *et al.* 1975), where alkali metal additives were shown to have either an increasing or decreasing effect on soot emission in the post-flame region of propane-oxygen and acetylene-oxygen diffusion flames, depending on the ion concentration of alkali metal. It should be noted that in these studies droplets of NaCl solution (containing water and NaCl) were introduced into the flame, whereas we introduced solid NaCl particles (with no

water content) into the flame. The added water content in the form of droplets presumably increase the concentration of hydroxyl (OH) radicals in the flame, which can further increase the oxidation of soot (Hirschler 1986). In light of the oxidation inhibiting effects of alkali ions, we may be able to explain the observed dependence of soot emission on alkali ion concentration in the two aforementioned studies (Cotton *et al.* 1971; Bulewicz *et al.* 1975) as follows: Between the two competing effects of increased soot oxidation due to added water and inhibition of soot oxidation due to added alkali ions, the outcome depends on the relative concentration of alkali ions. If the alkali ion has a high concentration, all the OH radicals are scavenged and the soot oxidation is inhibited, thus, the soot emission increases. However, if the alkali ion concentration is low, not all OH radicals are removed, which leads to increased soot oxidation and, therefore, the soot emission decreases. This is an interesting hypothesis which needs further exploration in future.

At HAB=287 mm, the particle size distribution became trimodal with three modes at < 6 nm, ~25 nm, and 95 nm (Figure 4.4, bottom right panel). Here the size distribution plot is in logarithmic scale to better represent the differences between subsequent size distributions. Presumably, the two leftmost modes were due to freshly nucleated NaCl particles based on electron microscopy images (as shown in Section 4.3.3), which re-condensed from NaCl vapour at lower temperatures observed at this height above the burner. The rightmost mode was due to soot particles as they continued to grow in size as a result of coagulation (as shown Section 4.3.3). The trimodal distribution existed up to HAB=487 mm with its first mode at ~8 nm and second mode at ~25 nm; however, the particle concentration in the third mode (soot mode) gradually decreased relative to the other two modes.

At HAB=512 mm and higher, the particle size distribution became bimodal with a leftmost mode at ~25 nm and a rightmost mode at ~140 nm. Apparently, the NaCl particles in the first mode of

the previous trimodal distributions (*i.e.*, the 8 nm particles) coagulated with each other and the NaCl particles in the second mode (*i.e.*, the 25 nm particles) to a final size of ~25 nm and increased the overall population of NaCl particles relative to soot particles. The sample temperature was ~110 °C at these HABs and the size distribution became independent of the HAB except for its number concentration which decreased gradually due to mixing with co-flow air.

4.3.3 Mixing State of Particles

The mixing state of particles was investigated using transmission electron microscopy (TEM). Figure 4.5 shows representative TEM images of samples collected from the methane-NaCl flame at HABs of 177 mm, 287 mm, and 537 mm. At a height of 177 mm (Figure 4.5a and b), the exhaust products of combustion were still at elevated temperatures (~540 °C) and NaCl existed in vapour phase. No NaCl particles were observed under the TEM and the soot particles had the fractal-like structure typical of soot from combustion sources. At HAB=287 mm, which was the onset of NaCl re-nucleation based on particle size distribution data, spherical or cubic NaCl particles were observed, mostly with a diameter of ~20 nm, which is consistent with particle size distribution data (Figure 4.5c and d). Most of these NaCl particles existed as individual particles and externally mixed with soot particles; however, they were occasionally attached to a soot aggregate and, thus, are considered to be internally mixed with soot particles. At HAB=537 mm, *i.e.*, 300 mm above the previous sampling point, the mixing state of NaCl and soot particles was very similar to the case of HAB=287 mm, with most of the NaCl particles observed individually (Figure 4.5e and f) and occasionally internally mixed with soot particles.

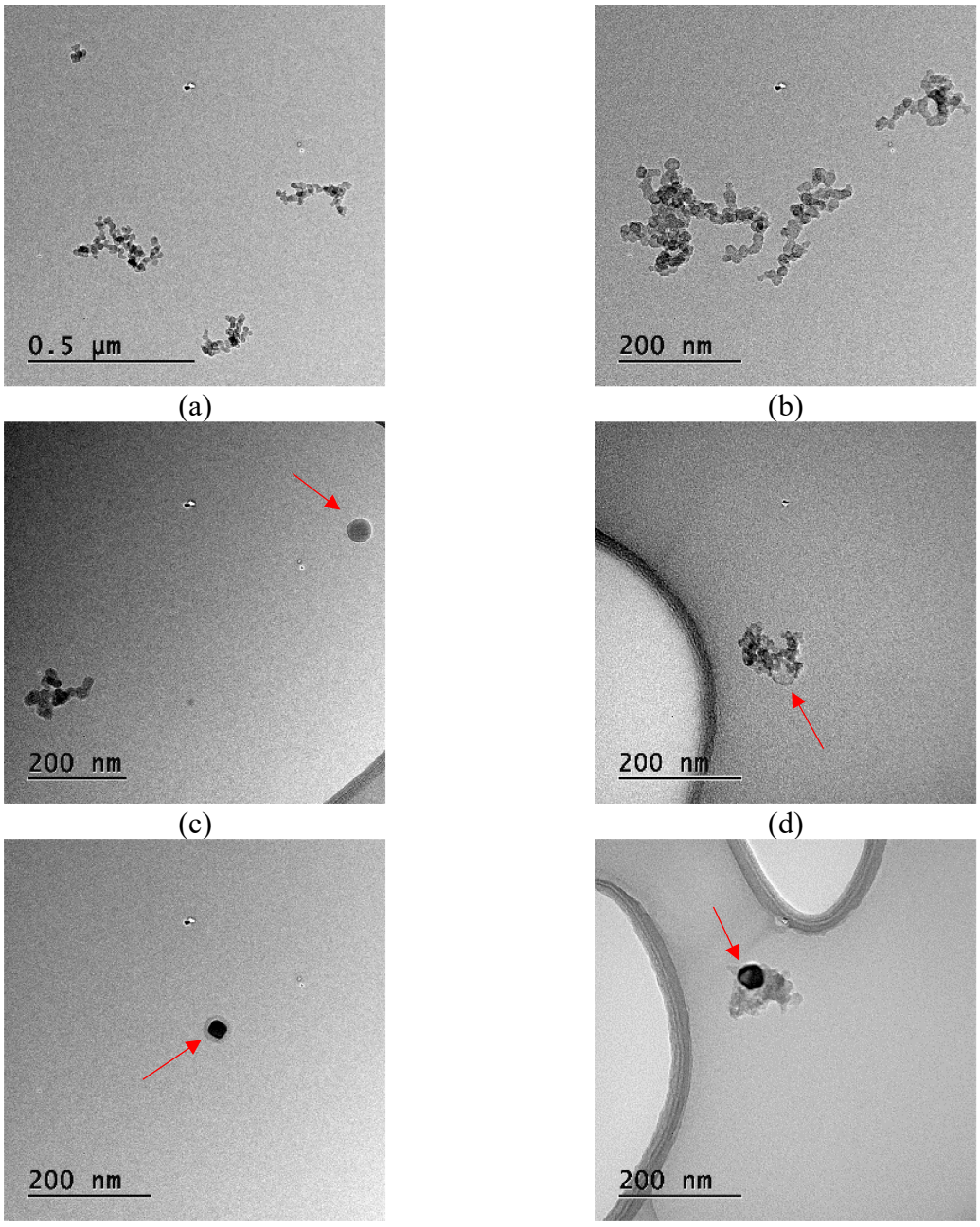

Figure 4.5: TEM images of particles at HAB=177 mm (a & b), 287 mm (c & d), and 537 mm (e & f). NaCl particles are pointed with a red arrow in these images.

These TEM images also indicate that in the bimodal particle size distributions of methane-NaCl flame (Figure 4.4, bottom-right panel), the mode with smaller particle size was due to NaCl particles with a diameter of ~20-25 nm and the mode with larger particle size was due to soot particles or NaCl particles internally mixed with soot particles. It should be noted that the

coagulation coefficient for two 25-nm NaCl particles is 11.9×10^{-10} cm^3/s, while for a 140-nm soot particle and a 25-nm NaCl particle the coagulation coefficient is 39.4×10^{-10} cm^3/s (Hinds 1999, p. 268). This means that more coagulation would be expected between soot and NaCl particles than between two NaCl particles or two soot particles of approximately the same size.

4.3.4 Light Absorption of Particle Emissions

The PAX was used to measure the absorption and scattering of particle emissions at the wavelength of 870 nm. The objective was to measure the optical properties of particle emissions from both methane-only and methane-NaCl flames at their final mixing state and, thus, the sample was drawn from HAB=537 mm. The particle emissions were sampled using a 6.3 mm stainless tube, with its sample inlet aligned along the centerline of the flame. The high-dilution sampling system was not required for these measurements as the particle concentration was relatively low and particle-particle coagulation was negligible. The PAX manufacturer has not provided data on the bias uncertainty of their instrument; thus, we considered the bias uncertainties in absorption and scattering coefficients as ±9.6% and ±7.0% based on the repeatability of three independent calibrations performed over two months. This is a more conservative uncertainty than the total uncertainty of ±4.4% (at 870 nm) recently reported by Conrad and Johnson (2019) for a similar three-wavelength photoacoustic spectrometer (PASS-3) from the same manufacturer. For each flame condition, three sets of samples were measured. The precision uncertainties in B_{abs} and B_{scat} was estimated based on the three measurement repeats. The total uncertainties in B_{abs} and B_{scat} was calculated by propagation of the respective bias and precision uncertainties (refer to Appendix D for details of the uncertainty analysis).

The soot sample was also collected simultaneously on filters to determine its mass concentration. Thermal-optical analysis of the soot samples determined the amount of EC and OC on the filter.

Here we were only interested in the mass concentration of EC, which is the main light absorbing component of soot and often linked to black carbon. The TOA determined the EC loading in units of μg/cm^2, which was converted to mass concentration (in units of μg/m^3) by using the total sampled volume as explained in Section 4.2.3 and the stain area on the filter. For each flame condition, three filters were collected and one punch (1 cm×1.5 cm) from each filter was analyzed by TOA. The bias uncertainty in the EC measurement, B_m, was estimated according to the specification of Sunset Lab EC-OC analyzer as follows

$$B_m = 0.1 \ \frac{\mu g}{cm^2} + 0.05 m_{EC} \tag{4.2}$$

where mass of EC, m_{EC}, was in units of μg/cm^2. The precision uncertainty was estimated based on the three measurement repeats. The total uncertainty in the EC mass concentration was calculated by propagation of bias and precision uncertainties (refer to Appendix D for details of the uncertainty analysis).

Table 4.1 shows the summary of absorption coefficient and EC mass concentration with their corresponding uncertainties for particle emissions sampled at HAB=537 mm for methane-only and methane-NaCl flames. The results show that both the absorption coefficient and the mass concentration of EC increased sharply by a factor of ~3.0 when NaCl particles were added to the flame. The observed increase in the mass concentration of soot is consistent with the results seen from the particle size distributions (Section 4.3.2) and was due to oxidation inhibition by sodium near the open tip of the flame, which led to larger soot particles in greater number concentration in the post-flame region.

Additionally, Table 4.1 shows the mass-specific absorption coefficient (MAC) and single-scattering albedo (SSA) for the particle emissions of both flames. MAC is defined as (see Section 1.4)

$$MAC = \frac{B_{\text{abs}}}{M_{\text{EC}}} \tag{4.3}$$

where M_{EC} is the mass concentration of EC. If B_{abs} is in units of Mm^{-1} and m_{EC}/V has a unit of $\mu\text{g/m}^3$, then MAC has a unit of m^2/g. The SSA is a measure of the fraction of extinction due to scattering and is defined as (see Section 1.4)

$$SSA = \frac{B_{\text{scat}}}{B_{\text{ext}}} = \frac{B_{\text{scat}}}{B_{\text{scat}} + B_{\text{abs}}} \tag{4.4}$$

and is a unitless parameter. The uncertainty in MAC and SSA was determined by the propagation of total uncertainties in each term of Equations (4.3) and (4.4). For details of the uncertainty analysis refer to Appendix D.

The MAC of soot particles from the methane-only flame was 5.66±0.88 m^2/g (at 870 nm). The MAC of soot particles of different ages produced by different fuels and combustion sources has been extensively reported in the literature. For example, one highly-cited value is 7.5±1.2 m^2/g at a wavelength of 550 nm, which was reported by Bond and Bergstrom (2006) based on an average

Table 4.1: Absorption and scattering coefficients, mass concentration of EC, mass-specific absorption coefficient, and single-scattering albedo of particle emissions for methane-only and methane-NaCl flames.

Test condition	B_{abs} (Mm^{-1})	B_{scat} (Mm^{-1})	EC mass concentration ($\mu\text{g/m}^3$)	MAC (m^2/g)	SSA
Methane-only flame	25000±2800	900±90	4500±500	5.66±0.88	0.03±0.01
Methane-NaCl flame	79000±7600	4200±290	13600±770	5.82±0.65	0.05±0.01

of 17 published values in the literature. Absorption coefficient, and hence MAC, has an inverse correlation with wavelength as follows

$$\frac{B_{\text{abs, 2}}}{B_{\text{abs, 1}}} = \frac{MAC_2}{MAC_1} = \left(\frac{\lambda_1}{\lambda_2}\right)^{AAE} \tag{4.5}$$

where AAE is the absorption Ångström exponent, λ is the wavelength, and the subscripts 1 and 2 indicate two different wavelengths. AAE is approximately equal to unity for fresh soot aggregates (Liu *et al.* 2018). Thus, the value of MAC reported by Bond and Bergstrom (2006) converts to 4.74±0.76 m^2/g at a wavelength of 870 nm. Zhang *et al*. (2008) also reported a MAC of 8.7 m^2/g at 532 nm (*i.e.*, a MAC of 5.32 m^2/g at 870 nm) for fresh soot from a propane diffusion flame of a Santoro burner. The MAC value obtained in this study was consistent with the values reported in the literature within the uncertainty limits. When NaCl particles were added to the flame, the MAC of emitted particles was 5.82±0.65 m^2/g (at 870 nm). This shows that due to large uncertainties in the measurements, it was not possible to say whether or not the MAC of particles changed with the addition of NaCl particles. In a previous study, Scarnato *et al*. (2013) studied the effect of internal mixing with NaCl particles on optical properties of black carbon using a discrete dipole approximation model. They investigated different mixing configurations between soot and NaCl particles and reported a MAC enhancement of 1.0±0.0 for a lacy soot aggregate in partial surface contact with NaCl crystal (similar to the mixing state observed in this study – see Section 4.3.3) up to 2.2±0.2 for a compact soot aggregate fully enclosed (immersed) in a larger NaCl crystal.

The SSA for the particles from methane-only and methane-NaCl flames was 0.03±0.01 and 0.05±0.01, respectively, which shows a slight enhancement in the SSA when NaCl particles were added to the flame. The mixing of soot with NaCl particles amplifies both absorption and scattering, but scattering increases more than absorption due to NaCl particles and, therefore, SSA

increases. It should be noted that the SSA obtained here for soot particles (without NaCl addition) was relatively small compared to the values reported in the literature. For example, the SSA reported for fresh soot from different diffusion flames produced by Santoro burner range from 0.10–0.30 for the wavelengths in the range of 532 nm–700 nm (Schnaiter *et al.* 2003; Zhang *et al.* 2008). More recently, Moallemi *et al*. (2019) reported the SSA of soot particles from an ethylene inverted diffusion flame in the range of 0.15–0.25 at the wavelength of 870 nm. Presumably, the lower SSA seen in our study is due to smaller size parameter, defined as $x = \pi d_p/\lambda$, compared to the aforementioned studies. According to the Mie theory for spheres of carbon, for small values of x, the extinction is primarily due to absorption; however for large x, scattering and absorption are of almost equal importance (McDonald 1962). The particles in our study were smaller than those observed in the study by Moallemi *et al*. (2019), and at the same wavelength, the size parameter in our study was smaller. On the other hand, the wavelength used by Zhang *et al*. (2008) and Schnaiter *et al*. (2003) was smaller than that used in our study, leading again to a smaller size parameter in our study.

4.4 Conclusions

In this study, an open-tip sooting laminar diffusion flame, with and without sodium chloride particles introduced into the methane flow prior to combustion, was used to study the effect of the latter on the evolution of size, mixing state, and optical properties of the particle emissions. Size distribution results showed that for the methane-only flame, the soot particles underwent coagulation, partial oxidation (near the flame tip), and further coagulation as the HAB increased from 47 to 437 mm. In the case of methane-NaCl flame, the coagulation rate between soot particles decreased in the agglomeration region of the flame due to the presence of NaCl, leading to smaller soot particles at higher number concentrations. Near the open tip of the flame, the NaCl caused an

inhibition in soot oxidation by scavenging OH radicals, which led to continued coagulation of soot particles with larger particles compared to the methane-only flame. At higher heights in the post-flame region where the temperature was sufficiently low, newly nucleated NaCl particles from its vapour phase formed with a diameter of 25 nm, which was a distinct mode from that of soot in the size distributions. These results showed that the formation of soot and NaCl particles happened at different stages: although its growth and oxidation was influenced by NaCl, soot was formed inside the flame; however, NaCl was in vapour-phase inside the flame and NaCl particles nucleated at much higher heights above the flame and mixed and coagulated with soot particles subsequently. TEM images showed that these nucleated NaCl particles are mostly externally mixed and occasionally internally mixed with soot particles. TOA results showed that the mass concentration of elemental carbon (which was above 95% of the soot) increased sharply by a factor of 3.0 when NaCl was added to the flame. This indicates that the current emission inventories for flares may significantly underestimate the role of inorganic salts on flare emissions, which is a likely scenario for flaring with droplets of flowback liquids subsequent to hydraulic fracturing operations. Absorption coefficient of soot also increased by a factor of 3.0 when NaCl was added to the flame, leaving MAC essentially unchanged, and within previously reported values in the literature, for emissions from both methane-only and methane-NaCl flames. The single-scattering albedo increased slightly from 0.03 to 0.05 with the addition of NaCl, which was presumably due to additional scattering from NaCl particles.

CHAPTER 5

Size, effective density, morphology, and nano-structure of soot particles generated from buoyant turbulent diffusion flames[5]

5.1 Introduction

In this chapter, we use a lab-scale flare with gas compositions similar to those found in the upstream oil and gas industry and characterize its soot particles in terms of their size, effective density, morphology, and nano-structure (graphitization). A new experimental setup is introduced and several parameters such as gas compositions, flare diameter, and flare exit velocity are explored to study their effect on the aforementioned characteristics of soot. The results of the experiments in this chapter provides a baseline for understanding the properties of particle emissions from flares when droplets of flowback fluids are added to the flare (Chapter 6).

[5] This chapter is published in the following journal article:
Kazemimanesh, M., Dastanpour, R., Baldelli, A., Moallemi, A., Thomson, K.A., Jefferson, M.A., Johnson, M.R., Rogak, S.N., and Olfert, J.S. (2019). Size, effective density, morphology, and nano-structure of soot particles generated from buoyant turbulent diffusion flames. *J. Aerosol Sci.*, 132:22–31.

Little is known about the microphysical, morphological, and nano-structure of the soot particles produced from flares. Several previous studies have sought to estimate soot yields, *i.e.* the mass of soot per unit mass or volume of fuel, or soot emission rate, *i.e.* the mass of soot per unit time, from lab-scale or real-world flares (Johnson *et al.* 2011, 2013; McEwen and Johnson 2012; Corbin and Johnson 2014; Schwarz *et al.* 2015; Weyant *et al.* 2016; Conrad and Johnson 2017; Gvakharia *et al.* 2017). One study by Fortner *et al*. (2012) measured particle size distributions from steam- and air-assisted propane and propene flares. The study by Weyant *et al*. (2016) measured mass concentration, mass median diameter, MAC, and absorption Ångström exponent (AAE) of black carbon particles emitted from flares in the Bakken formation; however, their measurements had very large uncertainties. The study by Schwartz *et al*. (2015) have also determined the mass distribution and mass median diameter of refractory black carbon (rBC) from flares in the Bakken formation, although their results may be biased by the surrounding open biomass burnings. These studies have not characterized the morphological properties of flare-generated soot particles.

One motivation for the current study is a new technique, referred to as sky-LOSA, which has been developed to measure black carbon emission rate from real-world flares (Johnson *et al.* 2011, 2013). This method is based on line-of-sight attenuation (LOSA) techniques and relates transmissivity measurements of sky-light through the flare plume to soot concentrations via Rayleigh-Gans-Debye theory. Sky-LOSA is thus far the only remote-sensing method available to measure black carbon emission rates of real-world flares. The sky-LOSA method requires estimates of black carbon primary particle diameter, aggregate size, aggregate distribution, and fractal parameters. In the current sky-LOSA model these values are assumed based on literature data from other sources as relevant flare data is not available.

Thus, the objective of this study is to characterize the morphological and physical properties as well as nano-structure of soot particles generated from lab-scale flares simulated by buoyant turbulent flames. These parameters are explored over a range of gas compositions, flare sizes, and gas flow rates. These measurements provide fundamental information on the properties of flare-generated soot and how it compares to the properties of soot from other common sources (*e.g.* internal combustion engines). Moreover, the measurements provide an insight about whether the properties of flare-generated soot change with gas composition, flow rate, and flare size. Finally, the properties measured here can be used for input parameters for the sky-LOSA method, and the variability in the particle properties can used to better assess the uncertainty in the method.

5.2 Experimental Setup

Experiments were performed in Carleton University's lab-scale flare facility. Many instruments were used to measure and characterize particulate- and gas-phase emissions from the studied turbulent flames; however, in the present study we only show and discuss the instruments relevant to the objectives of this study. Figure 5.1 shows the schematic of the experimental setup. Gas bottles of high-purity hydrocarbons were used to create a flare gas mixture of desired composition. The fuel mixture consisted of six gaseous species, *i.e.*, methane (C1), ethane (C2), propane (C3), *n*-butane (C4), carbon dioxide, and nitrogen. The gas species in the fuel were selected based on the most prevalent species found in flare gases in the province of Alberta, Canada. The study by Johnson and Coderre (2012) derived volume-weighted flare gas composition data for 2,360 oil and bitumen batteries in the province of Alberta that reported flaring in 2008, based on analysis of more than 60,000 gas analyses from wells drawing from more than 8,500 distinct pools. In the present study, three different fuel mixture compositions were chosen which spanned the range typically seen in flared gases in the upstream oil industry based on the above-mentioned data.

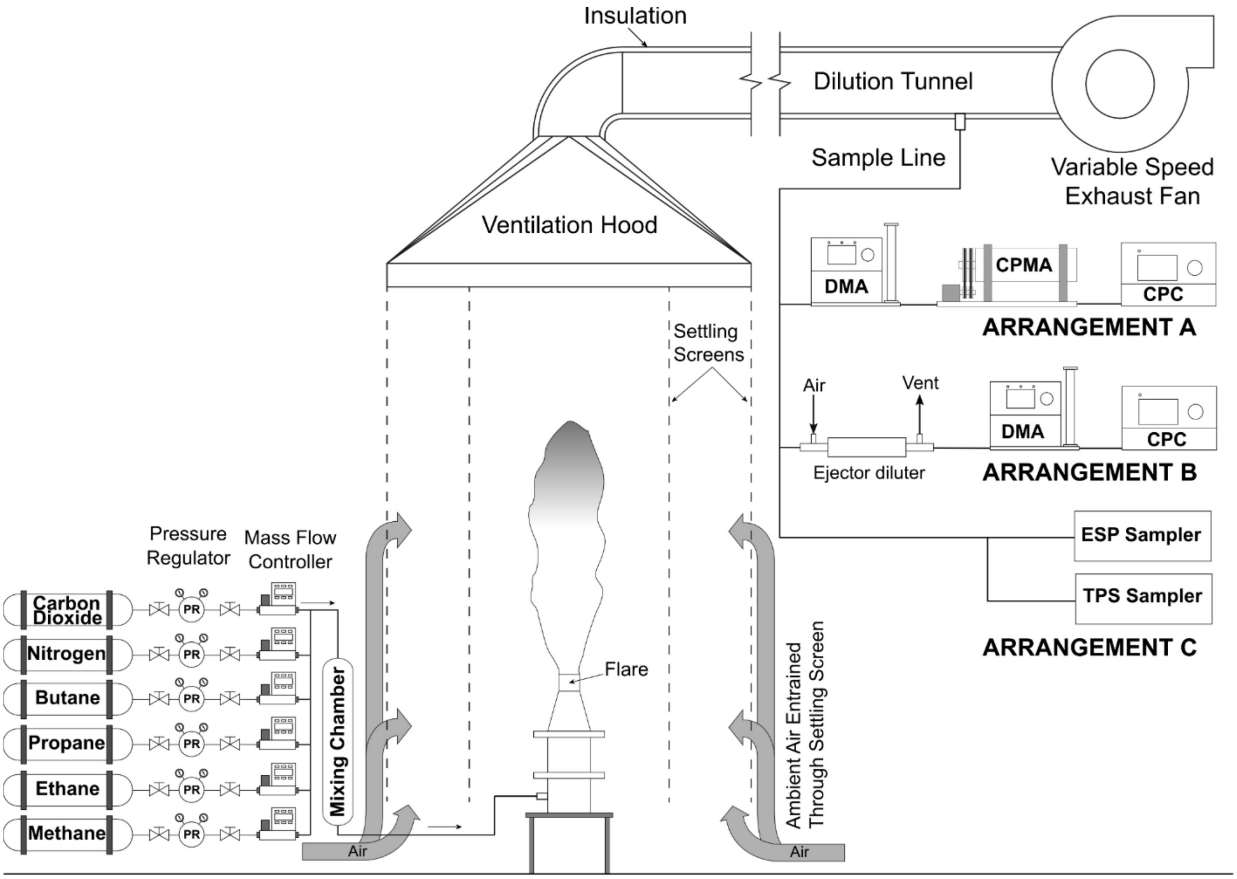

Figure 5.1: Schematic of the experimental setup showing fuel mixture metering and mixing section, the laboratory flare, the emission collection system, and various sampling instruments shown as arrangements A, B, and C.

These three fuel mixture compositions are summarized in Table 5.1. The light (L6) mixture had a composition with higher percentage of lighter alkanes (C1), whereas the heavy (H6) mixture had a composition with higher percentage of heavier alkanes (C2–C4). The flow rate of each component was set and metered using mass flow controllers (Brooks, various models) and the gaseous species mixed in a chamber prior to combustion in the flare.

Table 5.1: Fuel mixture composition (by volumetric percentage) for light, medium, and heavy mixtures

Fuel	Methane	Ethane	Propane	*n*-Butane	Nitrogen	Carbon Dioxide
Light (L6)	92.5	0.66	0.119	0.276	3.02	3.44
Medium (M6)	86.6	5.79	2.59	2.16	1.92	0.899
Heavy (H6)	76.9	11.0	5.80	4.24	1.26	0.801

The flare gas was directed to a laboratory flare with interchangeable stainless-steel exit pipes (38.1, 50.8, and 76.2 mm internal diameter and outer to inner diameter ratios of 0.89 corresponding to ASTM schedule 40 pipe typical of pipe flares). The fuel exit velocities at the burner tip were set at 0.5, 0.9, and 1.5 m/s and the fuel flow rates were adjusted accordingly for each burner size, which resulted in a range of flow rates from 60.8 to 246.3 SLPM (standard litres per minute at 0°C and 101.325 kPa). Table 5.2 summarizes the test matrix with different burner exit tube diameters and fuel exit velocities. For each flow rate in Table 5.2, the three different fuel mixture composition (L6, M6, and H6) were tested.

The emission collection system consisted of a large overhead hexagonal ventilation hood (with an included diameter of 3.1 m), a 40.6 cm round steel insulated duct, and a variable speed exhaust fan capable of drawing ~100,000 L/min. Two concentric settling screens (1.5 and 3 m diameter) surrounded the flare (suspended from the hood) to eliminate any flow disturbances around the flame that could be caused by air flows in the open lab. The flow rate of the exhaust fan was adjusted in each test case to capture the entire plume of combustion products and additional entrained ambient air. Combustion products were diluted by the entrained ambient air on the order of ~20:1 to ~120:1 as they were drawn in the hood, depending on the flow rates of the burner and exhaust fan. The exhaust fan drew the plume into the duct and vented them to the atmosphere. Emission samples were taken ~10.5 m downstream of the hood through ports installed on the duct.

Table 5.2: Test matrix and the fuel flow rate (in SLPM) corresponding to each burner exit tube diameter fuel exit velocity. For each flow rate, three fuel compositions (L6, M6, and H6) were tested.

Burner diameter	Fuel exit velocity (m/s)		
	0.5	0.9	1.5
38.1 mm (1.5 in.)	–	61.56	–
50.8 mm (2 in.)	60.80	109.45	182.41
76.2 mm (3 in.)	–	246.26	–

The samples were sequentially directed to measurement suites in Arrangement A, B, and C shown in Figure 5.1 (right) via sample transport lines.

Mass-mobility relationship and effective density of soot particles was determined using a tandem arrangement of a differential mobility analyzer (DMA; TSI Inc., Model 3081), a centrifugal particle mass analyzer (CPMA; Cambustion Ltd.), and a condensation particle counter (CPC; TSI Inc., Model 3025). This is shown as "Arrangement A" in Figure 5.1. The CPMA consists of two concentric cylinders rotating at different angular velocities and measures the mass to charge ratio of particles by balance of centrifugal and electric field forces on the particle (Olfert and Collings 2005). Soot particles were size selected based on their electrical mobility using the DMA and the average mass of the singly-charged particles of a certain mobility was measured using the CPMA. From these measurements, the mass-mobility relationship of the particles was determined using the power law as:

$$m = k d_{\mathrm{m}}^{D_{\mathrm{m}}} \tag{5.1}$$

where m is the average mass of a particle, k is the mass-mobility pre-factor, d_{m} is the particle mobility diameter, and D_{m} is the mass-mobility exponent. Thus, the effective density, ρ_{eff}, which is defined as the mass of the particle divided by the volume of a sphere with a diameter of d_{m}, was found as

$$\rho_{\mathrm{eff}} = \left(\frac{6k}{\pi}\right) d_{\mathrm{m}}^{D_{\mathrm{m}}-3}. \tag{5.2}$$

Size distributions of soot particles were measured using a scanning mobility particle sizer (SMPS; TSI Inc., Model 3938), which consisted of a differential mobility analyzer (TSI Inc., Model 3082) and a condensation particle counter (TSI Inc., Model 3788). This is shown as "Arrangement B" in

Figure 5.1. The aerosol and sheath air flow rates were 0.3 L/min and 3.00 L/min, respectively, which provided a measurement range of 15 to 661 nm. Typically, the SMPS had an up scan of 120 s and a down scan of 15 s for each measurement. The sample from the duct was further diluted by an average factor of ~9.8 using an ejector diluter (Dekati Ltd., Model DI-1000) upstream of the SPMS. The dilution factor was measured by comparing the CO_2 mole fraction of the undiluted and diluted samples for each test case using a non-dispersive infrared CO_2 analyzer (LiCor Inc., Model LI-840).

Particles were collected on Type-B carbon film supported by 300 mesh copper TEM grids (TedPella Inc., Model 01813) using both a thermophoretic sampler (TPS; in-house built – explained in Appendix E) and an electrostatic precipitator (ESP; ESPnano, Model 100), which is shown as "Arrangement C" in Figure 5.1. Samples were studied using the transmission electron microscope (Hitachi, Model H7600) operating at an accelerating voltage of 80 kV. About 30 images were taken for each flame condition. The images were analyzed with a previously validated code to derive the primary particle and aggregate size as described by Dastanpour *et al.* (2016a).

Nano-structure of soot particles was analyzed using a Raman spectrometer (Renishaw Confocal with digital stage). A 785-nm point focus laser at a power of 0.2 mW was used to avoid excessive heating of the sample. The exposure time was 10 s and the integration time was 1 s. For each sample, three Raman spectra were recorded and averaged. The soot Raman spectra were fitted using OriginPro (version 2017) software. The method of Sadezky *et al*. (2005) was used for deconvolution of different bands, which involved a baseline subtraction, a range focus of 500 to 2000 cm^{-1} for the first order peaks, data importing, and band fitting. The Raman spectra of soot was fitted with five bands as described in Table 5.3.

Table 5.3: Band descriptions and origins used in Raman spectra interpretation

Band	Description	Peak parameters
G	Graphitic planar sheet structures in soot consists of sp^2 bonded carbon atoms[a,d]. Independent of laser wavelength and intensity[b]	Lorentzian curve centered between 1571 to 1598 cm^{-1} [b,c]
D1	Induced by defects along graphitic edge planes[b,c]	Lorentzian curve centered between 1301 and 1317 cm^{-1} for 780 nm laser
D2	Attributed to PAH around soot boundaries[b, c]	Lorentzian curve centered near 1620 cm^{-1}
D3	Attributed to amorphous carbon (mixed sp^2 and sp^3 bonded carbon atoms)	Gaussian curve centered between 1489 to 1545 cm^{-1} and independent of laser wavelength and intensity[b,c]
D4	Attributed to curved PAH layers in graphitic crystallites	Lorentzian curve centered between 1127 and 1208 cm^{-1} [b,c]

[a] Saffaripour *et al*. (2017)
[b] Sadezky *et al*. (2005)
[c] Patel *et al*. (2012)
[d] Dresselhaus *et al*. (2010)

This study focussed on the ratio of average intensities of the D1 and G bands (that is, the area under each individual band denoted as I(D1)/I(G)), which will be referred to as D1/G ratio hereinafter. It was found that using 5-band fitting with floating peak locations (within the limits reported in Table 5.3) resulted in the most repeatable ratios. For example, when nine samples were re-analyzed after 6–18 months and re-fitted, the ratios increased by a mean of 2% and had a root mean square change of 7%.

5.3 Results and Discussion

5.3.1 Particle size distribution

Figure 5.2 shows the average particle size distribution for various burner sizes, exit velocities, and fuel mixtures. For each case, the particle size distribution shown is the average of at least 5 consecutive SMPS measurements. Note that each particle size distribution is corrected for the

combined dilution factor arising from the entrained ambient air and the subsequent dilution in the ejector diluter (see Section 5.2). The solid lines show the average of all test conditions for each fuel composition (light, medium, or heavy mixture). The particle size distribution changed most noticeably with the fuel mixture composition; *i.e.*, the particle median diameter and total concentration increased when the fuel composition changed from light to medium to heavy mixtures, respectively. This trend was more pronounced for particle median diameters, which were 66, 82, and 92 nm for the L6, M6, and H6 fuel mixtures. However, as seen in Figure 5.2, the particle size distribution was not a strong function of burner size or fuel exit velocity over the tested ranges of these parameters in this study.

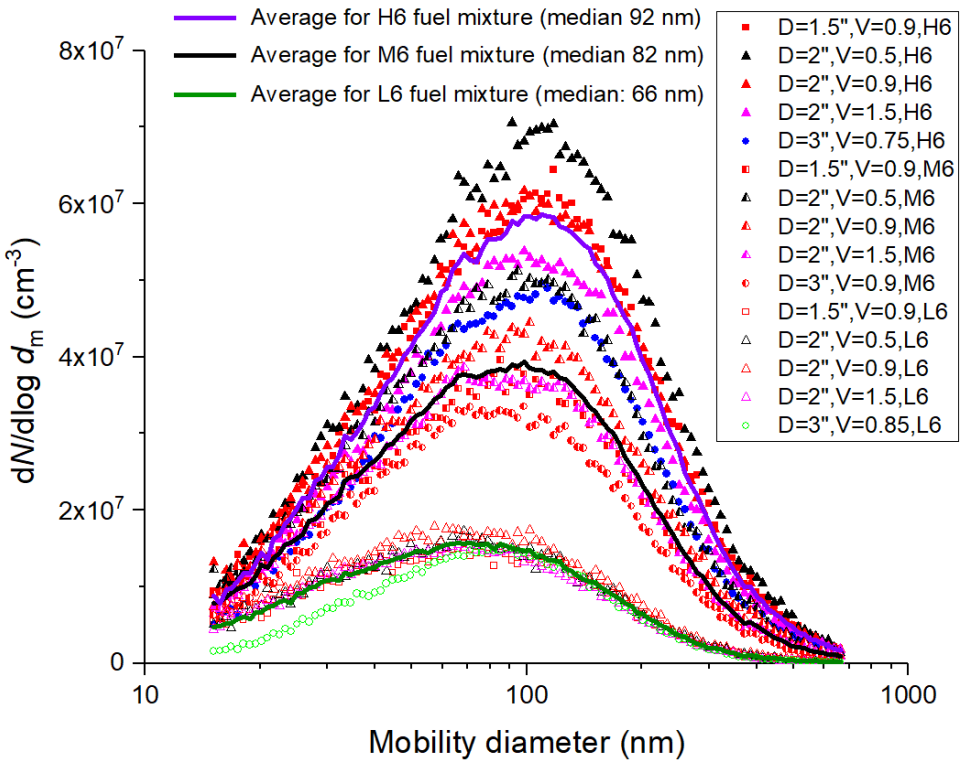

Figure 5.2: Particle size distributions for various burner diameters, exit velocities, and fuel compositions. The solid lines are the average size distributions for each fuel composition (L6, M6, H6). In the legend, D denotes flare diameter (in inches) and V denotes flare exit velocity (in m/s). Each particle size distribution is corrected for the dilution factor arising from the entrained ambient air and the subsequent dilution in the ejector diluter.

A previous study by Fortner *et al*. (2012) measured the size distribution of soot particles from steam- and air-assisted flares burning propene and propane. They reported median diameters of ~90 nm and ~80 nm in the case of propene flare with steam and air assist, respectively. In the case of steam- and air-assisted flares burning propane, the size distributions were broad with smaller median diameter (~50 nm) and lower total particle number concentration compared to propene. Although the steam- and air-assisted propene flares of Fortner *et al*. (2012) were intrinsically different from the unassisted pipe flares burning representative alkane mixtures used in the present work, our measured average particle median diameters fell within the lower and upper bounds of Fortner *et al*. (2012). We also noted that the average particle size distribution for L6 fuel mixture, which had relatively lower particle concentration, was broader compared to the case of H6 fuel mixture consistent with Fortner *et al*. (2012).

There is an extensive body of work in the literature on physical, optical, and morphological properties of soot particles inside the flames using different *in-situ* techniques; however, here we only focus on studies which measured these properties for soot particles in the post-combustion region. The dependency of soot particle concentration on fuel chemistry is expected based on previous literature. McEwen and Johnson (2012) measured soot yield (*i.e.*, mass of soot per unit mass of fuel) for buoyancy-driven turbulent diffusion flames with fuel compositions comparable to those of the present study. They measured soot volume fraction using the gravimetric method and laser-induced incandescence (LII) and found that soot yield increased linearly with the fuel mixture heating value (from ~38 to ~48 MJ/m^3) without much effect from burner size or fuel exit velocity when the burner diameter was larger than 38.1 mm and the burner exit velocity was 0.5 and 0.9 m/s. Their measurements did not provide any insight about particle median diameter or number concentration; however, the combination of soot particle diameter and number

concentration measured in the present study is an indication of soot volume fraction or mass. Thus, the qualitative trend observed in our results is in agreement with the trend of soot mass emission in McEwen and Johnson (2012) and also the field mesaurement results of Conrad and Johnson (2017).

5.3.2 Effective density of particles

Figure 5.3 shows the effective density of particles with mobility diameter of 30, 50, 85, 140, and 238 nm as selected by the DMA. A power law fit was passed through all the data points of each fuel composition (shown as solid lines in Figure 5.3) to obtain the pre-factor and exponent of the effective density-mobility relationship. As shown in the figure, the three fuel compositions have overlapping fit lines and the exponents of the fitted functions are all −0.45, which corresponds to mass-mobility exponent, D_m, of 2.55. Thus, the effective density of particles in the measured size

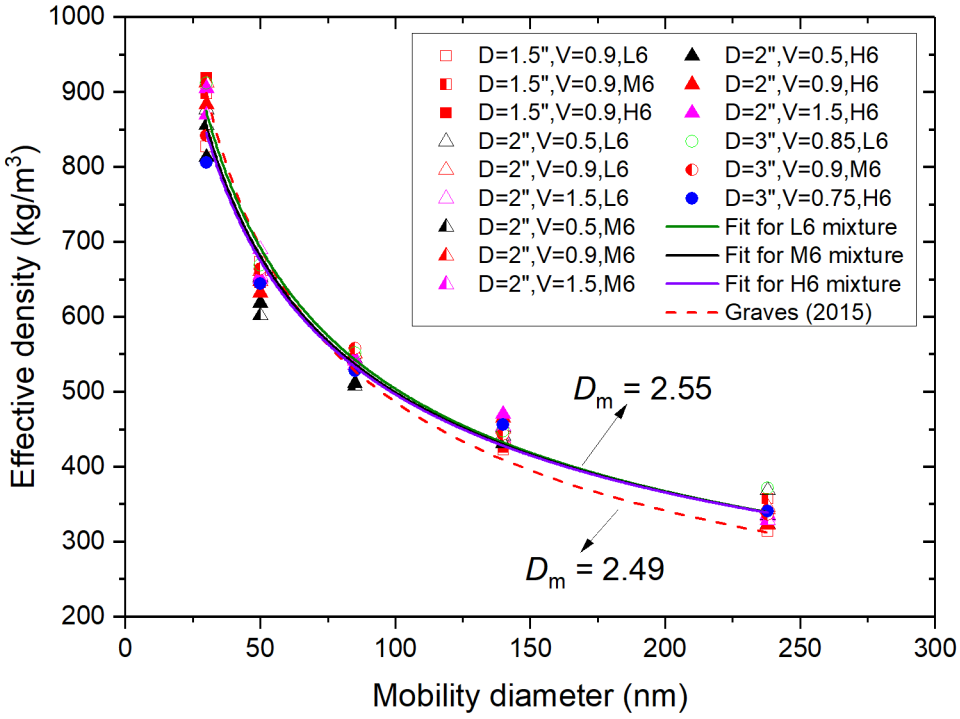

Figure 5.3: Effective density of soot particles for various burner diameters, exit velocities, and fuel compositions (L6, M6, and H6). In the legend, D denotes flare diameter (in inches) and V denotes flare exit velocity (in m/s). The solid lines show combined fit for each fuel mixture. The dashed line shows effective density measurements for soot particles from various internal combustion engines (Graves 2015).

range did not change significantly as a function of burner size, fuel exit velocity, and fuel composition. For the regression, the effective density is expressed as a function of ρ_{100}, the effective density of a 100-nm particle, and the resulting 95% confidence interval on ρ_{100} is 502 ± 5.5 kg/m^3.

The dashed line in Figure 5.3 shows the average fit function previously reported for the effective density of soot particles from various internal combustion engines, such as gasoline direction injection (GDI), diesel, port fuel injection (PFI), and high-pressure direct-injection natural gas (HPDI) engines (Graves 2015). The mass-mobility exponent of 2.55 for the soot particles in the present study agrees closely with the value of 2.49 (dashed line) derived from particles from different types of combustion engines.

5.3.3 Particle Morphology

Figure 5.4 shows representative TEM images for each fuel mixture type, *i.e.*, light, medium, and heavy; all particles exhibited the low-density fractal-like structure expected for soot. The images also show that larger aggregates tend to have larger primary particles. This relation is supported by the image analysis reported below.

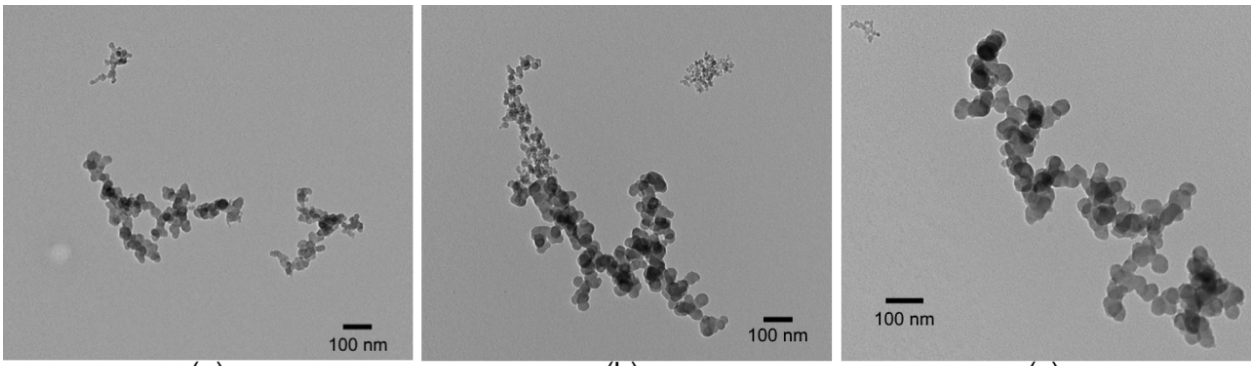

Figure 5.4: Representative TEM images of soot particles sampled from (a) light, (b) medium, and (c) heavy fuel mixture. The scale bar on each image is 100 nm.

From the TEM images, the average primary particle size was determined for each aggregate imaged based on the method described in Dastanpour *et al.* (2016a). Aggregate size was characterized by the projected area-equivalent diameter because it is expected to be close to the mobility diameter in free molecular and transition regimes as shown by Meakin *et al*. (1989) and Rogak *et al*. (1993), respectively. Figure 5.5 shows the average primary particle diameter of soot aggregates, d_p, versus their projected area equivalent diameter, d_a, for L6, M6, and H6 fuel mixtures. The black line on these plots is the best power-law fit to the TEM results. The fit is cast as

$$d_p = d_{p100}\left(\frac{d_a}{100}\right)^{D_{TEM}}. \tag{5.3}$$

Expressing diameters in nanometers, the pre-factor d_{p100} is conveniently interpreted as the primary particle size of 100-nm aggregates. Because this point is typically near the median aggregate size of the aerosol population, the confidence interval around the fitted value tends to be narrow. The uncertainties in both d_p and d_a are approximately 10%, which implies that the considerable scatter in the plots of Figure 5.5 is due to real differences between particles – consistent with the images shown in Figure 5.4. The fit was performed as a linear fit to the logarithms of d_p and d_a, consistent

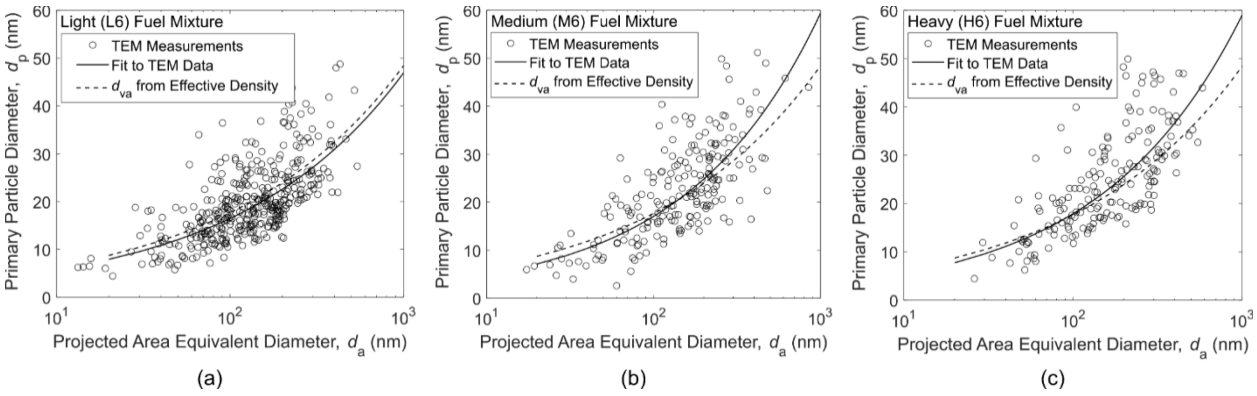

Figure 5.5: Primary particle diameter versus projected area equivalent diameter of soot particles for (a) light, (b) medium, and (c) heavy fuel mixture.

with an assumed lognormal distribution of d_p. For a given aggregate size d_a, the fitted curve then represents the geometric mean primary particle diameter; from the residuals of the fit, the geometric standard deviation is calculated as 1.33–1.40 (see Table 5.4).

The effective densities reported in Section 5.3.2 can be used to estimate the primary particle sizes using the method of Eggersdorfer *et al*. (2012) which was optimized by Dastanpour *et al*. (2016b) for soot particles from internal combustion engines, laminar flames, and gas turbines. The approach gives the Sauter mean diameter of the primary particles, d_{va}, according to,

$$d_{va} = \left(\frac{\pi k_a \rho}{6m} (d_m)^{2D_\alpha} \right)^{\frac{1}{2D_\alpha - 3}} \tag{5.4}$$

where of $D_\alpha = 1.1$ and $k_a = 1.13$ are constants empirically determined by Dastanpour *et al*. (2016b). Here, ρ is the material density of particle. The Sauter mean diameter is the diameter of a sphere that has the same volume to surface area ratio as the particle of interest. Using the mass-mobility relationship, i.e., Eq. (5.1), this can be written as

$$d_{va} = \left(\frac{\pi k_a \rho}{6k} \right)^{\frac{1}{2D_\alpha - 3}} (d_m)^{\frac{2D_\alpha - D_m}{2D_\alpha - 3}}. \tag{5.5}$$

Assuming that $d_{va} = d_p$ and $d_m = d_a$, a material density of $\rho = 1800$ kg/m^3, $k = 0.1885$ kg·m$^{-2.55}$, $D_m = 2.55$, and using diameters in nanometers, Eq. (5.5) becomes

$$d_p[\text{nm}] = 17.7 \left(\frac{d_a}{100} \right)^{0.44}. \tag{5.6}$$

The 95% confidence interval for the pre-factor is 17.7 ± 0.3 nm, from a fit to the measurements for all three fuels. The confidence interval for the exponent, straight from the regression, is 0.44 ± 0.04. The dashed black curves on the plots of Figure 5.5 represent primary particle Sauter mean diameter estimations based on mass-mobility measurements (Eq. (5.6)). The 95% confidence intervals (CI) for the TEM measurements are summarized in Table 5.4. For all fuel mixtures and both methods, the 95% confidence intervals overlap, except that the exponent derived from the TEM measurements tends to be higher than the exponent from Eq. (5.5).

These results show that previously developed relations between effective density and primary particle diameter work well for soot particles from buoyant turbulent diffusion flames. The implication of this result is that the effective density and TEM measurements provide equivalent information about the morphology of the particles and that the morphology of the soot particles from buoyant turbulent flames is very similar to other combustion sources (*e.g.*, internal combustion engines, gas turbines, and laminar flames).

A striking feature of the images in Figure 5.4 is that within each aggregate, the relative variation of primary particle size is much smaller than the variation between aggregates. Previously this was characterized by Dastanpour and Rogak (2014) by plotting geometric standard deviations of primary particles computed in two ways. The first is a measure of the "ensemble" or overall variation, $\sigma_{g,ens}$, computed as the geometric standard deviation of all primary particles ignoring their attachment to individual aggregates. The second measure is the geometric standard deviation

Table 5.4. Primary particle correlation parameters for Eq. (5.3) based on TEM measurements.

Fuel type	d_{p100} (nm)	Exponent D_{TEM}	σ_g around fit
Light (L6)	16.5 ± 0.5	0.45 ± 0.04	1.33
Medium (M6)	17.1 ± 0.9	0.54 ± 0.07	1.40
Heavy (H6)	17.9 ± 1.0	0.52 ± 0.07	1.34

of primary particles about the means of individual aggregates, $\sigma_{g,within}$. To compute this, individual primary particle sizes were measured for almost half of the aggregates.

Given sufficient coagulation time, one would expect that all primary particle sizes would be present in all aggregates, and $\sigma_{g,ens} = \sigma_{g,within}$. We found that the relative variations within aggregates, $\sigma_{g,within}$, is consistently between 1.16 and 1.31, while the overall (ensemble) relative variation, $\sigma_{g,ens}$, varies from 1.44 to 1.66. The fact that $\sigma_{g,ens} > \sigma_{g,within}$ is consistent with prior studies (Dastanpour and Rogak 2014) and with images shown in Figure 5.4.

5.3.4 Raman spectroscopy

Figure 5.6 shows 5-band fitting for a typical Raman spectrum of a sample using peak types as described in Section 5.2. Figure 5.7 summarizes the peak ratios for data aggregated by fuel type (there was no discernable trend with burner diameter or exit velocity) for samples collected on the titanium foils with the thermophoretic sampler (TPS). The error bars result from the differences between three points on the same substrate and the error propagation of the regression confidence intervals as determined by Origin Pro, however, they appear to be consistent with the variations

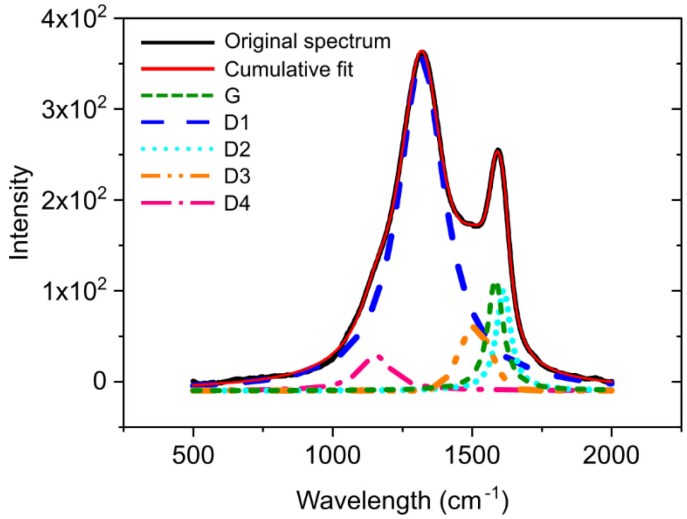

Figure 5.6: Representative Raman spectrum showing the fitted bands for the burner diameter of 50.8 mm with exit velocity of 1.5 m/s burning heavy fuel mixture.

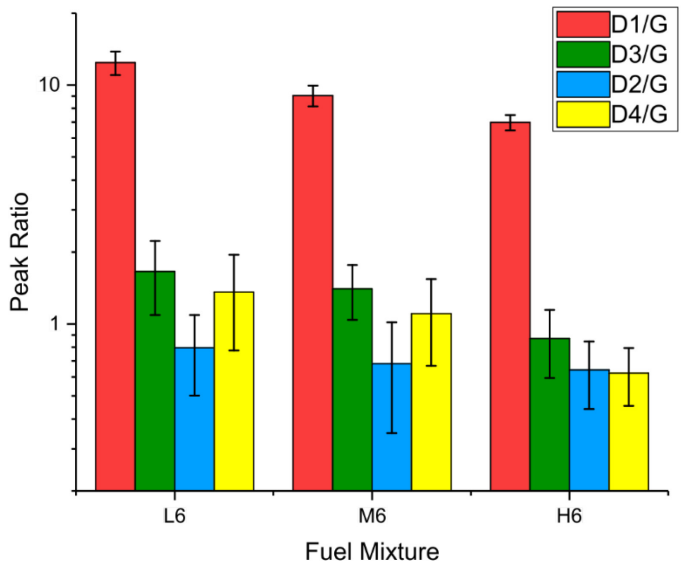

Figure 5.7: Peak ratios of D1/G, D2/G, D3/G, D4/G for all test conditions aggregated by fuel type for samples collected on titanium foils with the thermophoretic sampler.

between samples with the same fuel type but different burner diameter and exit velocity. When particular samples were reanalyzed after a period of months, the D1/G ratios were within 5–10% of the original ratios. Samples collected by the electrostatic precipitator sampler (ESP) showed a similar trend with fuel type, but with lower D1/G ratios. We believe that this is an artifact of loading levels (the electrostatic precipitator tends to produce a more uniform but less dense deposit). For the TPS samples, the Raman microscope can focus on a relatively thick soot deposit, uninfluenced by the titanium substrate, but the background subtraction becomes critical for the thin deposits on the ESP samples. When the background is taken as proportional to the titanium-only spectrum, the discrepancy between the two types of samples is reduced. Full details of the peak fits are given in Appendix F.

The peak ratios are at the upper end of the range found by Saffaripour *et al*. (2017) for lean MiniCAST flames and aircraft engine soot, and slightly higher than the values found by Dastanpour *et al*. (2017) for methane flames in a small inverted burner. For mobility-classified soot particles, Dastanpour *et al*. (2017) found that the D1/G ratio changed from 10.7 to 6.3 as the

particle mobility diameter increased from 125 to 300 nm. That change in particle diameter corresponded to a MAC increase of 25%. In the current study, a smaller change in D1/G ratio (from ~12 down to ~8) was obtained but the median mobility diameter of particles changed less (median diameters of *unclassified* particles increased from 66 to 92 nm – see Section 5.3.1).

5.4 Conclusions

In this study, the physical and morphological properties and nano-structure of soot particles from buoyant turbulent diffusion flames with fuel compositions representative of gas flares in the upstream oil and gas sector were studied. The results showed that none of the studied physical properties of soot particles such as particle concentration, median aggregate diameter, and effective density, depended on burner diameter or burner exit velocity over the range tested. However, the soot particle concentration and median aggregate diameter changed significantly with fuel mixture composition. The D1/G ratio of soot particles changed slightly with fuel mixture composition; *i.e.*, it decreased from light to heavy fuel mixture. Whether or not this change in ratio is associated with a change in optical properties would be something to investigate further. Soot particle morphology, *i.e.*, primary particle size and variation in primary particle size with aggregate size, was independent of fuel composition, burner diameter, and burner exit velocity over the range tested. Previously developed relations between effective density and primary particle size work well for the soot particles produced by buoyant turbulent diffusion flames – that is the TEM data and DMA-CPMA data provide consistent information on soot morphology. Moreover, it is expected that for instruments measuring soot emissions based on the optical properties of soot, such as Sky-LOSA, the uncertainty arising from particle morphology would be relatively small.

CHAPTER 6

Size, effective density, mixing state, and nano-structure of soot particles from turbulent diffusion flames with entrained flowback liquid droplets

6.1 Introduction

In this chapter, a lab-scale turbulent diffusion flame with gas compositions similar to that of flares in the upstream oil and gas industry is used to understand the effects of entrained flowback fluid droplets on the size, effective density, mixing state, and nano-structure of soot particulate emissions. The results of the experiments conducted in Chapter 5 showed that soot properties, such as size, concentration, and graphitization, changed significantly with gas composition and did not depend on flare diameter or exit velocity. These results provided a basis for more focused investigation of soot properties in a broader range of gas composition in this chapter. Moreover, we study the properties of particulate emissions released to the ambient air in this chapter and how flowback fluids affected these properties. To understand how these properties were arrived at, we will use the possible mechanisms found in bench-top scale flame in Chapters 3 and 4. The

measurements in this chapter provide fundamental information about the potential differences between particulate emissions from conventional flares and those subsequent to flowback operations. Furthermore, the particle emission properties measured here can be used for input parameters for the sky-LOSA method when it is used to measure the soot emission factor from the aforementioned flares. Finally, the results of this chapter can provide context for further studies on optical properties of soot from flares subsequent to flowback operations and to understand its climate forcing effects.

6.2 Experimental Setup

The experimental setup for this study was essentially identical to the setup used in Chapter 5, including the emission collection system, sampling and dilution system, and aerosol instruments used to measure and characterize the particle emissions. Here, we briefly describe the additions and modifications to the experimental setup. Similar to Chapter 5, the experiments were performed at Carleton University's lab-scale flare facility.

6.2.1 Liquid Aerosol Generation

To generate and introduce droplets of added flowback liquids to the flame, an ultrasonic atomizer (Sono-Tek Inc., Model NZL120CO) was used. The atomizer was held concentric with the burner outlet tube in an atomizer holder which was mounted on an adjustable tube. This tube also served as a conduit to deliver power and liquid to the atomizer base. The height of the ultrasonic atomizer was adjusted at ~75 mm below the exit plane of the burner outlet. This ensured that, with a narrow conical atomization pattern, no liquid droplets could hit the inner wall of the burner by visual inspection. The ultrasonic atomizer, powered with a frequency generator at 120 kHz, atomize the target liquids at flow rates of 2 mL/min and 13 mL/min. Based on the atomizer specifications, the median diameter of the droplets was 19 μm. The temperature near the exit plane of the burner was

~150 °C and, thus, it was expected that the 19-µm droplets fully evaporate within ~2 ms (Hinds 1999, p. 296). At an average flare exit velocity of 0.9 m/s, this evaporation time corresponded to a travel distance of ~1.8 mm, which means that the water in the droplets evaporated rapidly after they reached the flame.

The liquid was delivered to the atomizer via a precision micro-gear pump (Ismatec/Cole-Parmer, Model ISM901B), which had a bias uncertainty of 3%. The pump was calibrated by measuring the total mass of liquid pumped over a specific time to determine the mass flow rate, which was converted to the volumetric flow rate using the liquid density at room temperature. When switching among liquid types, the line was purged with distilled water to avoid cross-contamination of the liquid reaching the flare.

6.2.2 Flare Gas Compositions

Table 6.1 shows the summary of flare gas compositions used in this study. Gas bottles of high-purity hydrocarbons were used to create a flare gas mixture of desired composition. The flare gas was a mixture of nine gaseous species, including methane (C1), ethane (C2), propane (C3), *n*-butane (C4), *iso*-pentane (C5), *n*-hexane (C6), *n*-heptane (C7), carbon dioxide, and nitrogen. The multi-component mixtures in Table 6.1 were derived from field-measurements of flared gas in the oil and gas industry from different regions of the globe. The experiments in this study included 12 unique fuel compositions: light (AB-L9 or L9), medium (AB-M9 or M9), and heavy (AB-H9 or H9) mixtures for production sites in Alberta, Canada (Johnson and Coderre 2012); two mean compositions for the Bakken region (BK-1 (Brandt *et al.* 2016) and BK-2 (Wocken *et al.* 2013), respectively); three compositions from oil facilities in the province of Orellana, Ecuador (EC-1 through EC-3); a representative average of 20 offshore wells in the Norwegian North Sea (NS-A); two compositions at gas processing plants in Russia averaged over annual measurements from

Table 6.1: Summary of flare gas compositions in volume percentage studied in this experiment and their corresponding higher heating value (HHV).

Region	Designator	C1	C2	C3	C4	C5	C6	C7	N_2	CO_2	HHV (MJ/m^3)
Alberta, Canada	AB-L9	92.39	0.32	0.09	0.40	0.06	0.03	0.03	1.54	5.16	37.73
	AB-M9	86.36	6.83	2.36	0.97	0.33	0.13	0.18	1.62	1.22	43.81
	AB-H9	75.68	11.52	6.06	2.60	0.78	0.23	0.21	1.70	1.22	49.54
Bakken, North Dakota	BK-1	49.12	20.97	15.04	6.72	2.15	0.87	0.78	3.66	0.70	64.33
	BK-2	57.78	19.97	11.35	3.81	0.93	0.22	0.15	5.22	0.57	55.19
Orellana, Ecuador	EC-1	47.26	7.98	11.32	6.91	3.01	1.19	1.51	8.18	12.65	54.64
	EC-2	40.82	8.16	16.93	14.75	6.81	2.06	1.38	3.37	5.71	75.17
	EC-3	55.22	7.63	11.65	8.79	3.95	1.37	0.94	4.12	6.31	60.92
North Sea	NS-A	82.48	8.09	4.06	1.53	0.40	0.16	0.15	1.43	1.70	45.65
Russia	RU-1	73.96	3.08	7.87	6.79	2.35	0.63	0.57	1.90	2.85	54.15
	RU-2	77.05	5.29	8.24	4.28	1.24	0.30	0.27	1.56	1.76	51.07
	RU-3	51.90	9.81	16.90	10.27	4.68	2.93	2.40	0.95	0.15	75.43

2012 to 2017 (RU-1 and RU-2); and one representative composition of flared gas from three separation stages at an anonymous Russian oil well (RU-3) (Filippov 2013). Table 6.1 also shows the higher heating value (HHV; MJ/m^3) of the flare gas mixtures. The mixtures with lower HHV had a composition with higher percentage of lighter alkanes (C1), whereas the mixtures with higher HHV had a composition with higher percentage of heavier alkanes (C2–C7). The flow rate of each gaseous component was metered using mass flow controllers (Brooks, various models) and the gaseous species mixed in a chamber prior to combustion in the flare.

6.2.3 Flowback Fluid Composition

Four types of liquid were tested to study their effects on particle emissions from the flares: deionized water, sodium chloride solution, a surrogate flowback fluid from the Cardium formation

in Alberta, Canada for a tight-oil development (Wasylishen and Fulton 2012), and a real flowback fluid from Durvernay formation in Alberta, Canada. Deionized water was chosen as the baseline case, while sodium chloride solution (15% mass based) was selected because Na^+ and Cl^- ions are the most abundant ions in flowback fluids (see Chapter 1, Section 3). It should be noted that the easiest method to include Na^+ and Cl^- ions in water is by dissolving NaCl in water, although the mentioned ions in flowback fluids may come from other inorganic salts. The surrogate Cardium flowback fluid was made by dissolving different salts (chlorides, sulfates, and bicarbonates) of sodium, calcium, magnesium, barium, and iron (II) in deionized water, to achieve the reported ion concentrations for the actual flowback fluid and to keep the pH level of the mixture neutral. Table 6.2 shows the ion concentrations in the surrogate Cardium flowback fluid.

The real flowback fluid from Duvernay formation was acquired from the Department of Biological Sciences of the University of Alberta, which was also analyzed for composition. Table 6.3 shows the chemical composition of the Duvernay flowback fluid. The composition of Cardium and Duvernay flowback fluids show that the major cation and anion in these fluids were Na^+ and Cl^-, respectively, which is consistent with the findings in Chapter 1 (Section 3). The total dissolved solids (TDS) concentration for the NaCl solution, Cardium flowback fluid, and Duvernay flowback fluid was 150, 4.1, and 144.6 g/L, respectively. Previous studies (Jefferson 2017) have analyzed the TDS concentration (salinity) of formation water from 599 samples representing 14 formations and reported a median TDS concentration of 200 g/L, with lower and upper quartiles of 15 and 300 g/L, respectively. The minimum and maximum TDS concentration of the formation

Table 6.2: Concentration of total dissolved solids (TDS) and ions in the surrogate flowback fluid from Cardium formation

Ion	TDS	Na^+	K^+	Ca^{2+}	Mg^{2+}	Ba^{2+}	Fe^{2+}	Cl^-	SO_4^{2-}	HCO_3^-
Concentration (mg/L)	4,106	1,399	33	45	3	2	9	1,715	317	583

Table 6.3: Concentration of total dissolved solids (TDS) and ions in the real flowback fluid from Duvernay formation

Ion	TDS	Na^+	K^+	Ca^{2+}	Mg^{2+}	Ba^{2+}	Fe^{2+}	Sr^{2+}	Cl^-	Br^-
Concentration (mg/L)	144,592	47,382	1,574	6,759	614	15	185	673	83,882	228

water were 3×10^{-4} and 400 g/L, respectively (Jefferson 2017). Although flowback fluids are diluted by fracturing liquids (see Section 1.3), the values of TDS concentration reported here for formation water shows the significant variation that can be expected in the TDS concentration of flowback fluids.

6.2.4 Test Matrix

Tests on the effects of liquids on particle emissions from flares were conducted on an average flare diameter and gas flow rate of 50.8 mm (2 in.) and 156 SLPM (standard litres per minute at 0 °C and 101.325 kPa), respectively. This corresponds to an average flare exit velocity of ~1.4 m/s. Three fuel compositions (L9, M9, and H9) were used and for each composition, the four liquid types described in the previous section were tested. The flow rate of added liquids was 13 mL/min for all tests. Also, a lower liquid flow rate of 2 mL/min was used for Cardium flowback fluid and NaCl solution to investigate the effect of liquid flow rate on particle emissions. To study the effect of gas composition on flare particle emissions, tests were conducted with all 12 gas compositions and without the addition of liquid. Similar to the previous set of tests, an average flare diameter and gas flow rate of 50.8 mm and 156 SLPM, respectively, were used.

6.2.5 Measurement Instruments

Combustion products of flares were drawn into an overhead ventilation hood, which was connected to an exhaust fan via an insulated duct. The exhaust fan drew the combustion products into the duct and vented them to the atmosphere. Combustion products (and particle emissions)

were diluted by the entrained ambient air on the order of ~16:1 to ~64:1, depending on the flow rates of the gaseous mixture and the exhaust fan. Emission samples were taken ~10.5 m downstream of the hood through ports installed on the duct.

Size distributions of soot particles were measured using a scanning mobility particle sizer (SMPS; TSI Inc., Model 3938), which consisted of a differential mobility analyzer (TSI Inc., Model 3082) and a condensation particle counter (TSI Inc., Model 3788). The aerosol and sheath air flow rates were 0.3 L/min and 3.00 L/min, respectively. Typically, the SMPS had a scanning time of 120 s for each measurement. The sample from the duct was further diluted by adding a known flow rate of particle-free dry air to the sample using a mass flow controller upstream of the SMPS. The dilution factor varied from 1 to ~13.5, depending on the particle concentration in each test. The dilution factor was measured by comparing the CO_2 mole fraction of the undiluted and diluted samples for each test case using a non-dispersive infrared CO_2 analyzer (LiCor Inc., Model LI-850).

Mass-mobility relationship and effective density of soot particles was determined using a tandem arrangement of a differential mobility analyzer (DMA; TSI Inc., Model 3081), a centrifugal particle mass analyzer (CPMA; Cambustion Ltd.), and a condensation particle counter (CPC; TSI Inc., Model 3076).

To study the morphology and mixing state of particle emissions, the particles were collected on Type-B carbon film supported by 300 mesh copper TEM grids (TedPella Inc., Model 01813) using a thermophoretic sampler (TPS) identical to the one described in Chapter 5. Samples were studied using the transmission electron microscope (Hitachi, Model H7600) operating at an accelerating voltage of 80 kV.

Nano-structure of soot particles was analyzed using a Raman spectrometer (Renishaw Confocal with digital stage). A 785-nm point focus laser at a power of 0.2 mW was used. The exposure time was 10 s and the integration time was 1 s. For each sample, three Raman spectra were recorded and averaged. The soot Raman spectra were fitted by 5 bands using OriginPro (version 2017) software. The method of Sadezky *et al.* (2005) was used for deconvolution of different bands.

6.3 Results and Discussion

6.3.1 Particle size distribution

The particle size distributions shown in this section are each an average of at least 5 consecutive SMPS measurements. Note that each particle size distribution was corrected for the combined dilution factor arising from the entrained ambient air and the subsequent dilution with the mass flow controller (see Section 6.2.5).

6.3.1.1 Effect of fuel composition

Figure 6.1 shows the average particle size distribution for different fuel compositions listed in Table 6.1. The particle size distribution changed significantly with the fuel mixture composition; *i.e.*, the particle median mobility diameter and total concentration increased from lighter to heavier compositions as the HHV of the fuel mixture increased (Figure 6.2). The particle median mobility diameter changed from ~60 nm to ~120 nm as the HHV of the fuel mixture increased from 37.73 MJ/m^3 to 75.43 MJ/m^3. The total number concentration of particles increased by a factor of ~4.5 from 1.3×10^7 cm^{-3} to 5.9×10^7 cm^{-3} as the HHV of the fuel mixture increased in the aforementioned range (Figure 6.2). The increase in particle mobility diameter and total concentration with HHV is consistent with the findings in Chapter 5, although the fuel mixtures in those experiments had a smaller range of HHV.

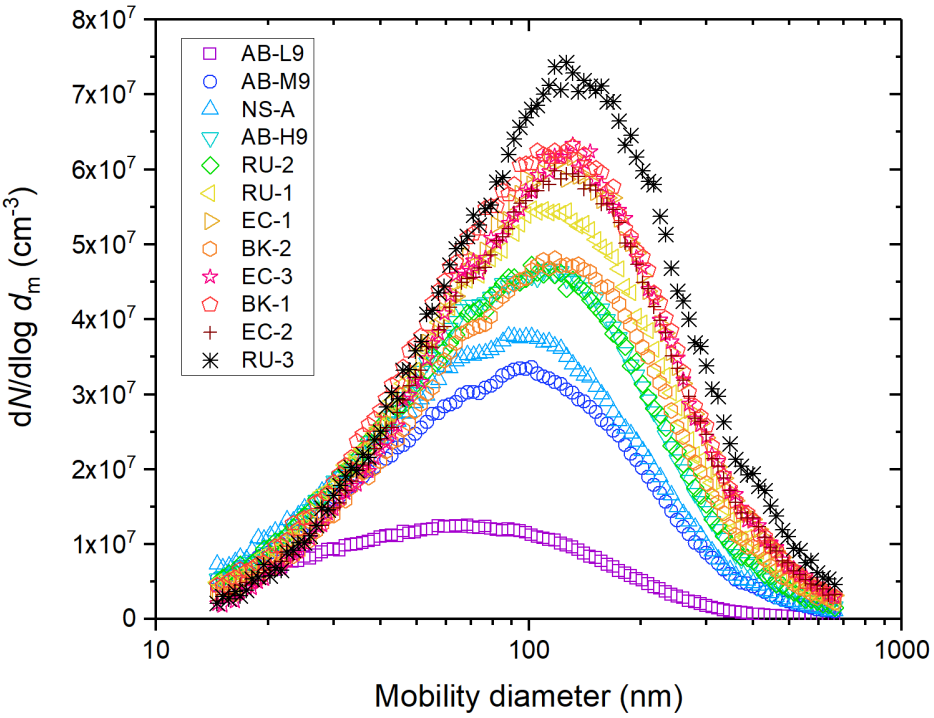

Figure 6.1: Particle size distributions for various fuel compositions. The fuels in the legend are sorted by their HHV ascendingly. Each particle size distribution is corrected for the dilution factor arising from the entrained ambient air and the subsequent dilution in the ejector diluter.

McEwen and Johnson (2012) also reported a dependency between soot emission rate and fuel chemistry. They measured soot yield (*i.e.*, mass of soot per unit mass of fuel) for turbulent diffusion flames burning 4-component and 6-component fuel compositions of C1–C4 alkanes, carbon dioxide, and nitrogen. They found that soot yield increased linearly with increasing fuel mixture heating value in the range of ~38 MJ/m^3 to ~47 MJ/m^3. The soot yield they obtained from the soot volume fraction measured by laser-induced incandescence (LII) agreed fairly well with the soot yield they obtained by using gravimetric filter analysis. In another study, Conrad and Johnson (2017) measured soot mass concentration (in g/m^3) from real flares in Ecuador by using the sky-LOSA technique (Johnson *et al.* 2010, 2011, 2013). They reported that the mass concentration of soot increased linearly with the HHV of the flare gas in the range of ~49 MJ/m^3 to ~71 MJ/m^3,

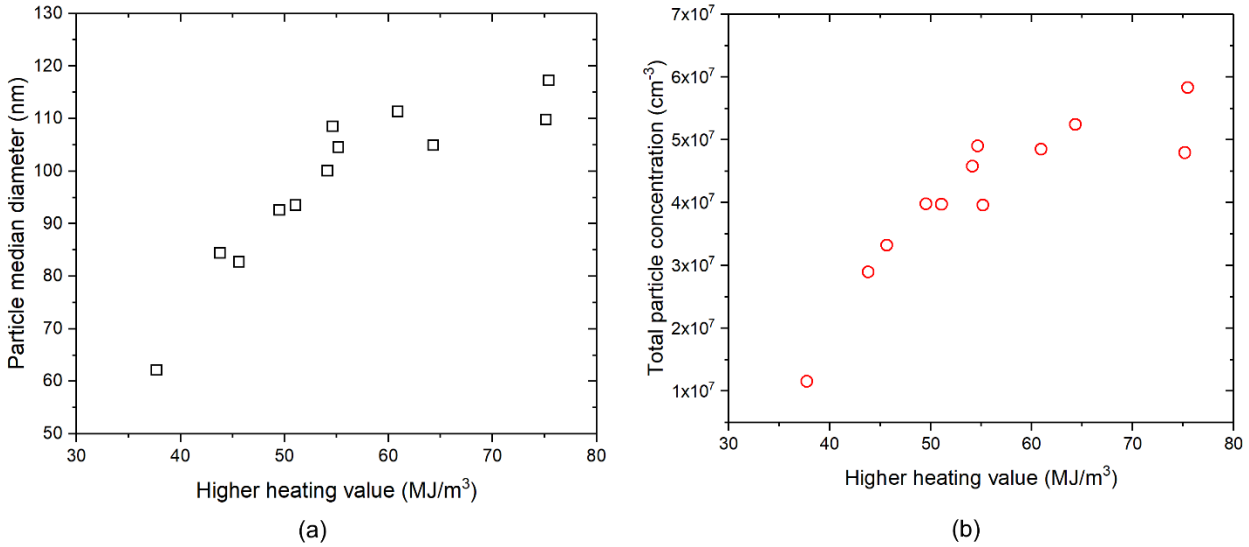

Figure 6.2: (a) Median diameter and (b) total concentration of soot particles from lab-scale flare as a function of higher heating value of the gas mixture. The plots show that median diameter and total concentration of particles increase as the higher heating value increases.

although their measured soot mass concentrations spanned more than two orders of magnitude from 0.03 to 3.85 g/m^3.

The results of the current study also indicate higher mass concentration of soot for higher HHV when we combine the soot particle diameter and number concentration via $\int \rho_{\text{eff}}(d_{\text{m}})(\pi/6)d_{\text{m}}^3 n(d_{\text{m}})d\,d_{\text{m}}$, where ρ_{eff} is the effective density of soot particles in terms of mobility diameter (taken from Section 5.3.2), d_{m} is the particle mobility diameter, and $n(d_{\text{m}})$ is the mobility diameter distribution. The results of this calculation are shown in Figure 6.3 as the mass concentration of soot particles as a function of HHV. The uncertainty in mass concentration calculated by this method was 16% based on the propagation of uncertainty in the effective density, particle number concentration, and mobility diameter (Momenimovahed and Olfert 2015). Figure 6.3 shows that the mass concentration of soot particles increases linearly with the HHV of the gas. This result is in agreement with the soot mass yield linear dependence on HHV of the fuel reported in McEwen and Johnson (2012) and Conrad and Johnson (2017). It should be noted that the estimation of soot mass concentration shown in Figure 6.3 is only valid within the range of HHV

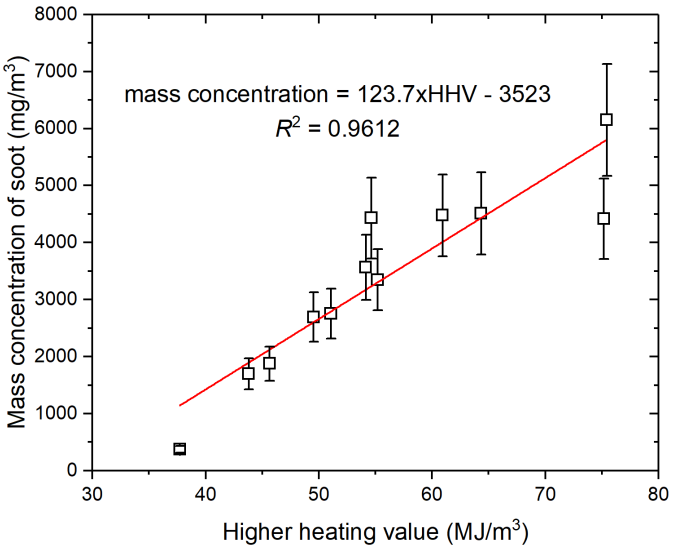

Figure 6.3: Mass concentration of soot particles as a function of higher heating value of the gas mixture. Solid line is the linear fit to the data.

shown and for the current experiments and should not be extrapolated to lower or higher HHV values.

6.3.1.2 Effect of adding liquids

Figures 6.4–6.6 show the particle size distributions in the case where liquids were added at a flow rate of 13 mL/min to the three representative fuels (L9, M9, and H9). The *y*-axis in these plots is on a logarithmic scale to clearly show orders of magnitude difference in particle size distributions when various liquids were added to the flame.

Comparing the size distribution of particles from flares with L9, M9, and H9 fuel compositions when no liquid droplet was added (Figures 6.4–6.6 and Figure 6.1), it is clear that both the median mobility diameter and the total number concentration of particles increased when the fuel composition changed from L9 to M9 to H9. This is the same trend explained in Section 6.3.1.1, where particle size and concentration increased with higher HHV of the fuel.

As can be seen in Figures 6.4–6.6, adding deionized water (DW) to all fuel compositions led to a decrease in the number concentration and the median mobility diameter of the particles. This effect was more pronounced for L9 fuel composition compared to M9 and H9 cases. The effect of adding

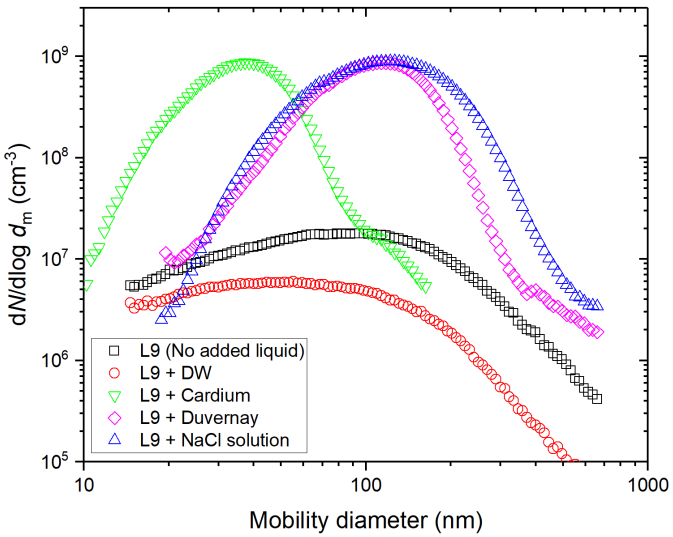

Figure 6.4: Size distribution of particles from the combustion of L9 fuel composition without and with added droplets of deionized water (DW), surrogate solution for the flowback fluids from Cardium formation (with TDS concentration of 4.1 g/L), real flowback fluid from Duvernay formation (with TDS concentration of ~145 g/L), and NaCl solution (with concentration of 150 g/L). The flow rate of the liquid was 13 mL/min for liquid types.

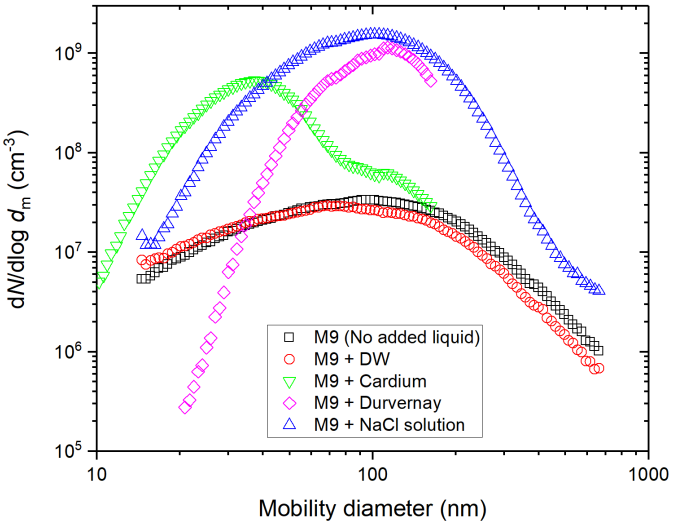

Figure 6.5: Size distribution of particles from the combustion of M9 fuel composition without and with added droplets of deionized water (DW), surrogate solution for the flowback fluids from Cardium formation (with TDS concentration of 4.1 g/L), real flowback fluid from Duvernay formation (with TDS concentration of ~145 g/L), and NaCl solution (with concentration of 150 g/L). The flow rate of the liquid was 13 mL/min for liquid types.

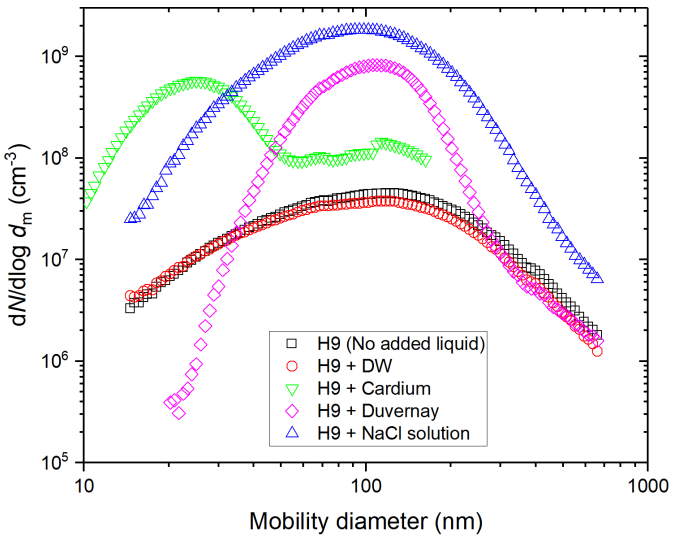

Figure 6.6: Size distribution of particles from the combustion of H9 fuel composition without and with added droplets of deionized water (DW), surrogate solution for the flowback fluids from Cardium formation (with TDS concentration of 4.1 g/L), real flowback fluid from Duvernay formation (with TDS concentration of ~145 g/L), and NaCl solution (with concentration of 150 g/L). The flow rate of the liquid was 13 mL/min for liquid types.

water on soot concentration in bench-top flames and other practical combustors has been previously reported (Cotton *et al.* 1971; Müller-Dethlefs and Schlader 1976; Dryer 1977; Greeves *et al.* 1977). This decreasing effect of water is presumably due to a thermal effect (*i.e.*, lowering of flame temperature) or to a chemical effect (reactions of hydroxyl radicals) (Hirschler 1986). Soot formation is highly influenced by flame temperature and, at lower temperatures, the formation of soot is greatly reduced (Wang 2011). Addition of water also increases the concentration of hydroxyl radicals (OH) in the flame, which in turn, cause more oxidation of soot particles and, hence, soot particle size and concentration decrease due to the enhanced oxidation (Hirschler 1986).

Adding the surrogate Cardium flowback fluid, with a TDS concentration of 4.1 g/L, to the fuel led to the generation of particles with smaller median diameter and orders of magnitude higher number concentration compared to the case of fuel with added deionized water. The particle size distribution had a main mode with a median mobility diameter of ~30–40 nm which was

presumably due to the newly nucleated salt particles and a smaller shoulder on the right with a median of ~100 nm which was presumably due to the soot particles (as shown in Section 6.3.2). The shoulder became more pronounced, in both absolute concentration and relative to the main mode, as the fuel composition changed from L9 to M9 to H9, indicating higher concentration of soot particles (see Figures 6.4–6.6). This means that a heavier fuel composition produced a higher concentration of soot particles with added Cardium flowback fluid compared to a lighter fuel composition.

The results discussed here are in agreement with the observations from a small-scale sooting diffusion flame with added salt particles (Chapter 4). The particles from the post-combustion region of the small-scale flame showed a final state with bimodal size distribution, with the leftmost mode due to nucleated salt particles and the rightmost mode due to soot particles. For the small-scale flame, the particle size distribution data and thermal-optical analysis of samples on filters showed that the concentration of soot increased when salt was added to the flame. In the case of the small-scale flame, we concluded that the increase in soot concentration was due to the inhibition of soot oxidation near the tip of the flame in the presence of alkali metal, which led to the release of soot to ambient air without undergoing oxidation. The same process was presumably responsible for the increase in soot emission when surrogate Cardium flowback fluid was added to the turbulent diffusion flame. It should be noted that the increase in soot emission from turbulent flames was a result of the combined effect of water (decreasing soot) and salts (promoting soot).

Adding Duvernay flowback fluid, with a TDS concentration of ~145 g/L, to the fuel led to particles with relatively large median diameter (~110 nm) and orders of magnitude higher number concentration compared to the deionized water case. Unlike the case of Cardium flowback fluid, the particle size distributions were mostly unimodal in this case; however, a small shoulder was

observed on the right for particles sizes greater than ~300 nm. This shoulder was presumably due the soot particles and the main mode was due to inorganic salt particles (see the effective density results in Section 6.3.2). The increase in the median mobility diameter and concentration of salt particles in the leftmost mode of Duvernay versus Cardium flowback fluid was related to a higher input of salt mass into the flame; at the same liquid flow rate (13 mL/min) and with TDS concentration of Duvernay and Cardium at ~145 g/L and 4.1 g/L, the mass flow rate of salts in Duvernay and Cardium cases was 1.88 and 0.053 g/min, respectively. This means that approximately 35 times higher mass of salt was available to re-condense into salt particles in the post-flame region in Duvernay case, which shows itself in salt particles with larger median diameter (100 nm vs. 35 nm) and higher number concentration.

Similar to the Duvernay flowback fluid, adding NaCl solution, with a concentration of 150 g/L, to the fuel led to particles with relatively large median mobility diameter (at ~100 nm) and orders of magnitude higher number concentration compared to the deionized water case. The particle size distributions were unimodal and broader (*i.e.*, greater geometric standard deviation) in this case. Presumably, in this case the main mode was due to re-nucleated NaCl particles in the post-combustion region; however, the soot mode at mobility diameter of ~300 nm was hidden inside the main mode of the particle size distribution with no apparent shoulder. This is plausible based on the effective density data for particles with mobility diameter greater than 300 nm (see Section 5.3.2).

The discussion above revealed that the amount of input salt to the flame is an important factor in the size and concentration of particle emissions from flares. Figure 6.7 shows the effect of input inorganic salts on the total number concentration and median mobility diameter of particles for the three fuel compositions studied here. The mass flow rate of inorganic salts was obtained from the

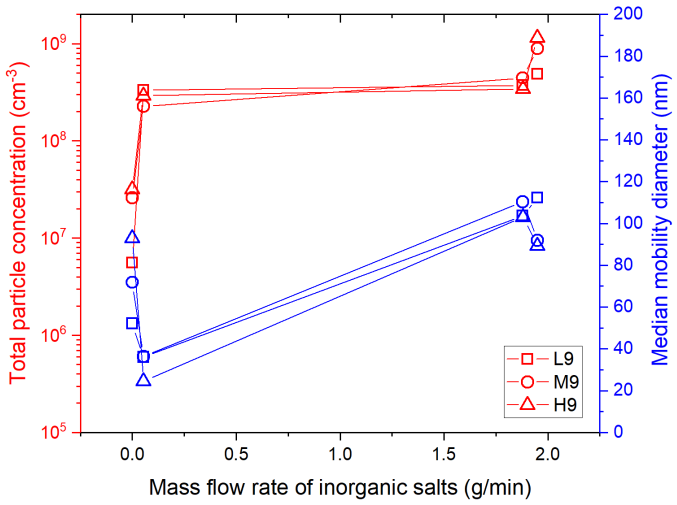

Figure 6.7: Total concentration and median mobility diameter of particles for different fuel compositions (L9, M9, and H9) versus mass flow rate of inorganic salts. In this plot, mass flow rate of zero corresponds to the case where deionized water (DW) was added to the flame. The mass flow rates of 0.053, 1.88, and 1.95 g/min correspond to the cases of Cardium flowback fluid, Duvernay flowback fluid, and NaCl solution, respectively.

flow rate and the concentration of the solution. The effect of salt was isolated from the effect of the amount of water in each flowback fluid by comparing the data against the case of deionized water at the same input flow rate for each solution (*i.e.*, 13 mL/min). The mass flow rate of inorganic salts was equal to the mass flow rate of TDS in Cardium and Duvernay flowback fluids.

It can be seen from Figure 6.7 that by adding very small amount of inorganic salts (0.053 g/min, corresponding to Cardium flowback fluid), the total particle concentration increased sharply by more than an order of magnitude and the particle median mobility diameter decreased significantly. Thus, in this case, a significantly large number of particles with small diameter is generated, presumably due to nucleation of salt particles from their vapour phase in the cooler regions above the flame. The effect of adding a very small amount of inorganic salts on total concentration of particles was more pronounced for L9 fuel composition compared to M9 and H9 fuels. On the other hand, the effect of adding a very small amount of inorganic salts on particle median diameter was less noticeable for L9 fuel composition compared to M9 and H9 fuels.

Adding more inorganic salts (to 1.88 and 1.95 g/min, corresponding to Duvernay and NaCl solution, respectively) changed the total particle concentration slightly by a factor of about two compared to an increase by more than an order of magnitude in the previous case (Cardium flowback fluid). Moreover, the particle median mobility diameter increased significantly from ~30 nm (Cardium flowback fluid) to ~110 nm (Duvernay flowback fluid) and did not change much thereafter. As mentioned earlier, this increase in the particle size was primarily due to the higher mass flow rate of salt into the flame for Duvernay flowback fluid and NaCl solution cases.

6.3.1.3 Effect of liquid flow rate

To study the effect of the flow rate of entrained liquid, experiments were conducted with Cardium flowback fluid and NaCl solution at two flow rates of 2 mL/min and 13 mL/min. Figure 6.8 shows the particle size distribution for L9, M9, and H9 fuels with added Cardium flowback fluids at these two flow rates. The particle size distributions with added droplets of NaCl solution at these flow rates are shown in Appendix G. Figure 6.8 shows that for all three gas compositions, the low liquid flow rate led to the formation of salt particles smaller in size and lower in concentration (compare the solid lines to the dashed lines in the plot). The high liquid flow rate resulted in salt particle larger in size and higher in concentration. Here, the leftmost mode of the size distributions was due to freshly nucleated salt particles, as discussed earlier in Section 6.3.1.2. For the case of H9 gas composition with 2 mL/min of Cardium flowback fluid, only a fraction of the leftmost mode was measured due to a different range of measurement. The observed change in the size and concentration of salt particles can be related to the mass input of salt into the flame in the form of droplets. At the higher liquid flow rate, the mass of salt introduced into the flame was 6.5 times greater than that of the lower liquid flow rate. Therefore, to conserve the higher input mass, re-nucleated salts particles should have larger size and higher concentration.

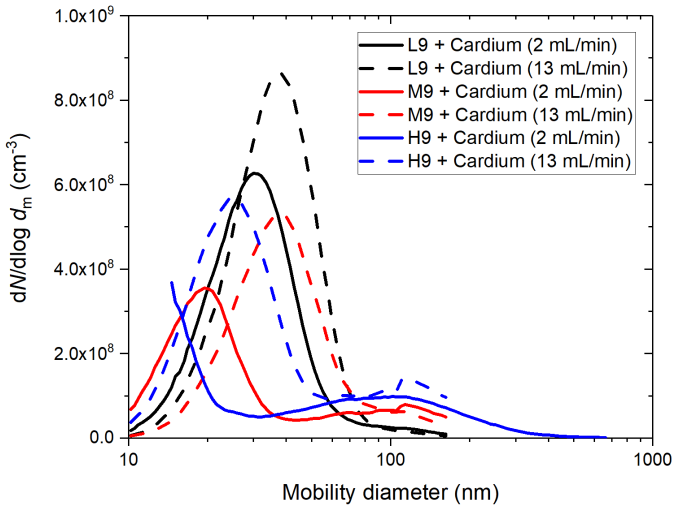

Figure 6.8: Particle size distributions for L9, M9, and H9 fuel compositions with added Cardium flowback fluid at two flow rates: 2 mL/min and 13 mL/min

The effect of the flow rate of Cardium flowback fluid on the rightmost mode, which was due to soot particles (as shown in Section 6.3.1.2), was the combined net effect of water and salt. Water decreases the concentration of soot as shown in Section 6.3.1.2, however, salts can increase the concentration of soot. The net effect on soot concentration in this case depends on the amount of water and the mass of salt.

6.3.2 Effect of adding liquid on the effective density of particles

Figures 6.9–6.11 show the number weighted average effective density of particles with mobility diameter of 50, 70, 140, 276, and 400 nm as selected by the DMA for the three fuel compositions with and without added liquids. These figures also show the effective density of solid NaCl particles (star-shaped markers) generated from drying atomized droplets of NaCl solution to make comparison with the effective density of particles from flares easier. The number weighted average effective density indicates the average effective density of particles weighted by their number concentration. For particles of a single species, this is the average effective density of a population of size-selected particles, which is the average effective density of the single species at that size.

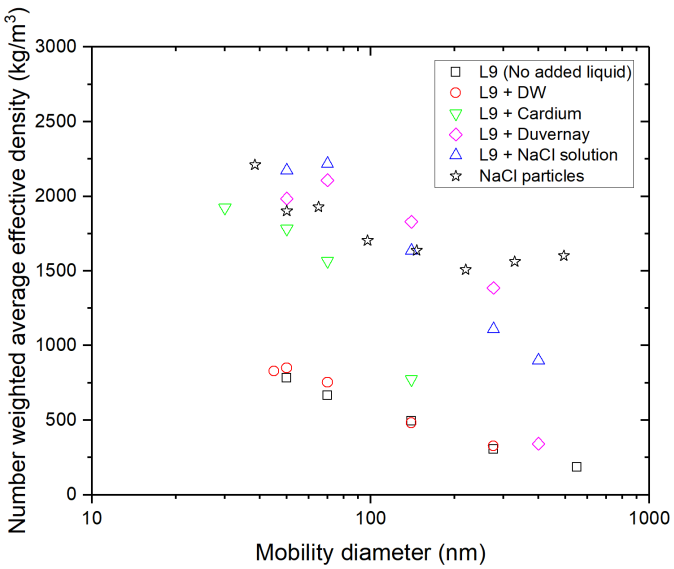

Figure 6.9: Number weighted average effective density of particles from the combustion of L9 fuel composition without and with added droplets of deionized water (DW), surrogate solution for the flowback fluids from Cardium formation (with TDS concentration of 4.1 g/L), real flowback fluid from Duvernay formation (with TDS concentration of ~145 g/L), and NaCl solution (with concentration of 150 g/L). The flow rate of the liquid was 13 mL/min for liquid types. The stars indicate the effective density of solid NaCl particles generated from drying atomized droplets of NaCl solution.

However, for a population of internally- or externally-mixed particles of two or more species, such as soot and inorganic salts, the number weighted average effective density of size-selected particles includes the effective density of externally-mixed particles of each species as well as internally-mixed particles at that size, all weighted by their abundancy (*i.e.*, number concentration).

It is clear from Figures 6.9–6.11 that when deionized water was added to the three fuel compositions (L9, M9, and H9), the effective density of soot particles did not change from that of the case with no added liquid. From Section 5.3.3, we know that effective density-mobility relationship provides equivalent information as TEM image analysis about the morphology of soot particles. Thus, we expect the morphology of soot particles to be very similar for both cases of flare with and without deionized water.

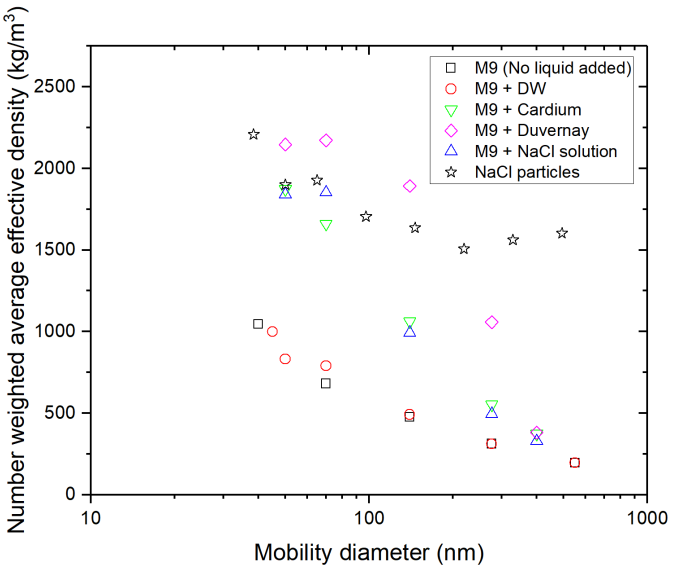

Figure 6.10: Number weighted average effective density of particles from the combustion of M9 fuel composition without and with added droplets of deionized water (DW), surrogate solution for the flowback fluids from Cardium formation (with TDS concentration of 4.1 g/L), real flowback fluid from Duvernay formation (with TDS concentration of ~145 g/L), and NaCl solution (with concentration of 150 g/L). The flow rate of the liquid was 13 mL/min for liquid types. The stars indicate the effective density of solid NaCl particles generated from drying atomized droplets of NaCl solution.

In the cases of NaCl solution and Duvernay flowback fluid added to all three fuel compositions (Figures 6.9–6.11), the number weighted average effective density of particles with mobility diameter less than ~150 nm was close to that of solid NaCl particles with the same mobility diameter. This indicated that the vast majority of particles with a mobility diameter less than 150 nm were salt particles. The effective density of particles started to deviate from that of NaCl particles and was closer to that of soot particles with the same mobility diameter when the mobility diameter was ~300 nm and larger. This indicated that most of the particles with a mobility diameter greater than 300 nm were soot. For example, in the case of Duvernay flowback fluid, the effective density of a 400 nm particle, which belonged to the rightmost shoulder of its corresponding size distribution (Figures 6.4–6.6), was close to effective density of 400 nm soot particle, indicating that the shoulder consisted mainly of soot particles and not many salt particles. This was also the case for NaCl solution added to the flame, although there was no distinct shoulder in the particle

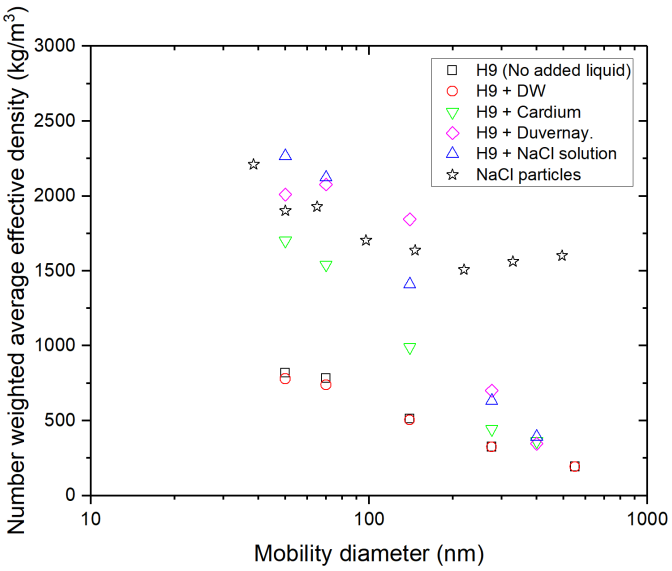

Figure 6.11: Number weighted average effective density of particles from the combustion of H9 fuel composition without and with added droplets of deionized water (DW), surrogate solution for the flowback fluids from Cardium formation (with TDS concentration of 4.1 g/L), real flowback fluid from Duvernay formation (with TDS concentration of ~145 g/L), and NaCl solution (with concentration of 150 g/L). The flow rate of the liquid was 13 mL/min for liquid types. The stars indicate the effective density of solid NaCl particles generated from drying atomized droplets of NaCl solution.

size distribution for soot particles, which means that mode due to soot particles was hidden inside the main mode of the particle size distribution.

Similar to the cases of NaCl solution and Duvernay flowback fluid, the number weighted average effective density of particles in the case of Cardium flowback fluid added to all three fuel compositions (Figures 6.9–6.11) was close to that of solid NaCl particles with the same mobility diameter when the mobility diameter was less than ~70 nm. This indicated that a large number of particles with a mobility diameter less than 70 nm were salt particles, which corresponded to the particles in the leftmost mode in the particle size distributions (see Figures 6.4–6.6). The effective density started to deviate from that of NaCl particles and was closer to that of soot particles with the same mobility diameter when the mobility diameter was greater than ~150 nm. This indicated that most of the particles with a mobility diameter greater than 150 nm were soot. Looking at the particles size distributions for the case of Cardium flowback fluid (Figures 6.4–6.6), particles with

a mobility diameter greater than 150 nm belonged to the rightmost shoulder of the size distribution, indicating that a large number of particles in the shoulder were soot particles.

It should be noted that in the case of L9 fuel composition, the number of particles larger than 200 nm was very low when deionized water or Cardium flowback fluid was added to the fuel, which made the measurement of effective density at those sizes impossible. However, in the case of M9 or H9 fuel compositions, the effective density measurements could be extended for mobility diameters up to 550 nm, because particle concentration was less affected by deionized water or Cardium flowback fluid and it was still sufficiently high to carry out the measurements.

6.3.3 Mixing state of particles

Figure 6.12 shows TEM images of particle emissions for two representative cases of Cardium flowback fluid (low TDS concentration) and NaCl solution (high TDS concentration). Soot particles from flares with and without the addition of deionized water had fractal-like structures, similar to soot particles from various combustion sources. TEM images for the case of Duvernay flowback fluid were similar to the case of NaCl solution as their TDS concentration was quite similar and, thus, the TEM images of the former are not shown here. Three categories of particles were identified in the TEM images (see Figure 6.12): individual salt particles (*i.e.*, externally mixed salt particles – shown in blue dashed circles), salt particles attached to soot aggregates (*i.e.*, internally mixed soot-salt particles – shown in green dashed line), and individual soot aggregates (*i.e.*, externally mixed soot aggregates – shown in red dashed line).

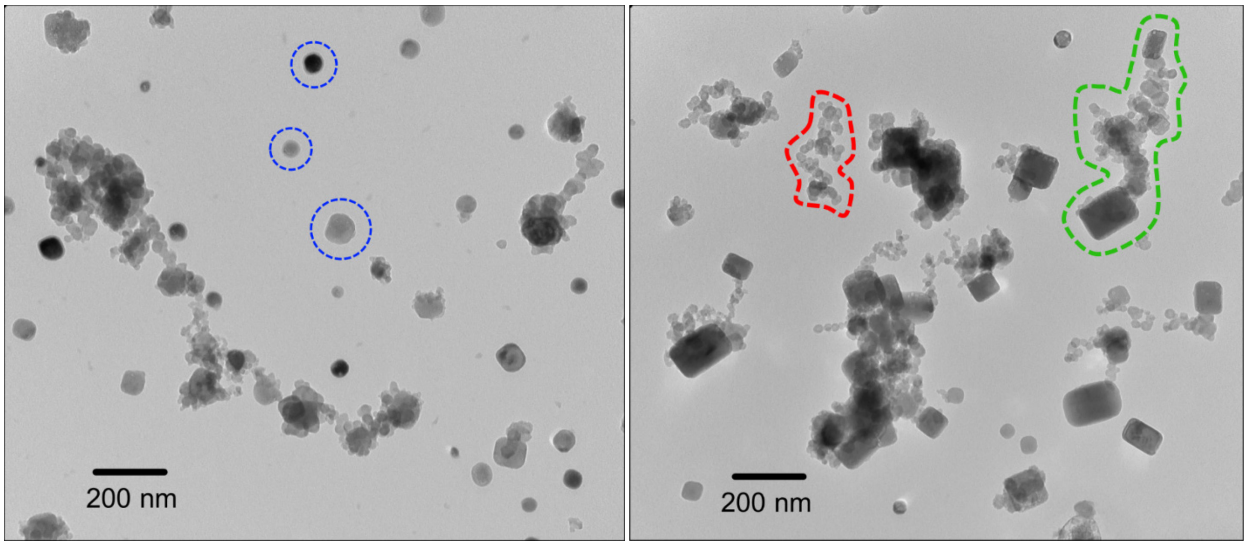

(a) (b)

Figure 6.12: TEM image of particles for the cases of (a) Cardium flowback fluid and (b) NaCl solution. Particles shown in blue dashed circles are individual salt particles with nearly spherical shape. The particle in the red dashed line is an individual soot aggregate and the particle in the green dashed line is an internally mixed soot-salt particle (*i.e.*, salt particles attached to soot aggregate).

The shape and size of salt particles depended on the TDS concentration of the flowback fluid. In the case of Cardium flowback fluid with low TDS concentration (4.1 g/L), salt particles were mostly spherical in shape and their size was relatively small (~20–50 nm). In the case of NaCl solution with high TDS concentration (150 g/L), salt particles were mostly cubic in shape and their size was relatively large (~50–200 nm). This observation agrees with the particle size distributions data of the two cases (Section 6.3.1.2), where the median diameter of particles was ~30–40 nm and ~110 nm for Cadium flowback fluid and NaCl solution cases, respectively. Figure 6.12 also shows that in the case of Cardium flowback fluid, the main (leftmost) mode of the particle size distribution (Figures 6.4–6.6) was mostly due to salt particles, which also agrees with the deduction from effective density data. Similarly, Figure 6.12 shows that in the case of NaCl solution, the main mode of the particle size distribution (Figures 6.4–6.6) was mostly due to NaCl particles, consistent with the results of effective density data.

Table 6.4: Percentage of particles which were individual salt, internally mixed soot and salt, and individual soot for Cardium flowback fluid and NaCl solution cases and the number of particles analyzed in each case.

Liquid additive	Percentage of particles by type			Number of particles analyzed
	Salt alone	Internally mixed	Soot alone	
Cardium flowback fluid	44	48	8	798
NaCl solution	52	47	1	527

Although the samples collected on TEM grids were slightly overloaded, it was desirable to estimate the fraction of particles which were internally or externally mixed. To this end, several hundred particles were analyzed manually in the TEM images of Cardium flowback fluid and NaCl solution cases. Table 6.4 shows the number of particles analyzed in each case and the percentage of particles which were individual salt, individual soot, and internally mixed soot and salt. These results reveal that only a small percentage of the particle analyzed in the two cases were individual soot particles, while the rest of the particles were almost equally either individual salt particles or internally mixed soot-salt particles. The potential climate implication of the externally-mixed salt particles are discussed in detail in Section 7.2. Briefly, these salts particle can scatter sunlight and act as cloud condensation nuclei (CCN) to form clouds, both mechanisms leading to cooling of the climate. The coagulation probability between soot and salt particles based on their concentration and residence time was ~60% in the case of Cardium flowback fluid, while the probability of particles overlapping on the grid due to overloading was ~40%. This means that the particles counted as internally mixed were in fact most probably the result of coagulation between soot and salt particles rather than an artifact due to overlap. Having said that, the values in Table 6.4 should be treated as a rough estimate of mixing state. More disperse samples should be collected in future studies to obtain more conclusive quantified results.

6.3.4 Raman spectroscopy

6.3.4.1 Effect of fuel composition

Figure 5.7 shows the D1/G ratio using Raman spectroscopy for different fuel compositions listed in Table 6.1. The error bars result from the precision uncertainty of three repeated measurements on the same substrate and the uncertainty in curve fitting (*i.e.*, the location and magnitude of peaks) as determined by Origin Pro software. The results show that the ratio of D1 (defect) band to G (graphite) band decreased from 11.4 to 5.4 as the HHV of fuel increased. From Section 6.3.1.1 we know that gas compositions with higher HHV generated larger soot particles; thus, lower D1/G ratios for higher HHV can be associated with larger soot particles which tend to have higher graphitization due to more graphitic layers in their nano-structure (Dastanpour *et al.* 2017). Saffaripour *et al.* (2017) reported D1/G ratio of 7.3 and 8 for soot particles from fuel-lean flames produced by MiniCAST soot generator and aircraft engines, respectively, and D1/G ratio of 5.8 for soot particles from fuel-rich flames produced by MiniCAST. The D1/G peak ratios reported by Saffaripour *et al.* (2017) for soot from fuel-lean flames and aircraft engines are in the middle

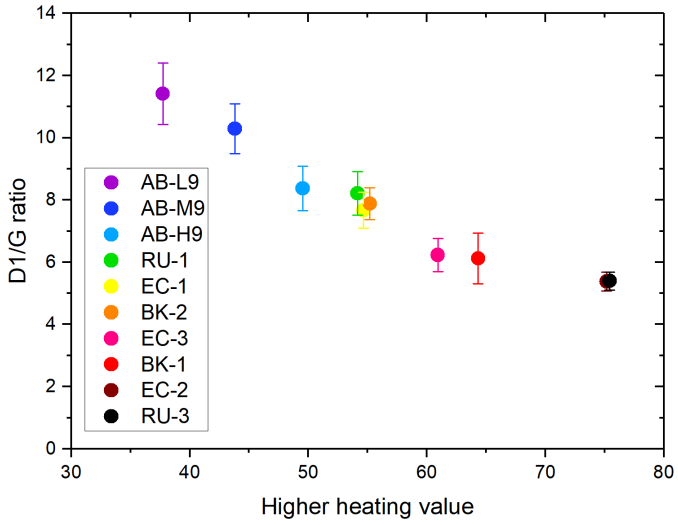

Figure 6.13: Peak ratio of D1/G bands versus higher heating value of different fuel compositions. In the legend, the fuels are sorted with their higher heating value ascending.

of the range found in the current study. The D1/G ratio reported by Saffaripour *et al.* (2017) for soot from fuel-rich flames was similar to that of high HHV fuel composition in our current study. Dastanpour *et al*. (2017) also determined the graphitization level of mobility-classified soot particles from an inverted co-flow methane-air flame and reported that the D1/G ratio decreased from 10.7 to 6.3 (*i.e.*, ~40% decrease) as the particle mobility diameter increased from 125 to 300 nm. In the current study, the D1/G ratio decreased from 11.4 to 5.4 (*i.e.*, ~50% decrease) as the median mobility diameter of a population of soot particles (as opposed to size-selected particles) increased from ~60 nm (AB-L9 fuel) to ~120 nm (RU-3 fuel) (see Section 6.3.1.1).

6.3.4.2 Effect of flowback fluid

Figure 6.14 shows the D1/G peak ratio using Raman spectroscopy for L9, M9, and H9 fuel compositions without and with add droplets of deionized water, Cardium flowback fluid, Duvernay flowback fluid, and NaCl solution. Similar to the previous section, the error bars result from the precision uncertainty of three repeated measurements on the same substrate and the uncertainty in curve fitting. The plot shows that the D1/G peak ratio decreased noticeably with gas composition from L9 to H9 consistent with the results in Section 6.3.4.1; however, it did not change significantly with the addition of different liquids. Although it seems that the D1/G peak ratio increased slightly with the addition of Cardium and Duvernay flowback fluids, the uncertainties in these measurements were large and overlap with the results of other liquids. Thus, we cannot say from these results whether or not the addition of different liquids affected the graphitization level of soot particles. Our previous results showed that the formation of soot in the flame and the nucleation of salt particles from their vapour phase occur at different time-temperature history and the two types of particles are mixed subsequent to their formation.

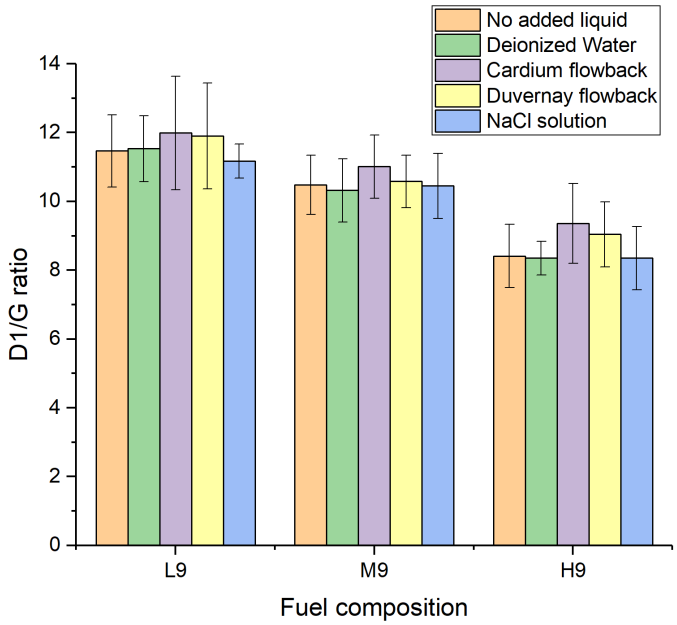

Figure 6.14: D1/G peak ratio of particles from L9, M9, and H9 fuel compositions without and with add droplets of deionized water, Cardium flowback fluid, Duvernay flowback fluid, and NaCl solution. The plot shows that the D1/G peak ratio decreased noticeably with gas composition; however, it did not change significantly with the addition of different liquids.

6.4 Conclusions

In this study, the effects of flowback fluids on the size, effective density, mixing state, and nano-structure of soot particles from buoyant turbulent diffusion flames with added droplets of flowback fluids were studied. Furthermore, the effects of fuel composition, representative of gas flares in the upstream oil and gas industry, on the size and nano-structure of the soot particles were studied. The results showed that the soot particle concentration and median aggregate diameter increased with the higher heating value of the fuel in the range tested. The D1/G ratio of soot particles decreased as the soot particles became larger when higher heating value of the fuel increased, indicating more graphitization in larger soot particles. Whether or not this change in graphitization level can affect the light absorption properties of soot would be something to investigate further. The addition of deionized water decreased the concentration and median diameter of the soot; however, adding only a small amount of salt, increased the particle concentration by more than an order of magnitude and decreased the particle median diameter significantly. This was due to

nucleation of salt particles from their vapour phase in the cooler post-flame regions. Adding more salt, increased the particle diameter significantly while the particle concentration increased slightly. Effective density results showed that the density of particles smaller than ~150 nm was similar to that of salt and the density of particles larger than ~300 nm was close to that of soot, indicating that small particles were mainly salt, while larger particles were mostly soot. This result was also confirmed by TEM images of the particles. TEM images also showed that most of the particles were individual salt particles in spherical or cubic shape and internally mixed soot and salt particles. Future studies can explore whether or not the light absorption of soot particles change when they are internally mixed with salt.

CHAPTER 7

Conclusion and Recommended Future Work

7.1 Summary

In this thesis, we studied the particle emissions from gas flares in the upstream oil and gas industry during flowback operations subsequent to hydraulic fracturing of oil/gas wells. Two experimental setups with different physical scales were used to understand the potential effects of flowback fluids on the microphysical, morphological, and optical properties as well as mixing state of particulate emissions from flares.

In the first experimental setup, a benchtop laminar diffusion flame (Santoro burner) was used under closed-tip (non-smoking) and open-tip (smoking) conditions. Methane was used as the fuel because it is a major component of flare gas in the UOG industry. Sodium chloride particles were added to the laminar flame under both conditions (non-smoking and smoking), since Na and Cl ions are the most abundant ions found in flowback fluids in the UOG industry. The main objective of these experiments was to understand how NaCl affects soot formation and evolution inside the flame and in the post-flame region. A high dilution sampling system with a dynamic range of

dilution ratio was designed and validated to sample nanoparticles (soot and non-soot) at very high concentrations from a high-temperature reacting flow. Using this dilution and sampling system, the coagulation between nanoparticles was minimized to an extent where particle size distributions were independent of dilution ratio.

Results from the closed-tip benchtop-scale flame revealed the soot formation and evolution along the centerline of the laminar flame from soot inception and surface growth to coagulation, agglomeration, and oxidation. Adding NaCl to the flame caused a decrease in the size of soot particles in the agglomeration region of the flame while its concentration increased. This was due to a reduction in coagulation rate between soot particles because the sodium ions changed their charge state. It was also found that NaCl would exist in vapour phase due to the high temperature of the reacting flow. When the laminar flame had an open tip (smoking), the NaCl caused an inhibition in soot oxidation near the tip of the flame. It was proposed that the oxidation inhibition was due to the scavenging of hydroxyl radicals — responsible for soot oxidation — by sodium ions. The inhibition in soot oxidation caused the soot particles to grow larger in size due to coagulation and release into the post-flame region. The NaCl vapour could re-condense as solid particles at lower temperatures in the post-flame region. The size distribution of particles in their final mixing state in the post-combustion region was bimodal: the leftmost mode at ~25 nm due to the freshly nucleated NaCl particles and the rightmost mode at ~140 nm due to the soot particles surviving the flame. Electron microscopy images showed that soot and NaCl particles existed mostly as individual particles separate from each other, i.e. externally mixed, and occasionally NaCl particles were attached to the soot particles, i.e. internally mixed. It was also learned that the formation of soot particles occurs at a separate stage inside the flame, while the formation of NaCl particles happens at lower temperatures outside the flame and soot and NaCl particles subsequently

mix. Thermal-optical analysis also showed that the mass concentration of soot increased by a factor of 3.0 when NaCl was added to the flame, which was due to larger soot particles (~40% larger) with higher number concentration by several times. This indicates that the current emission inventories for flares may significantly underestimate the role of inorganic salts on flare emissions. Absorption coefficient of soot also increased by a factor of 3.0 when NaCl was added to the flame; however, the mass-specific absorption coefficient (MAC) did not change noticeably with and without added NaCl.

In the second experimental setup, a lab-scale pipe flare, with a large buoyant turbulent diffusion flame, was used with and without entrained droplets of flowback fluids. The gas compositions studied were representative of gas flares in the upstream oil and gas industry. Four types of liquids were atomized and introduced into the flame: deionized water, a surrogate solution for the flowback fluids from the Cardium formation, and a real flowback fluid from the Duvernay formation. The main objective of these experiments was to understand how these fluids affect the size, effective density, nano-structure, and mixing state of the particle emissions from the flare. Moreover, we wanted to investigate how these properties would change with flare diameter, flare exit velocity, or gas composition.

The results from the lab-scale flare without entrained liquids showed that none of the studied physical properties of soot particles such as particle concentration, median diameter, and effective density, depended on flare diameter or exit velocity over the range tested. However, the soot particle concentration and median diameter changed significantly with gas composition and both were higher for gases with greater higher heating value (HHV). The D1/G ratio of soot particles (i.e. the level of amorphous to graphitized carbon) decreased from lighter compositions to heavier compositions with greater HHV. Data from TEM image analysis and effective density data provide

consistent information on soot morphology. Flare soot had an effective density (and hence, a morphology) similar to that of soot from various combustion engines. Moreover, soot particle morphology was independent of gas composition, flare diameter, and flare exit velocity over the range tested. When liquid droplets were introduced into the flame, particle properties changed more significantly. The addition of deionized water decreased the concentration and median diameter of the soot; however, adding only a small amount of salt, increased the particle concentration by more than an order of magnitude and decreased the particle median diameter significantly. This was due to nucleation of salt particles from their vapour phase at lower temperatures in the post-flame region. Adding more salt, increased the particle diameter significantly while the particle concentration increased slightly. Effective density results showed that the density of particles smaller than ~150 nm was similar to that of salt and the density of particles larger than ~300 nm was close to that of soot, indicating that small particles were mainly salt, while larger particles were mostly soot. This result was also confirmed by TEM images of the particles. TEM images also showed that most of the particles were individual salt particles — in spherical or cubic shape — and internally mixed soot and salt particles. Although soot and salt particles were internally mixed, D1/G ratios showed that the addition of liquids did not change the nano-structure (graphitization) of soot from a certain gas composition.

7.2 Climate implications

Radiative forcing (RF) is the difference between absorbed incoming solar radiation and Earth's outgoing thermal radiation (Forster *et al.* 2007). The aerosols in the atmosphere, such as black carbon (BC), organic carbon, sulfates, mineral dust, sea salt, *etc.*, can affect the global climate directly or indirectly. In the direct method, the aerosols can absorb or scatter solar radiation directly and change the radiation balance of Earth-atmosphere system (Forster *et al.* 2007), which is

referred to as direct radiative forcing (DRF). On the other hand, the aerosols can also affect the climate indirectly by changing the properties of clouds, such as their reflectivity and lifetime (Forster *et al.* 2007).

Key parameters to determine the DRF due to aerosols are the aerosol wavelength-dependent optical properties (such as its single-scattering albedo, SSA, and mass-specific absorption coefficient, MAC), the atmospheric concentration (loading) of aerosols, and the time-varying geographic distribution of the aerosols (Haywood and Boucher 2000). Scattering aerosols exert a net negative DRF, which cause a net cooling effect on the climate and absorbing aerosols exert a net positive DRF, which leads to a net warming effect on the climate (Chylek and Wong 1995; Haywood and Shine 1995).

The indirect effect is the mechanism by which aerosols modify the microphysical properties (and hence reflectivity), amount, and lifetime of clouds (Forster *et al.* 2007). An important parameter to determine the indirect effect is the effectiveness of an aerosol particle to act as a cloud condensation nucleus (CCN). This depends on the aerosol size, chemical composition, and mixing state (Forster *et al.* 2007). Clouds reflect solar radiation away from Earth's surface and exert a net negative RF in the range of 0 to −2 W/m^2 (Forster *et al.* 2007). The Intergovernmental Panel on Climate Change (IPCC) reported that the cloud albedo effect (*i.e.*, the scattering of sunlight from clouds) is a key uncertainty in the RF of climate (Forster *et al.* 2007).

We now investigate the implications of our results on each of these effects. In the small-scale diffusion flame experiments (Section 4.3.4), we found out that by adding NaCl particles to the flame, the soot particle number concentration increased by a factor of ~6–7, while its mass concentration increased by a factor of ~3. Moreover, the number concentration of NaCl particles

was ~4.5 times higher than that of soot particles. In the case of intermediate-scale flare with added Cardium flowback fluid, the soot number concentration increased by a factor of ~2 and the number concentration of salt particles was ~7 times higher than that of soot particles (compared with no entrained droplets). In terms of the direct effects of these emissions on global climate, the result of our study indicate that entrained droplets in flares can lead to an increase in the absorption of solar radiation by highly-absorbing BC particles. This increase in absorption is due the increase in the number and mass concentrations of soot particles, which results in a warming effect on the climate. On the other hand, generation of scattering salt particles in large number concentrations (several times more than soot particles), can increase the scattering of solar radiation and result in a cooling effect on the climate. This increase in scattering was also observed in the small-scale flame, where the single-scattering albedo enhanced by ~66% (from 0.03 to 0.05) with the addition of NaCl particles. Finally, we did not see a noticeable change in the MAC of particles when NaCl particles were internally mixed with soot particles and, thus, we expect little change in the absorption of solar radiation by these particles.

In terms of indirect effects of particle emissions from flares with entrained droplets on global climate, an increase in the number concentration of soot particles can lead to higher number of CCN. As mentioned in Chapter 1, soot particles are extremely hydrophobic when they are freshly released from combustion sources (Section 1.4). However, as soot particles age in the atmosphere, polar surface groups form on the soot due to oxidation by atmospheric OH, O_3, SO_2, and NO_x and can cause the soot to become hydrophilic (Zuberi *et al.* 2005). Subsequently, sulfates and secondary organic aerosols (SOAs) can condense on these hydrophilic soot particles as a coating. These hydrophilic aged soot particles can take up moisture (water content) in the ambient and act as CCN. High concentration of soot particles can form smaller droplets compared to naturally-

occurring CCNs for a fixed water content in the atmosphere (Forster *et al.* 2007). By assuming fixed moisture (water content) in the atmosphere where a cloud forms, calculations show that the scattering of solar radiation by a cloud consisting of many small droplets is higher than that by a cloud of larger droplets (*e.g.*, Hinds 1999, p. 359). Thus, it is expected that the indirect effect of soot particles from flares with entrained droplets on RF is higher scattering and cooling of the climate. Moreover, salt particles can take up moisture in the atmosphere readily and form droplets via nucleated (heterogeneous) condensation (Hinds 1999), which can act as CCN. The affinity of dissolved salt for water also allows the formation of stable droplets in saturated or unsaturated environments (Hinds 1999, p. 289). The larger number concentration of small salt particles released to the atmosphere as a result of flaring with entrained droplets can increase the number of CCN and form higher concentration of small cloud droplets. Similar to the case of soot acting as CCN, the scattering of solar radiation is expected to increase by clouds formed from emitted salt particles, leading to a cooling effect on climate.

To summarize, the direct effect of increased soot concentration on RF is positive (warming the climate), while the direct effect of increased salt concentration on RF is negative (cooling the climate). The indirect effect of increased soot and salt concentrations on RF is negative (cooling the climate) due to the formation of clouds. Although we cannot calculate the net climate effect (warming or cooling) as a result of all these processes, our results imply that such effects can be significant and require further study to determine the emission factor of soot and salt particles to be able to estimate their effect on global climate. Moreover, as mentioned previously, current emission inventories for flares may significantly underestimate the soot emission factor. Thus, it is possible that the atmospheric models which uses these inventories, significantly underestimate the warming/cooling effects of flaring on global climate.

7.3 Future work

Based on the results of this thesis, several suggestions for further work are recommended:

- The results from our lab-scale flare experiments showed that soot and salt particle can be internally mixed. We could not see a noticeable change in the MAC of particle emissions from the bench-top flame. Future studies can explore the MAC of particle emissions from lab-scale flares with entrained droplets of salt solution with a wide range of salt concentration. If an enhancement in MAC of soot is found with the addition of salts, as previous modelling works imply, this could have significant implications for estimating the net cooling/warming effect of soot from flares.

- Future works should shed light on the amount of droplet entrainment in the flare. Without knowing this, any effort to quantify the emission factors will be considered as bounding the potential effects and not the actual emission factor. Using emission spectroscopy to correlate the intensity of sodium and other ions peaks with their corresponding concentration might be one method to achieve this.

- Thermal-optical analysis can be used with the lab-scale flare to quantify the mass concentration of elemental carbon when salt solution with a wide range of concentration is added to the flame. The results in our work showed that inorganic salts can have a significant effect on increasing the mass concentration of soot emissions from flames by several times. If this is proved further with lab-scale flares, then the current emission inventories for flares may significantly underestimate flare emissions for flaring, which can lead to erroneous estimation of the climate effects of flaring with entrained droplets.

- On a fundamental level, experiments can be done to create a 2-D mapping of particle evolution in a small-scale laminar flame. This can be done by measuring particle size distributions at different radial positions at selected heights above the burner. The results from such experiments would be useful in understanding if the transport of particles from a lateral position (such as flame wing) to a downstream central position is important.

- Finally, some previous studies have shown that potassium has a much greater effect on soot formation compared to sodium due to lower ionization energy. Although the concentration of potassium is less than that of sodium in flowback fluids, it is worth investigating its individual effect or combined effect with sodium on soot formation in a small-scale flame.

Bibliography

Abdul-Wahab, S., Ali, S., Sardar, S., and Irfan, N. (2012). Impacts on Ambient Air Quality Due to Flaring Activities in One of Oman's Oilfields. *Arch. Environ. Occup. Health,* 67(1):3–14.

Abernethy, R.B., Benedict, R.P., and Dowdell, R.B. (1985). ASME Measurement Uncertainty. *J. Fluids Eng.,* 107(2):161–164.

Abid, A.D. (2009). Experimental investigation of soot nucleation and growth in premixed flat flames (PhD dissertation). University of Southern California, Los Angeles, CA.

Abid, A.D., Heinz, N., Tolmachoff, E.D., Phares, D.J., Campbell, C.S., and Wang, H. (2008). On evolution of particle size distribution functions of incipient soot in premixed ethylene–oxygen–argon flames. *Combust. Flame,* 154(4):775–788.

Abu-Rahmah, A., Arnott, W.P., and Moosmüller, H. (2006). Integrating nephelometer with a low truncation angle and an extended calibration scheme. *Meas. Sci. Technol.,* 17(7):1723–1732.

Acharya, H.R., Henderson, C., Matis, H., Kommepalli, H., Moore, B., and Wang, H. (2011). Cost effective recovery of low-TDS frac flowback water for re-use. US Department of Energy, Niskayuna, NY. Available at https://www.netl.doe.gov/sites/default/files/2018-03/FE0000784_FinalReport.pdf

Alberta Energy Regulator (2018). ST60B-2018: Upstream Petroleum Industry Flaring and Venting Report – Industry Performance for Year Ending December 31, 2017. Alberta Energy Regulator, Calgary, AB, Canada.

American Petroleum Institute (2014). Standard 521 – Pressure-relieving and Depressuring Systems. Available at www.api.org

An, Y.Z., Li, X., Teng, S.P., Wang, K., Pei, Y.Q., Qin, J., and Zhao, H. (2016). Development of a soot particle model with PAHs as precursors through simulations and experiments. *Fuel,* 179:246–257.

Appel, J., Bockhorn, H., and Frenklach, M. (2000). Kinetic modeling of soot formation with detailed chemistry and physics: laminar premixed flames of C2 hydrocarbons. *Combust. Flame,* 121(1–2):122–136.

Arnott, W.P., Moosmüller, H., Rogers, C.F., Jin, T., and Bruch, R. (1999). Photoacoustic spectrometer for measuring light absorption by aerosol: Instrument description. *Atmos. Environ.,* 33(17):2845–2852.

Ballantyne, A. and Moss, J.B. (1977). Fine Wire Thermocouple Measurements of Fluctuating Temperature. *Combust. Sci. Technol.,* 17(1–2):63–72.

Barbot, E., Vidic, N.S., Gregory, K.B., and Vidic, R.D. (2013). Spatial and temporal correlation of water quality parameters of produced waters from Devonian-age shale following hydraulic fracturing. *Environ. Sci. Technol.,* 47(6):2562–2569.

Birch, M.E. and Cary, R.A. (1996). Elemental Carbon-Based Method for Monitoring Occupational Exposures to Particulate Diesel Exhaust. *Aerosol Sci. Technol.,* 25(3):221–241.

Blondes, M.S., Gans, K.D., Engle, M.A., Kharaka, Y.K., Reidy, M.E., Saraswathula, V., Thordsen, J.J., Rowan, E.L., and Morrissey, E.A. (2018). U.S. Geological Survey National

Produced Waters Geochemical Database v2.3.

Bonczyk, P.A. (1991). Effects of metal additives on soot precursors and particulates in a $C_2H_4/O_2/N_2$/Ar premixed flame. *Fuel,* 70(12):1403–1411.

Bonczyk, P.A. (1988). Suppression of Soot in Flames by Alkaline-Earth and Other Metal Additives. *Combust. Sci. Technol.,* 59(1–3):143–163.

Bonczyk, P.A. (1983). In-situ optical measurement of additive effects on particulates in a sooting diffusion flame. *Combust. Flame,* 51:219–229.

Bond, T.C. and Bergstrom, R.W. (2006). Light absorption by carbonaceous particles: An investigative review. *Aerosol Sci. Technol.,* 40(1):27–67.

Bond, T.C., Doherty, S.J., Fahey, D.W., Forster, P.M., Berntsen, T., Deangelo, B.J., Flanner, M.G., Ghan, S., Kärcher, B., Koch, D., Kinne, S., Kondo, Y., Quinn, P.K., Sarofim, M.C., Schultz, M.G., Schulz, M., Venkataraman, C., Zhang, H., Zhang, S., Bellouin, N., Guttikunda, S.K., Hopke, P.K., Jacobson, M.Z., Kaiser, J.W., Klimont, Z., Lohmann, U., Schwarz, J.P., Shindell, D., Storelvmo, T., Warren, S.G., and Zender, C.S. (2013). Bounding the role of black carbon in the climate system: A scientific assessment. *J. Geophys. Res. Atmos.,* 118(11):5380–5552.

Botero, M.L., Chen, D., González-Calera, S., Jefferson, D., and Kraft, M. (2016). HRTEM evaluation of soot particles produced by the non-premixed combustion of liquid fuels. *Carbon,* 96:459–473.

Bradley, D., Dixon-Lewis, G., El-din Habik, S., and Mushi, E.M.J. (1985). The oxidation of graphite powder in flame reaction zones. *Symp. (Int.) Combust.,* 20(1):931–940.

Bradley, D. and Entwistle, a G. (1961). Determination of the emissivity, for total radiation, of small diameter platinum-10% rhodium wires in the temperature range 600-1450 C. *Br. J. Appl. Phys.,* 12:708–711.

Brandt, A.R., Yeskoo, T., McNally, M.S., Vafi, K., Yeh, S., Cai, H., and Wang, M.Q. (2016). Energy Intensity and Greenhouse Gas Emissions from Tight Oil Production in the Bakken Formation. *Energy & Fuels,* 30(11):9613–9621.

British Petroluem (2018). BP Statistical Review of World Energy. London, UK. Available at www.bp.com/statisticalreview

Bueno, P.A., Havey, D.K., Mulholland, G.W., Hodges, J.T., Gillis, K.A., Dickerson, R.R., and Zachariah, M.R. (2011). Photoacoustic Measurements of Amplification of the Absorption Cross Section for Coated Soot Aerosols. *Aerosol Sci. Technol.,* 45(10):1217–1230.

Bulewicz, E.M., Evans, D.G., and Padley, P.J. (1975). Effect of metallic additives on soot formation processes in flames. *Symp. (Int.) Combust.,* 15(1):1461–1470.

Bunch, A.G., Perry, C.S., Abraham, L., Wikoff, D.S., Tachovsky, J.A., Hixon, J.G., Urban, J.D., Harris, M.A., and Haws, L.C. (2014). Evaluation of impact of shale gas operations in the Barnett Shale region on volatile organic compounds in air and potential human health risks. *Sci. Total Environ.,* 468–469:832–842.

Burtscher, H., Matter, D., and Siegmann, H.C. (1993). Measurement of size distribution and photoelectric activity of particles in a gas diffusion flame. *Atmos. Environ. Part A. Gen. Top.,* 27(8):1255–1259.

Camacho, J., Lieb, S., and Wang, H. (2013). Evolution of size distribution of nascent soot in n-

and i-butanol flames. *Proc. Combust. Inst.,* 34(1):1853–1860.

Camacho, J., Liu, C., Gu, C., Lin, H., Huang, Z., Tang, Q., You, X., Saggese, C., Li, Y., Jung, H., Deng, L., Wlokas, I., and Wang, H. (2015). Mobility size and mass of nascent soot particles in a benchmark premixed ethylene flame. *Combust. Flame,* 162(10):3810–3822.

Cape, J.N., Coyle, M., and Dumitrean, P. (2012). The atmospheric lifetime of black carbon. *Atmos. Environ.,* 59:256–263.

Chapman, E.C., Capo, R.C., Stewart, B.W., Kirby, C.S., Hammack, R.W., Schroeder, K.T., and Edenborn, H.M. (2012). Geochemical and strontium isotope characterization of produced waters from Marcellus Shale natural gas extraction. *Environ. Sci. Technol.,* 46(6):3545–3553.

Chen, H.X. and Dobbins, R.A. (2000). Crystallogenesis of Particles Formed in Hydrocarbon Combustion. *Combust. Sci. Technol.,* 159(1):109–128.

Chylek, P. and Wong, J. (1995). Effect of absorbing aerosols on global radiation budget. *Geophys. Res. Lett.,* 22(8):929–931.

Ciajolo, A., Barbella, R., Tregrossi, A., and Bonfanti, L. (1998). Spectroscopic and compositional signatures of pah-loaded mixtures in the soot inception region of a premixed ethylene flame. *Symp. (Int.) Combust.,* 27(1):1481–1487.

Conrad, B.M. and Johnson, M.R. (2019). Mass absorption cross-section of flare-generated black carbon: Variability, predictive model, and implications. *Carbon,* 149:760–771.

Conrad, B.M. and Johnson, M.R. (2017). Field Measurements of Black Carbon Yields from Gas Flaring. *Environ. Sci. Technol.,* 51(3):1893–1900.

Corbin, D.J. and Johnson, M.R. (2014). Detailed Expressions and Methodologies for Measuring Flare Combustion Efficiency, Species Emission Rates, and Associated Uncertainties. *Ind. Eng. Chem. Res.,* 53(49):19359–19369.

Cotton, D.H., Friswell, N.J., and Jenkins, D.R. (1971). The suppression of soot emission from flames by metal additives. *Combust. Flame,* 17(1):87–98.

Cuesta, A., Dhamelincourt, P., Laureyns, J., Martínez-Alonso, A., and Tascón, J.M.D. (1994). Raman microprobe studies on carbon materials. *Carbon,* 32(8):1523–1532.

Cundy, V.A., Morse, J.S., and Senser, D.W. (1986). Constant-tension thermocouple rake suitable for use in flame mode combustion studies. *Rev. Sci. Instrum.,* 57(6):1209–1210.

D'Alessio, A., D'Anna, A., D'Orsi, A., Minutolo, P., Barbella, R., and Ciajolo, A. (1992). Precursor formation and soot inception in premixed ethylene flames. *Symp. (Int.) Combust.,* 24(1):973–980.

Dastanpour, R., Boone, J.M., and Rogak, S.N. (2016a). Automated primary particle sizing of nanoparticle aggregates by TEM image analysis. *Powder Technol.,* 295:218–224.

Dastanpour, R., Momenimovahed, A., Thomson, K., Olfert, J., and Rogak, S. (2017). Variation of the optical properties of soot as a function of particle mass. *Carbon,* 124:201–211.

Dastanpour, R. and Rogak, S.N. (2014). Observations of a Correlation Between Primary Particle and Aggregate Size for Soot Particles. *Aerosol Sci. Technol.,* 48(10):1043–1049.

Dastanpour, R., Rogak, S.N., Graves, B., Olfert, J., Eggersdorfer, M.L., and Boies, A.M. (2016b). Improved sizing of soot primary particles using mass-mobility measurements. *Aerosol Sci. Technol.,* 50(2):101–109.

De Filippo, A., Sgro, L.A., Lanzuolo, G., and D'Alessio, A. (2009). Probe measurements and numerical model predictions of evolving size distributions in premixed flames. *Combust. Flame,* 156(9):1744–1754.

Dennison, J., Holtz, M., and Swain, G. (1996). Raman Spectroscopy of Carbon Materials. *Spectroscopy,*.

di Stasio, S., LeGarrec, J.L., and Mitchell, J.B.A. (2011). Synchrotron Radiation Studies of Additives in Combustion, II: Soot Agglomerate Microstructure Change by Alkali and Alkaline-Earth Metal Addition to a Partially Premixed Flame. *Energy & Fuels,* 25(3):916–925.

Dobbins, R.A. and Megaridis, C.M. (1987). Morphology of flame-generated soot as determined by thermophoretic sampling. *Langmuir,* 3(2):254–259.

Dresselhaus, M.S., Jorio, A., and Saito, R. (2010). Characterizing Graphene, Graphite, and Carbon Nanotubes by Raman Spectroscopy. *Annu. Rev. Condens. Matter Phys.,* 1(1):89–108.

Dryer, F.L. (1977). Water addition to practical combustion systems—Concepts and applications. *Symp. (Int.) Combust.,* 16(1):279–295.

Dworkin, S.B., Zhang, Q., Thomson, M.J., Slavinskaya, N.A., and Riedel, U. (2011). Application of an enhanced PAH growth model to soot formation in a laminar coflow ethylene/air diffusion flame. *Combust. Flame,* 158(9):1682–1695.

Eggersdorfer, M.L., Gröhn, A.J., Sorensen, C.M., McMurry, P.H., and Pratsinis, S.E. (2012). Mass-mobility characterization of flame-made ZrO2 aerosols: Primary particle diameter and

extent of aggregation. *J. Colloid Interface Sci.,* 387(1):12–23.

Eggersdorfer, M.L. and Pratsinis, S.E. (2014). Agglomerates and aggregates of nanoparticles made in the gas phase. *Adv. Powder Technol.,* 25(1):71–90.

Elvidge, C., Zhizhin, M., Baugh, K., Hsu, F.-C., and Ghosh, T. (2015). Methods for Global Survey of Natural Gas Flaring from Visible Infrared Imaging Radiometer Suite Data. *Energies,* 9(1):14.

Escribano, R., Sloan, J.J., Siddique, N., Sze, N., and Dudev, T. (2001). Raman spectroscopy of carbon-containing particles. *Vib. Spectrosc.,* 26(2):179–186.

Etkin, D. (1990). Greenhouse warming: Consequences for Arctic Climate. *J. Cold Reg. Eng.,* 4(1):54–66.

Fenimore, C.P. and Jones, G.W. (1967). Oxidation of soot by hydroxyl radicals. *J. Phys. Chem.,* 71(3):593–597.

Ferrari, A.C. and Robertson, J. (2001). Resonant Raman spectroscopy of disordered, amorphous, and diamondlike carbon. *Phys. Rev. B,* 64(7):075414.

Feugier, A. (1978). Effect of Metal Additives on the Amount of Soot Emitted by Premixed Hydrocarbon Flames*., in Advances in Chemistry Series: Evaporation—Combustion of Fuels, J.T. Zung, ed,* American Chemical Society, pp. 178–189.

Filippov, A. (2013). Chemical composition of associated gas. *Neft. Mag.,* 22–26.

Forster, P., Ramaswamy, V., Artaxo, P., Berntsen, T., Betts, R., Fahey, D.W., Haywood, J., Lean, J., Lowe, D.C., Myhre, G., Nganga, J., Prinn, R., Raga, G., Schulz, M., and Van

Dorland, R. (2007). Changes in Atmospheric Constituents and in Radiative Forcing., *in Climate Change 2007: The Physical Science Basis. Contribution of Working Group I to the Fourth Assessment Report of the Intergovernmental Panel on Climate Change, S. Solomon, D. Qin, M. Manning, Z. Chen, M. Marquis, K.B. Averyt, M. Tignor, H.L. Miller, eds,* Cambridge University Press, United Kingdom.

Fortner, E.C., Brooks, W.A., Onasch, T.B., Canagaratna, M.R., Massoli, P., Jayne, J.T., Franklin, J.P., Knighton, W.B., Wormhoudt, J., Worsnop, D.R., Kolb, C.E., and Herndon, S.C. (2012). Particulate Emissions Measured During the TCEQ Comprehensive Flare Emission Study. *Ind. Eng. Chem. Res.,* 51(39):12586–12592.

Frac Focus (2019). Frac Focus - Chemical Disclosure Registry. Available at www.fracfocus.ca (Accessed 27 July 2019).

Frenklach, M. (2002). Reaction mechanism of soot formation in flames. *Phys. Chem. Chem. Phys.,* 4(11):2028–2037.

Frenklach, M. and Wang, H. (1994). Detailed Mechanism and Modeling of Soot Particle Formation. Springer, Berlin, Heidelberg, pp. 165–192.

Frenklach, M. and Wang, H. (1991). Detailed modeling of soot particle nucleation and growth. *Symp. (Int.) Combust.,* 23(1):1559–1566.

Gallegos, T.J. and Varela, B.A. (2015). Trends in hydraulic fracturing distributions and treatment fluids, additives, proppants, and water volumes applied to wells drilled in the United States from 1947 through 2010 : data analysis and comparison to the literature. U.S. Geological Survey, Denver, CO. Available at https://pubs.usgs.gov/sir/2014/5131/

Gandossi, L. (2013). An overview of hydraulic fracturing and other formation stimulation technologies for shale gas production (EUR 26347 EN). European Commission Joint Research Centre, Luxemburg. Available at http://dx.doi.org/10.2790/99937

Garo, A., Prado, G., and Lahaye, J. (1990). Chemical aspects of soot particles oxidation in a laminar methane-air diffusion flame. *Combust. Flame,* 79(3–4):226–233.

Ghazi, R. and Olfert, J.S. (2013). Coating Mass Dependence of Soot Aggregate Restructuring due to Coatings of Oleic Acid and Dioctyl Sebacate. *Aerosol Sci. Technol.,* 47(2):192–200.

Glarborg, P. (2007). Hidden interactions-Trace species governing combustion and emissions. *Proc. Combust. Inst.,* 31(1):77–98.

Gomaa, A.M., Mahmoud, M.A., and Nasr-El-Din, H.A. (2011). Effect of Shear Rate on the Propagation of Polymer-Based In-Situ-Gelled Acids Inside Carbonate Cores. *SPE Prod. Oper.,* 26(01):41–54.

Goodwin, D.G., Moffat, H.K., and Speth, R.L. (2016). An object-oriented software toolkit for chemical kinetics, thermodynamics, and transport processes.

Grahame, T.J., Klemm, R., and Schlesinger, R.B. (2014). Public health and components of particulate matter: The changing assessment of black carbon. *J. Air Waste Manage. Assoc.,* 64(6):620–660.

Graves, B.M. (2015). Characterization of Particulate Matter Morphology and Volatility for Two Direct-Injection Engines (MSc dissertation). University of Alberta, Edmonton, AB, Canada.

Greeves, G., Khan, I.M., and Onion, G. (1977). Effects of water introduction on diesel engine combustion and emissions. *Symp. (Int.) Combust.,* 16(1):321–336.

Gregory, K.B., Vidic, R.D., and Dzombak, D.A. (2011). Water management challenges associated with the production of shale gas by hydraulic fracturing. *Elements,* 7(3):181–186.

Gvakharia, A., Kort, E.A., Brandt, A., Peischl, J., Ryerson, T.B., Schwarz, J.P., Smith, M.L., and Sweeney, C. (2017). Methane, Black Carbon, and Ethane Emissions from Natural Gas Flares in the Bakken Shale, North Dakota. *Environ. Sci. Technol.,* 51(9):5317–5325.

Hadley, O.L. and Kirchstetter, T.W. (2012). Black-carbon reduction of snow albedo. *Nat. Clim. Chang.,* 2(6):437–440.

Haluszczak, L.O., Rose, A.W., and Kump, L.R. (2013). Geochemical evaluation of flowback brine from Marcellus gas wells in Pennsylvania, USA. *Appl. Geochemistry,* 28:55–61.

Hayes, T.D. and Severin, B.F. (2012). Characterization of Flowback Waters from the Marcellus and the Barnett Shale Regions. United States Environmental Protection Agency. Available at https://hero.epa.gov/hero/index.cfm/reference/details/reference_id/2520675

Hayhurst, A.N. and Jones, H.R.N. (1989). The effect of metallic additives on ionization and soot formation in oxyacetylene flames. *Combust. Flame,* 78(3–4):339–356.

Haynes, B.S., Jander, H., and Wagner, H.G. (1979). The effect of metal additives on the formation of soot in premixed flames. *Symp. (Int.) Combust.,* 17(1):1365–1374.

Haynes, B.S. and Wagner, H.G. (1981). Soot formation. *Prog. Energy Combust. Sci.,* 7(4):229–273.

Haywood, J. and Boucher, O. (2000). Estimates of the direct and indirect radiative forcing due to tropospheric aerosols: A review. *Rev. Geophys.,*.

Haywood, J.M. and Shine, K.P. (1995). The effect of anthropogenic sulfate and soot aerosol on the clear sky planetary radiation budget. *Geophys. Res. Lett.,* 22(5):603–606.

Heitor, M.V. and Moreira, A.L.N. (1993). Thermocouples and sample probes for combustion studies. *Prog. Energy Combust. Sci.,* 19(3):259–278.

Hepp, H. and Siegmann, K. (1998). Mapping of Soot Particles in a Weakly Sooting Diffusion Flame by Aerosol Techniques. *Combust. Flame,* 115(1–2):275–283.

Higgins, K.J., Jung, H., Kittelson, D.B., Roberts, J.T., and Zachariah, M.R. (2002). Size-Selected Nanoparticle Chemistry: Kinetics of Soot Oxidation. *J. Phys. Chem. A,* 106(1):96–103.

Hinds, W.C. (1999). Aerosol Technology: Properties, Behavior, and Measurement of Airborne Particles, 2nd ed. John Wiley & Sons, New York, NY.

Hirschler, M.M. (1986). Soot From Fires: III. Soot Suppression. *J. Fire Sci.,* 4(1):42–72.

Horner, P., Halldorson, B., and Slutz, J. (2011). Shale gas water treatment value chain - A review of technologies, including case studies*., in Proceedings - SPE Annual Technical Conference and Exhibition,* Society of Petroleum Engineers, pp. 3969–3978.

Howard, J.B. and Kausch, W.J. (1980). Soot control by fuel additives. *Prog. Energy Combust. Sci.,* 6(3):263–276.

Howard, J.B., Wersborg, B.L., and Williams, G.C. (1973). Coagulation of carbon particles in premixed flames. *Faraday Symp. Chem. Soc.,* 7(0):109–119.

Ishizuka, S. (1982). An experimental study on the opening of laminar diffusion flame tips. *Symp. (Int.) Combust.,* 19(1):319–326.

Ishizuka, S. and Sakai, Y. (1988). Structure and tip-opening of laminar diffusion flames. *Symp. (Int.) Combust.,* 21(1):1821–1828.

Janssen, N.A.H., Hoek, G., Simic-Lawson, M., Fischer, P., van Bree, L., ten Brink, H., Keuken, M., Atkinson, R.W., Anderson, H.R., Brunekreef, B., and Cassee, F.R. (2011). Black Carbon as an Additional Indicator of the Adverse Health Effects of Airborne Particles Compared with PM $_{10}$ and PM $_{2.5}$. *Environ. Health Perspect.,* 119(12):1691–1699.

Jefferson, A.M. (2017). Exploratory Experiments to Determine Effects of Injected Aerosolized Water, Hydrochloric Acid, and Sodium Chloride Solutions on Lab-Scale Flare Emissions (MSc dissertation). Carleton University, Ottawa, Ontario, Canada.

Jensen, D.E. and Jones, G.A. (1982). Kinetics of flame inhibition by sodium. *J. Chem. Soc. Faraday Trans. 1 Phys. Chem. Condens. Phases,* 78(9):2843.

Jensen, D.E., Jones, G.A., and Mace, A.C.H. (1979). Flame inhibition by potassium. *J. Chem. Soc. Faraday Trans. 1 Phys. Chem. Condens. Phases,* 75(0):2377.

Johnson, M.R. and Coderre, A.R. (2012). Compositions and greenhouse gas emission factors of flared and vented gas in the Western Canadian Sedimentary Basin. *J. Air Waste Manage. Assoc.,* 62(9):992–1002.

Johnson, M.R., Devillers, R.W., and Thomson, K.A. (2013). A generalized sky-LOSA method to quantify soot/black carbon emission rates in atmospheric plumes of gas flares. *Aerosol Sci. Technol.,* 47(9):1017–1029.

Johnson, M.R., Devillers, R.W., and Thomson, K.A. (2011). Quantitative Field Measurement of Soot Emission from a Large Gas Flare Using Sky-LOSA. *Environ. Sci. Technol.,*

45(1):345–350.

Johnson, M.R., Devillers, R.W., Yang, C., and Thomson, K.A. (2010). Sky-scattered solar radiation based plume transmissivity measurement to quantify soot emissions from flares. *Environ. Sci. Technol.,* 44(21):8196–8202.

Johnson, M.R., Kostiuk, L.W., and Spangelo, J.L. (2001). A Characterization of Solution Gas Flaring in Alberta. *J. Air Waste Manage. Assoc.,* 51(8):1167–1177.

Kasper, M., Siegmann, K., and Sattler, K. (1997). Evaluation of an in situ sampling probe for its accuracy in determining particle size distributions from flames. *J. Aerosol Sci.,* 28(8):1569–1578.

Katsuki, M., Mizutani, Y., and Matsumoto, Y. (1987). An improved thermocouple technique for measurement of fluctuating temperatures in flames. *Combust. Flame,* 67(1):27–36.

Kennedy, I.M. (1997). Models of soot formation and oxidation. *Prog. Energy Combust. Sci.,* 23(2):95–132.

Kholghy, M.R. (2012). The Evolution of Soot Morphology in Laminar Co-Flow Diffusion Flames of the Surrogates for Jet A-1 and a Synthetic Kerosene (MSc dissertation). University of Toronto, Toronto, ON, Canada.

Kholghy, M.R., Weingarten, J., and Thomson, M.J. (2015). A study of the effects of the ester moiety on soot formation and species concentrations in a laminar coflow diffusion flame of a surrogate for B100 biodiesel. *Proc. Combust. Inst.,* 35(1):905–912.

Kulkarni, P., Baron, P.A., and Willeke, K. (Eds.) (2011). Aerosol measurement: principles, techniques, and applications. John Wiley & Sons, Hoboken, New Jersey.

Lai, F.S., Friedlander, S.K., Pich, J., and Hidy, G.M. (1972). The self-preserving particle size distribution for Brownian coagulation in the free-molecule regime. *J. Colloid Interface Sci.,* 39(2):395–405.

Lim, S.S., Vos, T., Flaxman, A.D., Danaei, G., Shibuya, K., Adair-Rohani, H., Amann, M., Anderson, H.R., Andrews, K.G., Aryee, M., Atkinson, C., Bacchus, L.J., Bahalim, A.N., Balakrishnan, K., Balmes, J., Barker-Collo, S., Baxter, A., Bell, M.L., Blore, J.D., Blyth, F., Bonner, C., Borges, G., Bourne, R., Boussinesq, M., Brauer, M., Brooks, P., Bruce, N.G., Brunekreef, B., Bryan-Hancock, C., Bucello, C., Buchbinder, R., Bull, F., Burnett, R.T., Byers, T.E., Calabria, B., Carapetis, J., Carnahan, E., Chafe, Z., Charlson, F., Chen, H., Chen, J.S., Cheng, A.T.A., Child, J.C., Cohen, A., Colson, K.E., Cowie, B.C., Darby, S., Darling, S., Davis, A., Degenhardt, L., Dentener, F., Des Jarlais, D.C., Devries, K., Dherani, M., Ding, E.L., Dorsey, E.R., Driscoll, T., Edmond, K., Ali, S.E., Engell, R.E., Erwin, P.J., Fahimi, S., Falder, G., Farzadfar, F., Ferrari, A., Finucane, M.M., Flaxman, S., Fowkes, F.G.R., Freedman, G., Freeman, M.K., Gakidou, E., Ghosh, S., Giovannucci, E., Gmel, G., Graham, K., Grainger, R., Grant, B., Gunnell, D., Gutierrez, H.R., Hall, W., Hoek, H.W., Hogan, A., Hosgood, H.D., Hoy, D., Hu, H., Hubbell, B.J., Hutchings, S.J., Ibeanusi, S.E., Jacklyn, G.L., Jasrasaria, R., Jonas, J.B., Kan, H., Kanis, J.A., Kassebaum, N., Kawakami, N., Khang, Y.H., Khatibzadeh, S., Khoo, J.P., Kok, C., Laden, F., Lalloo, R., Lan, Q., Lathlean, T., Leasher, J.L., Leigh, J., Li, Y., Lin, J.K., Lipshultz, S.E., London, S., Lozano, R., Lu, Y., Mak, J., Malekzadeh, R., Mallinger, L., Marcenes, W., March, L., Marks, R., Martin, R., McGale, P., McGrath, J., Mehta, S., Mensah, G.A., Merriman, T.R., Micha, R., Michaud, C., Mishra, V., Hanafiah, K.M., Mokdad, A.A., Morawska, L., Mozaffarian, D., Murphy, T., Naghavi, M., Neal, B., Nelson, P.K., Nolla, J.M., Norman, R., Olives, C.,

Omer, S.B., Orchard, J., Osborne, R., Ostro, B., Page, A., Pandey, K.D., Parry, C.D.H., Passmore, E., Patra, J., Pearce, N., Pelizzari, P.M., Petzold, M., Phillips, M.R., Pope, D., Pope, C.A., Powles, J., Rao, M., Razavi, H., Rehfuess, E.A., Rehm, J.T., Ritz, B., Rivara, F.P., Roberts, T., Robinson, C., Rodriguez-Portales, J.A., Romieu, I., Room, R., Rosenfeld, L.C., Roy, A., Rushton, L., Salomon, J.A., Sampson, U., Sanchez-Riera, L., Sanman, E., Sapkota, A., Seedat, S., Shi, P., Shield, K., Shivakoti, R., Singh, G.M., Sleet, D.A., Smith, E., Smith, K.R., Stapelberg, N.J.C., Steenland, K., Stöckl, H., Stovner, L.J., Straif, K., Straney, L., Thurston, G.D., Tran, J.H., Van Dingenen, R., Van Donkelaar, A., Veerman, J.L., Vijayakumar, L., Weintraub, R., Weissman, M.M., White, R.A., Whiteford, H., Wiersma, S.T., Wilkinson, J.D., Williams, H.C., Williams, W., Wilson, N., Woolf, A.D., Yip, P., Zielinski, J.M., Lopez, A.D., Murray, C.J.L., and Ezzati, M. (2012). A comparative risk assessment of burden of disease and injury attributable to 67 risk factors and risk factor clusters in 21 regions, 1990-2010: A systematic analysis for the Global Burden of Disease Study 2010. *Lancet,* 380(9859):2224–2260.

Liu, C., Chung, C.E., Yin, Y., and Schnaiter, M. (2018). The absorption Ångström exponent of black carbon: from numerical aspects. *Atmos. Chem. Phys.,* 18(9):6259–6273.

Lyon, A., Keating, C.D., Fox, A.P., Baker, B.E., He, L., Nicewarner, S.R., Mulvaney, S.P., and Natan, M.J. (1998). Raman Spectroscopy. *Anal. Chem.,* 70(12):341–362.

Maricq, M.M. (2012). Soot formation in ethanol/gasoline fuel blend diffusion flames. *Combust. Flame,* 159(1):170–180.

Maricq, M.M. (2011). Physical and chemical comparison of soot in hydrocarbon and biodiesel fuel diffusion flames: A study of model and commercial fuels. *Combust. Flame,*

158(1):105–116.

Maricq, M.M. (2006). A comparison of soot size and charge distributions from ethane, ethylene, acetylene, and benzene/ethylene premixed flames. *Combust. Flame,* 144(4):730–743.

Maricq, M.M., Harris, S.J., and Szente, J.J. (2003). Soot size distributions in rich premixed ethylene flames. *Combust. Flame,* 132(3):328–342.

Maricq, M.M. and Xu, N. (2004). The effective density and fractal dimension of soot particles from premixed flames and motor vehicle exhaust. *J. Aerosol Sci.,* 35(10):1251–1274.

McDonald, J.E. (1962). Visibility Reduction due to Jet-Exhaust Carbon Particles. *J. Appl. Meteorol.,* 1(3):391–398.

Mcelreath, D. (2011). Comparison of Hydraulic Fracturing Fluids Composition with Produced Formation Water following Fracturing – Implications for Fate and Transport*., in Proceedings of the Technical Workshops for the Hydraulic Fracturing Study: Fate and Transport,* pp. 1–33.

McEnally, C.S., Köylü, Ü.Ö., Pfefferle, L.D., and Rosner, D.E. (1997). Soot volume fraction and temperature measurements in laminar nonpremixed flames using thermocouples. *Combust. Flame,* 109(4):701–720.

McEnally, C.S., Pfefferle, L.D., Atakan, B., and Kohse-Höinghaus, K. (2006). Studies of aromatic hydrocarbon formation mechanisms in flames: Progress towards closing the fuel gap. *Prog. Energy Combust. Sci.,* 32(3):247–294.

McEwen, J. (2010). Soot emission factors from lab-scale flares burning solution gas mixtures (MSc dissertation). Carleton University, Ottawa, ON, Canada.

McEwen, J.D.N. and Johnson, M.R. (2012). Black carbon particulate matter emission factors for buoyancy-driven associated gas flares. *J. Air Waste Manage. Assoc.,* 62(3):307–321.

Meakin, P., Donn, B., and Mulholland, G.W. (1989). Collisions between point masses and fractal aggregates. *Langmuir,* 5(2):510–518.

Menon, S., Hansen, J., Nazarenko, L., and Luo, Y. (2002). Climate Effects of Black Carbon Aerosols in China and India. *Science,* 297(5590):2250–2253.

Michelsen, H.A. (2017). Probing soot formation, chemical and physical evolution, and oxidation: A review of in situ diagnostic techniques and needs. *Proc. Combust. Inst.,* 36(1):717–735.

Michelsen, H.A., Schulz, C., Smallwood, G.J., and Will, S. (2015). Laser-induced incandescence: Particulate diagnostics for combustion, atmospheric, and industrial applications. *Prog. Energy Combust. Sci.,* 51:2–48.

Milani, Z.R., Jefferson, A.M., and Johnson, M.R. (2019). Remote Detection of Sodium Signatures as an Indicator of Liquid Carry-Over into Flare Flames in Northa Dakota*., in Proceedings of the Combustion Institute Canadian Section – Spring Technical Meeting,* Kelowna, BC, Canada.

Miller, D.J., Huang, X., Li, H., Kasemset, S., Lee, A., Agnihotri, D., Hayes, T., Paul, D.R., and Freeman, B.D. (2013). Fouling-resistant membranes for the treatment of flowback water from hydraulic shale fracturing: a pilot study. *J. Memb. Sci.,* 437:265–275.

Mitchell, J.B.A. and Miller, D.J.M. (1989). Studies of the effects of metallic and gaseous additives in the control of soot formation in diffusion flames. *Combust. Flame,* 75(1):45–55.

Mitchell, R.E. (1975). Nitrogen oxide formation in laminar methane-air diffusion flames (PhD

dissertation). Massachusetts Institute of Technology, Boston, MA.

Moallemi, A. (2017). Experimental Investigation of the Effect of NaCl Additive on the Formation and Evolution of Particles in a Diffusion Flame (MSc dissertation). University of Alberta, Edmonton, AB, Canada.

Moallemi, A., Kazemimanesh, M., Corbin, J.C., Thomson, K., Smallwood, G., Olfert, J.S., and Lobo, P. (2019). Characterization of black carbon particles generated by a propane-fueled miniature inverted soot generator. *J. Aerosol Sci.,* 135:46–57.

Momenimovahed, A. and Olfert, J.S. (2015). Effective Density and Volatility of Particles Emitted from Gasoline Direct Injection Vehicles and Implications for Particle Mass Measurement. *Aerosol Sci. Technol.,* 49(11):1051–1062.

Müller-Dethlefs, K. and Schlader, A.F. (1976). The effect of steam on flame temperature, burning velocity and carbon formation in hydrocarbon flames. *Combust. Flame,* 27:205–215.

Myhre, G., Shindell, D., Bréon, F.-M., Collins, W.D., Fuglestvedt, J., Huang, J., Koch, D., Lamarque, J.-F., Lee, D., Mendoza, B., Nakajima, T., Robock, a., Stephens, G., Takemura, T., and Zhan, H. (2013). IPCC AR5 (2013) Chapter 8: Anthropogenic and Natural Radiative Forcing*., in Climate Change 2013: The Physical Science Basis. Contribution of Working Group I to the Fifth Assessment Report of the Intergovernmental Panel on Climate Change,* pp. 659–740.

Nanda, K.K. (2005). Bulk cohesive energy and surface tension from the size-dependent evaporation study of nanoparticles. *Appl. Phys. Lett.,* 87(2):21909.

Neoh, K.G., Howard, J.B., and Sarofim, A.F. (1981). Soot Oxidation in Flames., *in Particulate Carbon,* Springer US, Boston, MA, pp. 261–282.

Nguyen, H. V. and Flagan, R.C. (1993). The mobility and structure of aerosol agglomerates. *Aerosol Sci. Technol.,* 18(1):25–47.

Olfert, J. and Rogak, S. (2019). Universal relations between soot effective density and primary particle size for common combustion sources. *Aerosol Sci. Technol.,* 53(5):485–492.

Olfert, J.S. and Collings, N. (2005). New method for particle mass classification—the Couette centrifugal particle mass analyzer. *J. Aerosol Sci.,* 36(11):1338–1352.

Paktinat, J., O'Neil, B.J., and Tulissi, M.G. (2011). Case studies: impact of high salt tolerant friction reducers on freshwater conversation in Canadian shale fracturing treatments., *in Canadian Unconventional Resources Conference,* Society of Petroleum Engineers, Calgary, AB, Canada.

Park, J.H., Mudunkotuwa, I.A., Mines, L.W.D., Anthony, T.R., Grassian, V.H., and Peters, T.M. (2015). A Granular Bed for Use in a Nanoparticle Respiratory Deposition Sampler. *Aerosol Sci. Technol.,* 49(3):179–187.

Patel, M., Azanza Ricardo, C.L., Scardi, P., and Aswath, P.B. (2012). Morphology, structure and chemistry of extracted diesel soot—Part I: Transmission electron microscopy, Raman spectroscopy, X-ray photoelectron spectroscopy and synchrotron X-ray diffraction study. *Tribol. Int.,* 52:29–39.

Paulik, L.B., Donald, C.E., Smith, B.W., Tidwell, L.G., Hobbie, K.A., Kincl, L., Haynes, E.N., and Anderson, K.A. (2015). Impact of Natural Gas Extraction on PAH Levels in Ambient

Air. *Environ. Sci. Technol.,* 49(8):5203–5210.

Petzold, A. and Niessner, R. (1996). Photoacoustic soot sensor for in-situ black carbon monitoring. *Appl. Phys. B Laser Opt.,* 63(2):191–197.

Pratsinis, S.E. (1998). Flame aerosol synthesis of ceramic powders. *Prog. Energy Combust. Sci.,* 24(3):197–219.

Puri, R., Richardson, T.F., Santoro, R.J., and Dobbins, R.A. (1993). Aerosol dynamic processes of soot aggregates in a laminar ethene diffusion flame. *Combust. Flame,* 92(3):320–333.

Puri, R., Santoro, R.J., and Smyth, K.C. (1994). The oxidation of soot and carbon monoxide in hydrocarbon diffusion flames. *Combust. Flame,* 97(2):125–144.

Quay, B., Lee, T.-W., Ni, T., and Santoro, R.J. (1994). Spatially resolved measurements of soot volume fraction using laser-induced incandescence. *Combust. Flame,* 97(3–4):384–392.

Radney, J.G., You, R., Ma, X., Conny, J.M., Zachariah, M.R., Hodges, J.T., and Zangmeister, C.D. (2014). Dependence of Soot Optical Properties on Particle Morphology: Measurements and Model Comparisons. *Environ. Sci. Technol.,* 48(6):3169–3176.

Raj, A., Sander, M., Janardhanan, V., and Kraft, M. (2010). A study on the coagulation of polycyclic aromatic hydrocarbon clusters to determine their collision efficiency. *Combust. Flame,* 157(3):523–534.

Ramanathan, V. and Carmichael, G. (2008). Global and regional climate changes due to black carbon. *Nat. Geosci.,* 1(4):221–227.

Richter, H. and Howard, J.. (2000). Formation of polycyclic aromatic hydrocarbons and their

growth to soot—a review of chemical reaction pathways. *Prog. Energy Combust. Sci.,* 26(4–6):565–608.

Rogak, S.N., Flagan, R.C., and Nguyen, H. V. (1993). The Mobility and Structure of Aerosol Agglomerates. *Aerosol Sci. Technol.,* 18(1):25–47.

Roth, P., Brandt, O., and Von Gersum, S. (1991). High temperature oxidation of suspended soot particles verified by CO and CO2 measurements. *Symp. (Int.) Combust.,* 23(1):1485–1491.

Russo, C., Apicella, B., Lighty, J.S., Ciajolo, A., and Tregrossi, A. (2017). Optical properties of organic carbon and soot produced in an inverse diffusion flame. *Carbon,* 124:372–379.

Russo, C., Tregrossi, A., and Ciajolo, A. (2015). Dehydrogenation and growth of soot in premixed flames. *Proc. Combust. Inst.,* 35(2):1803–1809.

Sadezky, A., Muckenhuber, H., Grothe, H., Niessner, R., and Pöschl, U. (2005). Raman microspectroscopy of soot and related carbonaceous materials: Spectral analysis and structural information. *Carbon,* 43(8):1731–1742.

Saffaripour, M., Tay, L.-L., Thomson, K.A., Smallwood, G.J., Brem, B.T., Durdina, L., and Johnson, M. (2017). Raman spectroscopy and TEM characterization of solid particulate matter emitted from soot generators and aircraft turbine engines. *Aerosol Sci. Technol.,* 51(4):518–531.

Saffaripour, M., Zabeti, P., Kholghy, M., and Thomson, M.J. (2011). An Experimental Comparison of the Sooting Behavior of Synthetic Jet Fuels. *Energy & Fuels,* 25(12):5584–5593.

Samson, R.J., Mulholland, G.W., and Gentry, J.W. (1987). Structural analysis of soot

agglomerates. *Langmuir,* 3(2):272–281.

Santoro, R.J., Semerjian, H.G., and Dobbins, R.A. (1983). Soot particle measurements in diffusion flames. *Combust. Flame,* 51:203–218.

Santoro, R.J., Yeh, T.T., Horvath, J.J., and Semerjian, H.G. (1987). The Transport and Growth of Soot Particles in Laminar Diffusion Flames. *Combust. Sci. Technol.,* 53(2–3):89–115.

Scarnato, B. V., Vahidinia, S., Richard, D.T., and Kirchstetter, T.W. (2013). Effects of internal mixing and aggregate morphology on optical properties of black carbon using a discrete dipole approximation model. *Atmos. Chem. Phys.,* 13(10):5089–5101.

Schnaiter, M., Horvath, H., Möhler, O., Naumann, K.-H., Saathoff, H., and Schöck, O.W. (2003). UV-VIS-NIR spectral optical properties of soot and soot-containing aerosols. *J. Aerosol Sci.,* 34(10):1421–1444.

Schulz, C., Kock, B.F., Hofmann, M., Michelsen, H., Will, S., Bougie, B., Suntz, R., and Smallwood, G. (2006). Laser-induced incandescence: recent trends and current questions. *Appl. Phys. B,* 83(3):333–354.

Schwarz, J.P., Holloway, J.S., Katich, J.M., McKeen, S., Kort, E.A., Smith, M.L., Ryerson, T.B., Sweeney, C., and Peischl, J. (2015). Black Carbon Emissions from the Bakken Oil and Gas Development Region. *Environ. Sci. Technol. Lett.,* 2(10):281–285.

Sgro, L.A., Barone, A.C., Commodo, M., D'Alessio, A., De Filippo, A., Lanzuolo, G., and Minutolo, P. (2009). Measurement of nanoparticles of organic carbon in non-sooting flame conditions. *Proc. Combust. Inst.,* 32 I(1):689–696.

Shaddix, C.R. (1999). Correcting thermocouple measurements for radiation loss: a critical

review., *in Proceedings of the 33rd National Heat Transfer Conference,* Albuquerque, NM.

Shaddix, C.R. and Smyth, K.C. (1996). Laser-induced incandescence measurements of soot production in steady and flickering methane, propane, and ethylene diffusion flames. *Combust. Flame,* 107(4):418–452.

Simonsson, J., Olofsson, N.E., Bladh, H., Sanati, M., and Bengtsson, P.E. (2017). Influence of potassium and iron chloride on the early stages of soot formation studied using imaging LII/ELS and TEM techniques. *Proc. Combust. Inst.,* 36(1):853–860.

Slack, M., Cox, J.W., Grillo, A., Ryan, R., and Smith, O. (1989). Potassium kinetics in heavily seeded atmospheric pressure laminar methane flames. *Combust. Flame,* 77(3–4):311–320.

Slavinskaya, N.A., Riedel, U., Dworkin, S.B., and Thomson, M.J. (2012). Detailed numerical modeling of PAH formation and growth in non-premixed ethylene and ethane flames. *Combust. Flame,* 159(3):979–995.

Smooke, M.D., Long, M.B., Connelly, B.C., Colket, M.B., and Hall, R.J. (2005). Soot formation in laminar diffusion flames. *Combust. Flame,* 143(4):613–628.

Smyth, K.C., Miller, J.H., Dorfman, R.C., Mallard, W.G., and Santoro, R.J. (1985). Soot inception in a methane/air diffusion flame as characterized by detailed species profiles. *Combust. Flame,* 62(2):157–181.

Sonibare, J.A., Adebiyi, F.M., Obanijesu, E.O., and Okelana, O.A. (2010). Air quality index pattern around petroleum production facilities. *Manag. Environ. Qual. An Int. J.,* 21(3):379–392.

Sorensen, C.M. (2011). The Mobility of Fractal Aggregates: A Review. *Aerosol Sci. Technol.,*

45(7):765–779.

Stohl, A., Klimont, Z., Eckhardt, S., Kupiainen, K., Shevchenko, V.P., Kopeikin, V.M., and Novigatsky, A.N. (2013). Black carbon in the Arctic: the underestimated role of gas flaring and residential combustion emissions. *Atmos. Chem. Phys.,* 13(17):8833–8855.

Strosher, M.T. (2000). Characterization of emissions from diffusion flare systems. *J. Air Waste Manage. Assoc.,* 50(10):1723–1733.

Sun, J. and Simon, S.L. (2007). The melting behavior of aluminum nanoparticles. *Thermochim. Acta,* 463(1–2):32–40.

Swarthout, R.F., Russo, R.S., Zhou, Y., Miller, B.M., Mitchell, B., Horsman, E., Lipsky, E., McCabe, D.C., Baum, E., and Sive, B.C. (2015). Impact of Marcellus Shale Natural Gas Development in Southwest Pennsylvania on Volatile Organic Compound Emissions and Regional Air Quality. *Environ. Sci. Technol.,* 49(5):3175–3184.

Tappe, M., Haynes, B.S., and Kent, J.H. (1993). The effect of alkali metals on a laminar ethylene diffusion flame. *Combust. Flame,* 92(3):266–273.

Tyner, D.R. and Johnson, M.R. (2014). Emission Factors for Hydraulically Fractured Gas Wells Derived Using Well- and Battery-level Reported Data for Alberta, Canada. *Environ. Sci. Technol.,* 48(24):14772–14781.

U.S. Energy Information Administration (2018). Natural Gas Gross Withdrawals and Production. Available at https://www.eia.gov/dnav/ng/ng_prod_sum_a_EPG0_VGV_mmcf_a.htm (Accessed 30 July 2019).

URS Corporation (2011). Water-related issues associated with gas production in the Marcellus

shale. Fort Washington, PA. Available at https://www.nyserda.ny.gov/-/media/Files/Publications/PPSER/NYSERDA/ng/URS-Report-2011-Mar.pdf

Vander Wal, R.L., Bryg, V.M., and Huang, C.-H. (2014). Aircraft engine particulate matter: Macro- micro- and nanostructure by HRTEM and chemistry by XPS. *Combust. Flame,* 161(2):602–611.

Vander Wal, R.L., Yezerets, A., Currier, N.W., Kim, D.H., and Wang, C.M. (2007). HRTEM Study of diesel soot collected from diesel particulate filters. *Carbon,* 45(1):70–77.

Vengosh, A., Jackson, R.B., Warner, N., Darrah, T.H., and Kondash, A. (2014). A critical review of the risks to water resources from unconventional shale gas development and hydraulic fracturing in the United States. *Environ. Sci. Technol.,* 48(15):8334–8348.

Wang, H. (2011). Formation of nascent soot and other condensed-phase materials in flames. *Proc. Combust. Inst.,* 33(1):41–67.

Wang, Z., King, S.M., Freney, E., Rosenoern, T., Smith, M.L., Chen, Q., Kuwata, M., Lewis, E.R., Pöschl, U., Wang, W., Buseck, P.R., and Martin, S.T. (2010). The Dynamic Shape Factor of Sodium Chloride Nanoparticles as Regulated by Drying Rate. *Aerosol Sci. Technol.,* 44(11):939–953.

Warner, N.R., Darrah, T.H., Jackson, R.B., Millot, R., Kloppmann, W., and Vengosh, A. (2014). New Tracers Identify Hydraulic Fracturing Fluids and Accidental Releases from Oil and Gas Operations. *Environ. Sci. Technol.,* 48(21):12552–12560.

Wasylishen, R. and Fulton, S. (2012). Reuse of Flowback and Produced Water for Hydraulic Fracturing in Tight Oil. Calgary, AB, Canada. Available at https://auprf.ptac.org/wp-

content/uploads/2015/11/reuse-of-flowback-produced-water-for-hydraulic-fracturing-1.pdf

Wersborg, B.L., Yeung, A.C., and Howard, J.B. (1975). Concentration and mass distribution of charged species in sooting flames. *Symp. (Int.) Combust.,* 15(1):1439–1448.

Weyant, C.L., Shepson, P.B., Subramanian, R., Cambaliza, M.O.L., Heimburger, A., McCabe, D., Baum, E., Stirm, B.H., and Bond, T.C. (2016). Black Carbon Emissions from Associated Natural Gas Flaring. *Environ. Sci. Technol.,* 50(4):2075–2081.

Whitaker, S. (1972). Forced Convection Heat Transfer Correlations for Flow In Pipes, Past Flat Plates, Single. *AIChE J.,* 18(2):361–371.

Wieschnowsky, U., Bockhorn, H., and Fetting, F. (1989). Some new observations concerning the mass growth of soot in premixed hydrocarbon-oxygen flames. *Symp. (Int.) Combust.,* 22(1):343–352.

Wocken, C.A., Stevens, B.G., Almlie, J.C., and Schlasner, S.M. (2013). End-Use Technology Study-An Assessment of Alternative Uses for Associated Gas. Bismarck, ND. Available at https://undeerc.org/Bakken/pdfs/CW_Tech_Study_April-2013.pdf

Wronski, C.R.M. (1967). The size dependence of the melting point of small particles of tin. *Br. J. Appl. Phys.,* 18(12):1731–1737.

Xue, H., Khalizov, A.F., Wang, L., Zheng, J., and Zhang, R. (2009). Effects of Coating of Dicarboxylic Acids on the Mass−Mobility Relationship of Soot Particles. *Environ. Sci. Technol.,* 43(8):2787–2792.

Zhang, M., Efremov, M.Y., Schiettekatte, F., Olson, E.A., Kwan, A.T., Lai, S.L., Wisleder, T., Greene, J.E., and Allen, L.H. (2000). Size-dependent melting point depression of

nanostructures: Nanocalorimetric measurements. *Phys. Rev. B - Condens. Matter Mater. Phys.,* 62(15):10548–10557.

Zhang, R., Khalizov, A.F., Pagels, J., Zhang, D., Xue, H., and McMurry, P.H. (2008). Variability in morphology, hygroscopicity, and optical properties of soot aerosols during atmospheric processing. *Proc. Natl. Acad. Sci. U. S. A.,* 105(30):10291–6.

Zhao, B., Uchikawa, K., and Wang, H. (2007). A comparative study of nanoparticles in premixed flames by scanning mobility particle sizer, small angle neutron scattering, and transmission electron microscopy. *Proc. Combust. Inst.,* 31(1):851–860.

Zhao, B., Yang, Z., Li, Z., Johnston, M. V, and Wang, H. (2005). Particle size distribution function of incipient soot in laminar premixed ethylene flames: effect of flame temperature. *Proc. Combust. Inst.,* 30(1):1441–1448.

Zhao, B., Yang, Z., Wang, J., Johnston, M. V., and Wang, H. (2003). Analysis of Soot Nanoparticles in a Laminar Premixed Ethylene Flame by Scanning Mobility Particle Sizer. *Aerosol Sci. Technol.,* 37(8):611–620.

Ziegler, J.G. and Nichols, N.B. (1942). Optimum settings for automatic controllers. *Trans. ASME,* 64(11):759–765.

Ziemkiewicz, P.F. and He, Y.T. (2015). Evolution of water chemistry during Marcellus Shale gas development: A case study in West Virginia. *Chemosphere,* 134:224–231.

Zuberi, B., Johnson, K.S., Aleks, G.K., Molina, L.T., Molina, M.J., and Laskin, A. (2005). Hydrophilic properties of aged soot. *Geophys. Res. Lett.,* 32(1):L01807.

Appendix A

Estimation of sample residence time and particle coagulation in the high dilution sampling system

In addition to the practical criterion outlined in Section 2.3.1 for eliminating the effect of particle-particle coagulation in the high dilution sampling system, it is worthwhile to have an estimation of coagulation theoretically. The first step is to determine the sample flow velocity and sample residence time in different sections of the dilution system. Let us consider a common case where the dilution ratio was ~10,000. Dilution ratio, in its general definition, is equal to the molar rate of diluting gas (nitrogen) divided by the molar rate of sample gas. Using the ideal gas law, dilution ratio, *DR*, at the sampling pinhole is

$$DR = \frac{\dot{n}_{\mathrm{DG}}}{\dot{n}_{\mathrm{s}}} = \frac{\frac{P_{\mathrm{DG}}\dot{V}_{\mathrm{DG}}}{RT_{\mathrm{DG}}}}{\frac{P_{\mathrm{s}}\dot{V}_{\mathrm{s}}}{RT_{\mathrm{s}}}}, \tag{A.1}$$

where *R* is the universal gas constant and subscripts "DG" and "s" stand for diluting gas and sample gas, respectively. Simplifying Eq. (A.1) yields

$$\dot{V}_{\mathrm{s}} = \frac{\dot{V}_{\mathrm{DG}}}{DR}\left(\frac{P_{\mathrm{DG}}}{P_{\mathrm{s}}}\right)\left(\frac{T_{\mathrm{s}}}{T_{\mathrm{DG}}}\right). \tag{A.2}$$

The volumetric flow rate of diluting gas and dilution ratio across the pinhole are known and equal to 19,300 cm^3/min and ~10,000, respectively. We can assume that $P_{\mathrm{DG}} \approx P_{\mathrm{s}}$ because the pressure drop across the pinhole is tiny (250–500 Pa). It is also assumed that the temperature of sample gas

inside the pinhole is approximately the same as flame temperature in the immediate vicinity of the pinhole, which was in the range of 1200–1500 K based on the Figure 3.3. The temperature of diluting nitrogen was ~300 K and, therefore, the temperature ratio in Eq. (A.2) is ~4–5. Thus, the volumetric flow rate of sample gas through the pinhole is calculated using Eq. (A.2) to be ~0.13–0.16 cm^3/s.

Flow velocity of sample gas traversing the pinhole was obtained by dividing the volumetric flow rate of sample gas by the cross-sectional area of the clean pinhole with a diameter of 0.2 mm. Sample gas velocity through the pinhole was calculated to be ~4–5 m/s. The residence time of sample gas traversing the pinhole is the length of the pinhole (125 μm) divided by the sample gas velocity. Therefore, the residence time through the pinhole was ~30–50 μs. Sample flow velocity and residence time through other sections of the sampling system was calculated using a similar method outlined above and the numbers are reported in section 2.2.4.

Coagulation of nanoparticles in the sample was estimated using the average coagulation coefficient for a polydisperse aerosol (Hinds 1999, pp. 269–271) for various lognormal size distributions measured by the SMPS. The calculated average coagulation coefficient was in the range of 7.2×10^{-10} cm^3/s to 19.6×10^{-10} cm^3/s. The extent of particles undergoing coagulation can be estimated from

$$\frac{N_{\text{coagulated}}(t)}{N_{\text{total}}} = \frac{N_{\text{total}}\bar{K}t}{1 + N_{\text{total}}\bar{K}t} \tag{A.3}$$

where N is the particle number concentration, $\bar{K}$ is the average coagulation coefficient, and t is the residence time (Hinds 1999, p. 263). The residence time for particles in the sampling probe from

the pinhole to the extraction branch for the particle measurement suite was ~2.1 ms. The maximum concentration of particles in the sampling probe after being diluted in the pinhole was ~3×10^{7} cm^{-3}.

Considering the maximum coagulation coefficient of 19.6×10^{-10} cm^{3}/s, the percentage of particles undergoing coagulation in the probe was always below 0.01%. The residence time from the extraction branch in the sampling probe to the particle measurement suite was ~0.78 s and the coagulation of particles was always less than ~4.4% during transport to the particle measurement suite.

Appendix B

Flame Temperature Measurement

As mentioned earlier, the temperature of the flame was measured at various radial and axial locations in the reacting flow. The thermocouple was inserted swiftly in different regions of the reacting flow and once the thermocouple junction reached the desired location in the flame as indicated by a stopper at the end of the rail, a switch was triggered and the data acquisition started. The sampling was done for a period of about two seconds with a sampling rate of 100 Hz. This technique of flame temperature measurement is known as the rapid thermocouple insertion technique (McEnally *et al.* 1997). Long exposure (more than 7 seconds) of the thermocouple wire inside the flame resulted in its rupture. Additionally, the soot deposition on the thermocouple junction changes its emissivity and results in a gradual drop in the measured temperature.

Figure B.1 shows temperature measurements in regions of the flow where high and low concentrations of soot particles exist. In locations with low soot concentration, the data showed a swift increase in temperature followed by a plateau as the steady-state response. In locations with high soot concentration, the temperature profile showed a swift increase in temperature followed by a peak and then a significant decrease in the measured temperature. These trends were also observed in several other studies (McEnally *et al.* 1997; Abid 2009; Kholghy 2012). McEnally *et al.* (1997) stated that the temperature profile obtained by the rapid thermocouple insertion technique has several stages. The first stage is the transient response which starts from the moment

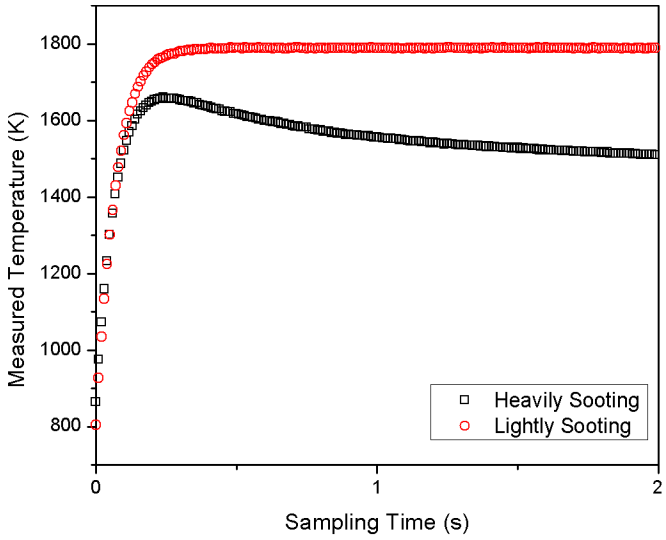

Figure B.1: Effect of soot deposition on the thermocouple junction on flame temperature profile.

sampling commences until it reaches either a steady-state plateau or a peak. For lightly sooting locations, the temperature measured after the transient response is more-or-less constant, known as the steady-state stage. For heavily sooting locations, the next stages after the transient response are the variable emissivity and variable diameter stages, where a decrease in temperature occurs. The representative temperature for each location in the reacting flow depends on whether the desired location is highly sooting or not. Kholghy (Kholghy 2012) considered the magnitude of the steady-state plateau section of the temperature profile as the representative temperature in lightly sooting regions and the magnitude of peak as the representative temperature in heavily sooting regions.

To determine if the thermocouple was in a highly sooting or lightly sooting region, the measured temperature profile from $t = 0.75$ s (after the transient response) to $t = 2$ s was fitted by a first order polynomial. It was assumed that if the polynomial fit has a slope larger than -20 K/s, the measured temperature was for a highly sooting region and the maximum measured temperature was considered as the thermocouple junction temperature.

For lightly sooting regions, the thermocouple junction temperature was assumed to be the average of measured temperature from 5τ to 7τ, where τ is the time constant assuming the measured temperature during the sampling time is the step response function of a first order time-variant system that can be approximated as

$$T = A\left(1 - e^{-\frac{t}{\tau}}\right) + B \tag{B.1}$$

where B is the value of temperature measured by the thermocouple at t = 0 s. Coefficient A was obtained by fitting the temperature data points with the function in Eq. (B.1). The time constant of the thermocouple determined from Eq. (B.1) was between 0.1–0.25 s, which was similar to the time constant reported by McEnally *et al.* (1997).

The gas (flow) temperature was obtained by correcting the thermocouple junction temperature for heat losses. Equation (B.2) is the energy balance equation for the thermocouple junction, as suggested by Shaddix (1999):

$$\dot{Q}_{\text{rad}} + \dot{Q}_{\text{conv}} + \dot{Q}_{\text{cond}} + \dot{Q}_{\text{cat}} = \rho_{\text{th}} c_p V_{\text{th}} \frac{\mathrm{d}T_{\text{th}}}{\mathrm{d}t} \tag{B.2}$$

where $\dot{Q}_{\text{rad}}$ is the radiation heat transfer, $\dot{Q}_{\text{conv}}$ is the convective heat transfer, $\dot{Q}_{\text{cond}}$ is the conductive heat transfer, and $\dot{Q}_{\text{cat}}$ is the heat transfer due to catalytic reactions. T_{th} is the thermocouple temperature, c_p is the specific heat capacity of the thermocouple, and ρ_{th} and V_{th} are the density and volume of the thermocouple, respectively.

Conductive heat loss occurs in the thermocouple due to the conductive heat transfer from the junction to the wire. Heitor and Moreira (1993) have suggested that the conductive heat loss is insignificant if the length to diameter ratio of thermocouple is more than 200, which was the case in this study and the conductive heat loss was considered to be negligible.

The catalytic reactions could occur due to radical recombination at the surface of the thermocouple junction (Shaddix 1999). Characterizing the effect of catalysis on thermocouple measurements is a relatively difficult task. Coating the surface of the thermocouple with a non-reactive material, such as silica, can mitigate the effect of catalytic reactions (Katsuki *et al.* 1987; Abid 2009). However, catalytic heat loss is more significant in unreacted regions of premixed flames (Shaddix 1999) and some studies that did not apply coating on the thermocouple surface (Ballantyne and Moss 1977; McEnally *et al.* 1997; Saffaripour *et al.* 2011; Kholghy *et al.* 2015). Ballantyne and Moss (Ballantyne and Moss 1977) measured the temperature of a turbulent methane diffusion flame and claimed that the catalytic heat loss would contribute about 20 K in temperature measurements. McEnally *et al.* (1997) used an uncoated R-type thermocouple to measure the temperature of a laminar methane diffusion flame and reported that the catalysis effect was negligible in diffusion fames.

By neglecting the heat losses due to conduction and catalytic reactions and considering steady-state condition, Eq. (B.2) becomes

$$\dot{Q}_{\mathrm{rad}} + \dot{Q}_{\mathrm{conv}} = 0 \tag{B.3}$$

For the radiative heat loss in this study, it was assumed that the thermocouple has a gray emitting surface and is surrounded by an isothermal diffuse-gray wall (Shaddix 1999). Additionally, the surface area of the wall is much greater than the surface area of the thermocouple. With these assumptions Eq. (B.3) becomes

$$\varepsilon\sigma A\left(T_{\mathrm{th}}^4 - T_{\mathrm{w}}^4\right) - Ah\left(T_{\mathrm{g}} - T_{\mathrm{th}}\right) = 0 \tag{B.4}$$

where ε is the emissivity, σ is the Boltzmann constant, A is the heat transfer surface area, h is the convective heat transfer coefficient, and T_w and T_g are the wall and gas (flow) temperatures, respectively.

By rearranging Eq. (B.4), the gas temperature is

$$T_g = T_{th} + \frac{\varepsilon\sigma}{h}\left(T_{th}^4 - T_w^4\right) \tag{B.5}$$

Rewriting Eq. (B.5) based on the Nusselt number (Nu) gives

$$T_g = T_{th} + \frac{\varepsilon\sigma}{Nu}\left(T_{th}^4 - T_w^4\right)\frac{d}{k} \tag{B.6}$$

where d is the thermocouple junction diameter and k is the thermal conductivity of the gas.

The convective heat transfer was corrected for based on empirical correlations for the Nusselt number. In the current study, the thermocouple junction had a spherical geometry and, for forced convection around a sphere, Whitaker correlation (Whitaker 1972) was used to obtain the Nusselt number as follows

$$Nu = 2 + (0.4Re^{\frac{1}{2}} + 0.06Re^{\frac{2}{3}})Pr^{0.4}(\frac{\mu_g}{\mu_j}) \tag{B.7}$$

where Re is the Reynolds Number, Pr is the Prandtl number, and μ_g and μ_j are the viscosity of the gas and the thermocouple junction, respectively. Substituting Eq. (B.7) into Eq. (B.6) gives the following equation for gas temperature:

$$T_g = T_{th} + \frac{\varepsilon\sigma}{2 + (0.4Re^{\frac{1}{2}} + 0.06Re^{\frac{2}{3}})Pr^{0.4}(\frac{\mu_g}{\mu_j})}\left(T_{th}^4 - T_w^4\right)\frac{d}{k}. \tag{B.8}$$

The thermocouple junction diameter was 190±37 μm based on the specifications from the supplier. In Eq. (B.8), Re, Pr, and k are functions of gas composition and temperature and, to derive these

parameters, the gas composition of reacting flow must be known. The gas composition and the velocity of the flow were obtained from a previous study on a similar burner geometry and fuel flow condition (Mitchell 1975). For simplicity, the approximated gas composition consisted of only six species: CO_2, H_2O, CO, H_2, CH_4, and N_2. Viscosity, density, and thermal conductivity of the flow were calculated using Cantera software (Goodwin *et al.* 2016) based on the approximate gas composition. The value of the emissivity in Eq. (B.8) is also temperature dependent. Previous studies (McEnally *et al.* 1997; Saffaripour *et al.* 2011; Kholghy 2012) have used the emissivity values reported by Bradley and Entwistle (1961) for type-S thermocouple (Pt and Pt/10% Rh alloy), which was also used in this study.

Appendix C

Mass Concentration of Input NaCl Particles into the Small-scale Laminar Flame

To estimate the mass concentration of NaCl particles injected into the fuel flow, first the particle size distribution of NaCl particles at the outlet of the burner tube was measured using a scanning mobility particle sizer (SMPS). Figure C.1 shows the PSDs of four SMPS scans of NaCl samples extracted from the burner tube.

Secondly, the mass-mobility relationship of the NaCl particles was determined. To obtain the mass-mobility relationship, a tandem arrangement of a differential mobility analyzer (DMA), a centrifugal particle mass analyzer (CPMA, Cambustion Ltd.), and a condensation particle counter (CPC) was used as shown in Figure C.2. Using the DMA, particles with selected mobility diameter

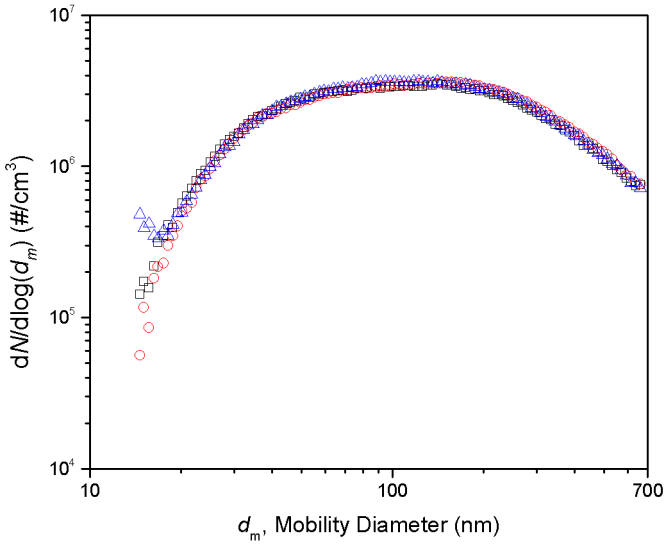

Figure C.1: Size distribution of NaCl particles at the outlet of the burner tube.

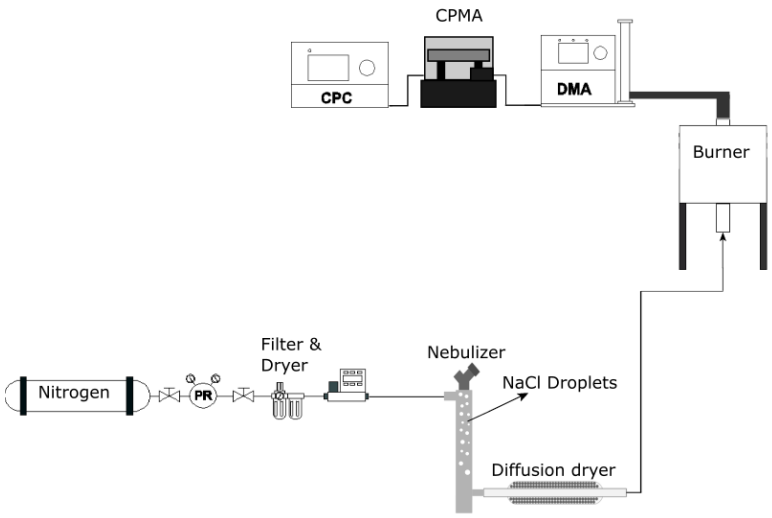

Figure C.2: Scheme of the experimental setup used for obtaining mass-mobility relation.

were directed to the CPMA to measure their corresponding mass. Figure C.3 shows the mass of NaCl particles as a function of their mobility diameter. The mass-mobility relationship of NaCl particles was found as

$$m = 8.79 \times 10^{-7} d_{\mathrm{m}}^{3.02} \tag{C.1}$$

where m has a unit of fg (femtogram) and d_{m} has a unit of nm.

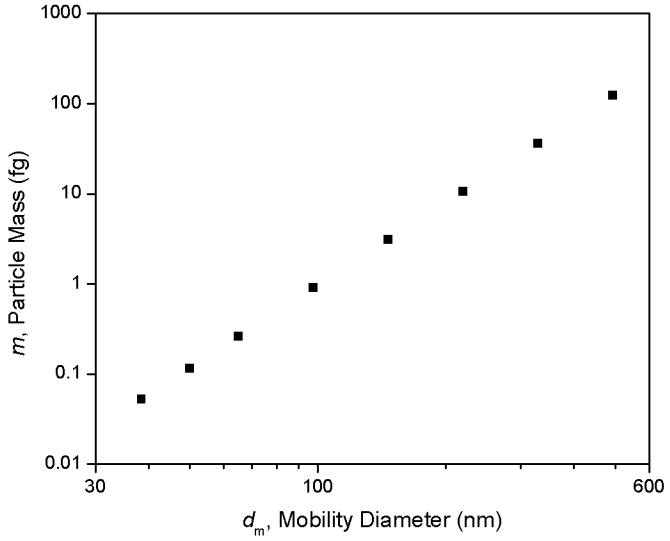

Figure C.3: Mass of NaCl particles as a function of their mobility diameter.

Finally, the size distribution of the NaCl particles was fitted with a log-normal distribution and the mass concentration of NaCl particles was obtained as follows:

$$M_{\mathrm{NaCl}} = \int_0^{1000} \left(\frac{dN}{d \log d_{\mathrm{m}}} \right) m(d_{\mathrm{m}}) d \log d_{\mathrm{m}} \tag{C.2}$$

The mass concentration of NaCl particles based on Eq. (14) was ~45 ng/cm^3.

Appendix D

Uncertainty Analysis for Mass-specific Absorption Coefficient and Single-Scattering Albedo

An uncertainty analysis of the reported mass-specific absorption coefficient (MAC) and single-scattering albedo (SSA) in Chapter 4 was conducted based on ANSI/ASME Measurement Uncertainty Standard (Abernethy *et al.* 1985). According to this standard, total uncertainty of a measurement consists of contributions from "bias" uncertainty (also known as systematic or instrument error) and "precision" uncertainty (also known as repeatability uncertainty). The total uncertainty is the square-root of the bias uncertainty and precision uncertainty squared. The bias uncertainty is the error of the instrument to read the correct value of a measurement. The precision uncertainty represents the scatter in repeated measurements of a quantity. For MAC and SSA measurements, each test was repeated three times for methane-only and methane-NaCl flame.

To estimate the uncertainty in MAC, we first need to calculate the uncertainty in the measured absorption coefficient (B_{abs}) and the mass concentration of elemental carbon (EC) according to the definition of MAC:

$$MAC = \frac{\text{Absorption coefficient}}{\text{EC mass concentration}} \tag{D.1}$$

The bias uncertainty in absorption and scattering coefficients was ±9.6% and ±7.0%, respectively, based on the repeatability of three independent calibrations performed over two months. The precision uncertainty was evaluated based on Student's t-table for a confidence level of 95% and

a degree of freedom of 2 (*i.e.*, number of repeats minus one). The evaluated precision uncertainty, average bias uncertainty, and total uncertainty in absorption coefficient are shown in Table D.1. Similarly, the precision uncertainty, average bias uncertainty, and total uncertainty in scattering coefficient are shown in Table D.2.

Table D.1: Absorption coefficient and its precision uncertainty, average bias uncertainty, and total uncertainty for methane-only and methane-NaCl flames

Flame condition	Test	B_{abs} (Mm^{-1})	Average B_{abs} (Mm^{-1})	Precision uncertainty	Average Bias uncertainty	Total uncertainty
Methane-only	Test 1	24695	25471	1283	2445	2762
	Test 2	25668				
	Test 3	26050				
Methane-NaCl	Test 1	78932	79133	348	7596	7605
	Test 2	79308				
	Test 3	79158				

Table D.2: Scattering coefficient and its precision uncertainty, average bias uncertainty, and total uncertainty for methane-only and methane-NaCl flames

Flame condition	Test	B_{scat} (Mm^{-1})	Average B_{scat} (Mm^{-1})	Precision uncertainty	Average Bias uncertainty	Total uncertainty
Methane-only	Test 1	865	901	61	62	87
	Test 2	911				
	Test 3	929				
Methane-NaCl	Test 1	4207	4205	19	290	291
	Test 2	4214				
	Test 3	4194				

The bias uncertainty in the EC measurement, B_m, was estimated according to the specification of Sunset Lab EC-OC analyzer as follows

$$B_m = 0.1\ \frac{\mu g}{cm^2} + 0.05 m_{EC} \tag{D.2}$$

where mass of EC, m_{EC}, was in units of $\mu g/cm^2$. The uncertainty in the mass of EC was converted to the uncertainty in mass concentration (in units of $\mu g/m^3$) by using the total sampled volume

(sampling flow rate × sampling time) and the stain area on the filter. The precision uncertainty was estimated based on the three measurement repeats for a confidence level of 95%. The total uncertainty in the EC mass concentration was calculated by propagation of bias and precision uncertainties. The evaluated precision uncertainty, average bias uncertainty, and total uncertainty in the mass concentration of EC are shown in Table D.3.

Table D.3: Mass concentration of elemental carbon (EC) and its precision uncertainty, average bias uncertainty, and total uncertainty for methane-only and methane-NaCl flames

Flame condition	Test	EC mass concentration ($\mu g/m^3$)	Average EC concentration ($\mu g/m^3$)	Precision uncertainty	Average Bias uncertainty	Total uncertainty
Methane-only	Test 1	4274	4498	431	261	504
	Test 2	4477				
	Test 3	4743				
Methane-NaCl	Test 1	13527	13592	754	139	767
	Test 2	13574				
	Test 3	13675				

The relative uncertainty in MAC was calculated based on the propagation of uncertainties in the absorption coefficient and the mass concentration of EC as follows:

$$\frac{\varepsilon_{MAC}}{MAC} = \sqrt{\left(\frac{\varepsilon_{B_{\text{abs}}}}{B_{\text{abs}}}\right)^2 + \left(\frac{\varepsilon_{m_{\text{EC}}}}{m_{\text{EC}}}\right)^2} \tag{D.3}$$

where ε indicates the absolute uncertainty in each quantity. The relative uncertainty in absorption coefficient and EC concentration was 10.8% and 11.2%, respectively, in the case of methane-only flame. These values were 9.6% and 5.6%, respectively, in the case of methane-NaCl flame. Table D.4 shows the total uncertainty in MAC for methane-only and methane-NaCl flames evaluated based on Eq. (D.3).

Table D.4: Absorption and scattering coefficients, mass concentration of EC, mass-specific absorption coefficient, and single-scattering albedo of particle emissions for methane-only and methane-NaCl flames.

Test condition	B_{abs} (Mm^{-1})	B_{scat} (Mm^{-1})	EC mass concentration ($\mu g/m^3$)	MAC (m^2/g)	SSA
Methane-only flame	25000±2800	900±90	4500±500	5.66±0.88	0.03±0.01
Methane-NaCl flame	79000±7600	4200±290	13600±770	5.82±0.65	0.05±0.01

The SSA is calculated as follows

$$SSA = \frac{B_{\text{scat}}}{B_{\text{ext}}} = \frac{B_{\text{scat}}}{B_{\text{scat}} + B_{\text{abs}}} \tag{D.4}$$

Thus, by propagation of uncertainty, we can estimated the relative uncertainty in SSA as follows

$$\frac{\varepsilon_{SSA}}{SSA} = \sqrt{\left(\frac{\varepsilon_{B_{\text{scat}}}}{B_{\text{scat}}}\right)^2 + \left(\frac{\varepsilon_{B_{\text{ext}}}}{B_{\text{ext}}}\right)^2} \tag{D.5}$$

where the absolute uncertainty in extinction coefficient is calculated by the propagation of uncertainty as

$$\begin{aligned} \varepsilon_{B_{\text{ext}}} &= \sqrt{\left(\frac{\partial B_{\text{ext}}}{\partial B_{\text{scat}}} \times \varepsilon_{B_{\text{scat}}}\right)^2 + \left(\frac{\partial B_{\text{ext}}}{\partial B_{\text{abs}}} \times \varepsilon_{B_{\text{abs}}}\right)^2} \\ &= \sqrt{\left(\varepsilon_{B_{\text{scat}}}\right)^2 + \left(\varepsilon_{B_{\text{abs}}}\right)^2} \end{aligned} \tag{D.6}$$

Table D.4 also shows the total uncertainty in SSA for methane-only and methane-NaCl flames evaluated based on Eq. (D.5) and (D.6).

Appendix E

Thermophoretic Sampling Device Used in Lab-scale Flare Experiments

A thermophoretic sampler designed and built by the University of British Columbia was used to collect particles from the lab-scale flare described in Chapters 5 and 6. Figure E.1 shows the cross-section of the thermophoretic sampler. A small flow (100 ± 10 cm^3/min) was drawn into the sampler through a heated capillary tube with inside diameter 0.69 mm and length of 50 mm. The jet left the capillary with a temperature of approximately 150 °C and a velocity of approximately 6 m/s. Overall sampling efficiency was less than 1%, but most of the particles were deposited in the central region of the grid, such that reasonable coverage was obtained in under a minute when sampling from the main extraction duct above the turbulent diffusion flame. Large particles (with aerodynamic diameter > 2 µm) would deposit mainly by impaction, but even the largest aggregates observed in this study had an aerodynamic diameter of well under 400 nm. Tests without heating

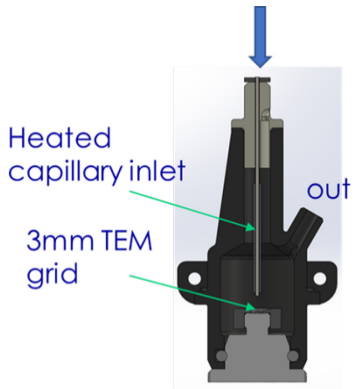

Figure E.1: The cross-section of the thermophoretic sampler.

showed minimal deposition and implied that thermophoresis was the main mechanism of deposition.

Appendix F

Details of Raman Spectroscopy Peaks

Figure F. shows the Raman spectra normalized by D1 band intensity for all test cases. There was substantial variation in the baseline, which was subtracted by considering the range between 500 to 2000 cm^{-1} and using a straight line as a subtract baseline.

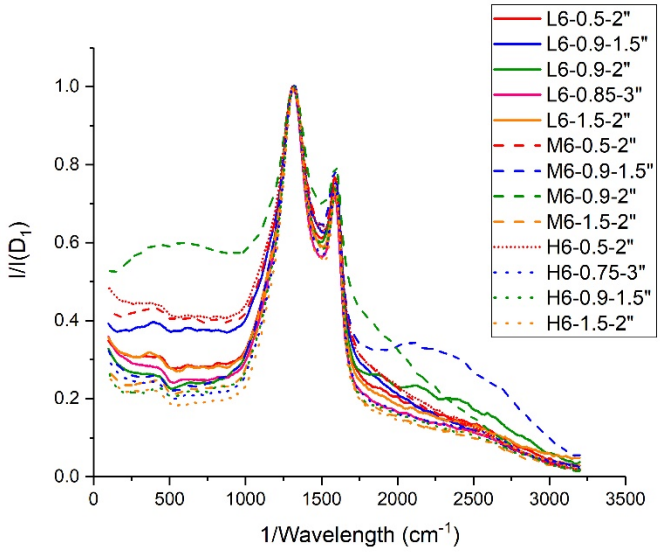

Figure F.1: Raman spectra normalized by D1 band intensity for all test cases

Table F.1 shows the centers of the fitted peaks for each band of the Raman spectra for samples collected on titanium foils using the thermophoretic sampler (TPS). Table F.2 shows the summary of peak ratios of the Raman spectra, showing their average and standard deviation values, for samples collected using both the TPS and the electrostatic precipitator (ESP) methods. Generally, the area imaged by the Raman microscope was fully covered by soot for the samples collected by

the TPS (qualitative coverage of 80–95%). However, the coverage area for the samples collected by the ESP was much lower (qualitative coverage of 30–55%).

Table F.1: Centers of the fitted peaks for each band of the Raman spectra for all test cases collected by using thermophoretic sampler.

Conditions			Peak Center				
Fuel mixture	Exit velocity (m/s)	Burner size (mm)	D1	D3	D2	D4	G
L6	0.5	50.8	1314	1518	1609	1150	1583
	0.9	38.1	1320	1513	1614	1157	1581
	0.9	50.8	1313	1537	1612	1142	1581
	0.85	76.2	1314	1523	1611	1160	1581
	1.5	50.8	1314	1526	1612	1147	1581
M6	0.5	50.8	1318	1518	1614	1162	1582
	0.9	38.1	1311	1519	1609	1153	1577
	0.9	50.8	1321	1549	1616	1188	1587
	1.5	50.8	1322	1521	1616	1178	1583
H6	0.5	50.8	1314	1523	1613	1150	1580
	0.75	76.2	1315	1517	1612	1151	1582
	0.9	38.1	1315	1493	1617	1179	1583
	1.5	50.8	1319	1527	1614	1162	1585

Table F.2: Summary of the peak ratios of the Raman spectra (showing their average and standard deviation values) for all test cases collected using TPS or ESP.

			D1/G				D3/G				D2/G				D4/G			
			TPS		ESP		TPS		ESP		TPS		ESP		TPS		ESP	
Fuel Mixture	Exit velocity (m/s)	Burner diameter (mm)	Ave.	Std. Dev.	Ave.	Std. Dev.	Ave.	Std. Dev.	Ave.	Std. Dev.	Ave.	Std. Dev.	Ave.	Std. Dev.	Ave.	Std. Dev.	Ave.	Std. Dev.
L6	0.5	50.8	11.4	1.2	10.0	0.8	1.4	0.2	1.3	0.2	0.8	0.1	0.9	0.1	1.2	0.1	1.1	0.1
	0.9	38.1	12.0	3.4	5.4	0.3	2.2	0.2	0.4	0.0	0.9	0.2	0.2	0.0	1.9	0.2	0.3	0.1
	0.9	50.8	16.1	1.5	11.4	1.1	2.2	0.2	1.4	0.2	1.0	0.1	1.1	0.1	1.2	0.2	0.9	0.1
	0.85	76.2	12.9	1.2	10.8	0.9	1.5	0.1	1.1	0.1	0.7	0.1	0.6	0.1	1.3	0.1	1.1	0.1
	1.5	50.8	–	–	8.5	0.3	–	–	0.8	0.1	–	–	0.7	0.1	–	–	1.3	0.1
M6	0.5	50.8	7.1	0.2	10.6	0.5	1.5	0.2	0.8	0.1	0.8	0.1	0.7	0.1	1.0	0.1	0.5	0.0
	0.9	38.1	9.8	1.4	6.7	0.2	1.2	0.2	0.4	0.0	0.6	0.6	0.2	0.1	0.7	0.1	0.3	0.0
	0.9	50.8	10.7	1.5	8.7	1.2	1.6	0.2	1.0	0.1	0.7	0.1	0.6	0.2	2.2	0.4	0.9	0.1
	0.9	50.8	9.0	1.2	8.2	0.7	0.9	0.1	0.6	0.1	0.7	0.2	0.4	0.1	1.0	0.2	0.7	0.1
	1.5	50.8	10.8	1.2	10.9	1.0	1.7	0.2	1.6	0.2	0.7	0.1	0.7	0.1	1.9	0.3	1.7	0.2
H6	0.5	50.8	7.0	0.6	6.6	0.2	0.9	0.1	0.4	0.0	0.6	0.1	0.5	0.0	0.7	0.1	0.5	0.0
	0.75	76.2	6.9	0.5	5.3	1.0	0.9	0.1	1.1	0.3	0.5	0.0	0.4	0.0	0.7	0.0	0.6	0.1
	0.75	76.2	–	–	8.7	1.2	–	–	1.1	0.2	–	–	0.6	0.1	–	–	0.6	0.1
	0.9	38.1	6.4	0.9	5.9	0.4	1.1	0.1	1.1	0.1	0.6	0.1	0.3	0.0	0.6	0.1	0.8	0.1
	1.5	50.8	9.1	0.8	8.9	0.8	0.9	0.1	0.9	0.1	0.7	0.1	0.4	0.1	0.6	0.1	0.6	0.0

Appendix G

Particle Size Distributions for Added NaCl Solution to Lab-scale Flare at Low and High Liquid Flow Rates

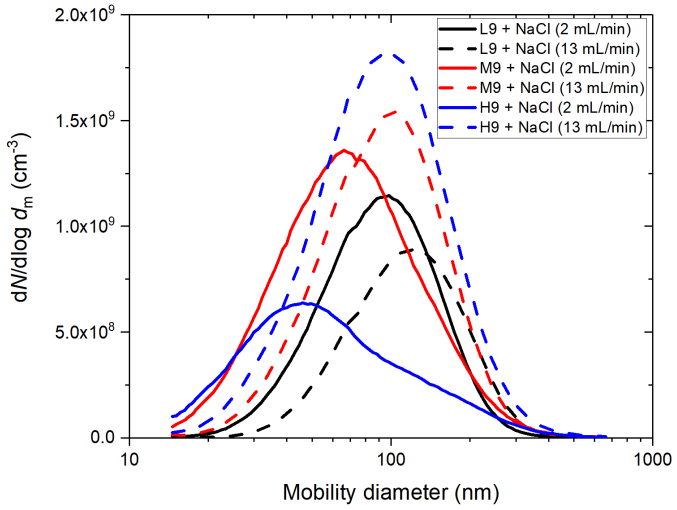

Figure G.1: Particle size distributions for L9, M9, and H9 fuel compositions with added droplets of NaCl solution at flow rates of 2 mL/min and 13 mL/min.